Department of Civil Engineering

Discrete Element Modelling of Compression Tests for an Idealised Asphalt Mixture

by

Junwei Wu

Thesis submitted to the University of Nottingham
for the degree of Doctor of Philosophy

March 2009

TO MY FAMILY

ABSTRACT

Discrete Element Modelling (DEM) has been used to simulate constant strain rate tests on an idealised asphalt mixture under monotonic compressive loading. The idealised asphalt mixture comprises approximately single-sized sand particles mixed with bitumen and was chosen so that the packing characteristics are well known (dense random packing) and its behaviour will be dominated by the bitumen whilst the complex aggregate interlock effects can be minimised. A range of constant strain-rate compressive tests to failure have been undertaken in the laboratory at various strain rates and temperatures. It was found that the strain rates applied at various temperatures can be converted to temperature-compensated strain rates at a reference temperature. The compressive strength of the material was found to be as a power-law function of the temperature-compensated strain rates in the ductile region of behaviour.

The internal geometry of the idealised asphalt mixture has been reproduced in PFC-3D and internal damage (cracking) in the material was modelled by allowing bond breakage between adjacent particles. Elastic contact properties have been used to investigate the effect of random variations in internal sample geometry, the distribution of bond strengths between adjacent particles and the coefficient of friction between particles where the bond has broken on the stress-strain behaviour. A simple viscoelastic Burger's model was introduced to give time dependent shear and normal (tensile) contact stiffnesses and an elastic contact has been assumed for the compressive normal contact stiffness. To reduce the computation time, the effect of scaling the viscosities in the Burger's model to simulate slower strain rates has been investigated.

Time dependent bond strength has been investigated and developed to model the stress-strain response of materials at different strain rates and temperatures. The bond breakage criterion has shown a good prediction of the post-peak softening behaviour of the material. The maximum rate of bond breakage was found to coincide with the peak stress (compressive strength) in the stress-strain response. Results from the model compared well to the experimental data in both brittle and ductile region of behaviour.

Keywords: Discrete Element Modelling, Monotonic Compression Test, Idealised Asphalt Mixture, Bond Breakage Criterion.

ACKNOWLEDGEMENTS

This research project was suggested by Prof. Andrew Collop who acted as my research supervisor. I am greatly in debt with him for his advice, encouragement and enthusiasm towards this project. I would also like to express my gratitude to him for proofreading this thesis. I am very grateful to Prof. Glenn McDowell who acted as the co-supervisor for his invaluable contributions during numerous discussions and his guidance throughout this project.

Special thanks to Dr. York Lee for his advice on learning DEM program. I would also like to thank Dr. Salah Zoorob and Dr. James Grenfell for their valuable discussions on the experimental work and all other technicians at the Nottingham Transportation Engineering Centre (NTEC) for providing the technical support to this project. Thanks also go to Dr. David Potyondy and Prof. Heinz Koniezky at Itasca Consulting Group Inc. for discussing the problems in the DEM modelling.

Valuable discussions were held with a number of staff members at the Department of Civil Engineering, notably Prof. Gordon Airey, Prof. Stephen Brown, Dr. Nick Thom, Dr. Wee Loo Lim, Dr. Jean-Francois Ferellec and Dr. Mingfei Lu.

My gratitude also goes to the University of Nottingham and the Nottingham Transportation Engineering Centre for their financial support.

A special thank you to all my friends at the research office, at no particular order, Jiantao, Xiaoyi, York, Joe, Riccardo, Poranic, Nono, Ted, Rawid, Lelio, Muhammed, Hung, Naveed, Muslich, with whom I have shared many enjoyable times.

Finally, all my gratitude goes to my family for their patience, understanding and encouragement and to Natalie Zhang, for her love and sacrifice throughout the thesis writing up period.

DECLARATION

The research described in this thesis was conducted in the Department of Civil Engineering at the University of Nottingham between October 2005 and September 2008. I declare that the work is my own and has not been submitted for a degree of another university.

Junwei Wu
Nottingham
March 2009

LIST OF CONTENTS

LIST OF TABLES

LIST OF FIGURES

1 INTRODUCTION

1.1 Problem Definition

The primary function of a pavement is to carry traffic safely, conveniently and economically throughout its service life. There are many reasons that may cause pavements to fail in adequately fulfilling their service function. The most common forms of structural failure are permanent deformation (i.e. rutting) and fatigue cracking. The development of a model that explains damage mechanism of flexible pavements largely relies on understanding the constitutive behaviour of the bituminous mixtures that are used in the construction.

Although asphalt is basically a granular material with an extra ingredient, bitumen, acting as binder to form the main structure, the mechanical properties of bitumen have a very important influence on the overall constitutive behaviour of mixture. Bitumen is a very different binder from cement – and the resulting mixture, asphalt therefore is quite different in its behaviour from concrete. As a viscous liquid even in the normal service temperature, bitumen has some certain features: it can “flow” at high temperature, leading to pavement rutting; it can fracture at low temperature, leading to pavement cracking; the adhesion between bitumen and aggregate can break down under a combination of ageing and water attack (Thom, 2008). Nevertheless, bitumen also plays a key role in helping maintaining the service function of a flexible pavement from cracking at high temperature, namely *healing*. Bitumen is a liquid, fractured or not, and this means that the molecular on either side of fracture can recombine to create a continuous binder phase once again over time. Thus, there is a state of dynamic flux present, which requires more fundamental understanding of the constitutive behaviour of bitumen.

Asphalt mixture is known as a viscoelastic material; they respond to loading in both an elastic and viscous manner. The complexity of this behaviour is increased by the heterogeneity of the mixture components, the bitumen being responsible for the viscoelastic properties whilst the mineral skeleton influences elastic and plastic properties. Since mixture components and compositions can be extremely diverse, this makes prediction of the properties of a particular mixture very difficult (Read and Whiteoak, 2003).

The traditional approach to model asphaltic material behaviour is to treat them at the macro-scale using continuum-based models. This usually involves undertaking careful experiments over a range of conditions (e.g. stress levels, loading rates and temperatures, etc), measuring the macroscopic response of the material and then fitting continuum-based constitutive models to the measured behaviour. The micromechanical behaviour of the asphalt is not explicitly included in this approach which means that it is not easy to relate the observed macroscopic behaviour to the micromechanics of the material (Collop *et al.*, 2004).

If a true understanding of asphalt needs to be achieved then it is necessary to think about the interaction between individual aggregate particles (Collop *et al.*, 2006; Thom, 2008). A micromechanical model can predict fundamental material properties of a composite based upon the properties of the individual constituents and it allows a thorough examination of micro structural material behaviour. Micromechanical models have tremendous potential benefits in reducing or eliminating costly tests to characterise asphalt mixture for the design purpose. Furthermore, since micro structural behaviour of individual component (e.g. stress transmission and intensities in the aggregate skeleton) can be examined, they can provide a promising insight of the micromechanics of the asphalt mixture at the aggregate level (Buttlar and You, 2001).

As a first step towards modelling the micromechanical behaviour of the idealised asphalt mixtures, Lee (2006) developed a meso-scale approach in the Discrete Element Model (DEM) to model the time dependent deformation behaviour of the idealised sand asphalt mixture under uniaxial and triaxial compressive loadings. Lee's research has shown an encouraging beginning of utilising the 3D DEM approach in modelling the linear viscoelastic behaviour of the idealised asphalt mixture in creep tests.

Following-on from the work of Lee, the logical next step is to further develop the DEM approach for modelling the constitutive behaviour of the idealised asphalt mixtures at a higher stress level where the behaviour of material shows a significant nonlinear viscoelastic feature. The internal damage of the asphalt mixture will be also investigated and modelled in the DEM. This is the topic of the work described in this thesis.

The scope of this research involves both undertaking compression tests on the idealised asphalt mixture and developing the discrete element model in modelling the constitutive behaviour of the idealised asphalt mixture under the constant strain rate condition. The idealised asphalt mixture comprising approximately single-sized sand mixed with bitumen has been selected in the experimental testing of this project. This is mainly because the idealised asphalt mixture has a relatively simple internal geometry compared to the realistic asphalt mixtures, and its behaviour is dominated by the bitumen whilst the complex aggregate interlock effect can be minimised. The responses of compression tests on the idealised asphalt mixtures at various testing conditions have been carefully measured and used as a validation to the discrete element modelling.

The development of the DEM for modelling the viscoelastic behaviour of the idealised asphalt mixture provides a means of understanding the micromechanical behaviour of the asphalt at a meso-scale (aggregate level).

1.2 Objectives of the Project

The objectives of the project can be summarised as follows:

- To investigate the fundamental stress-strain responses of the idealised sand asphalt mixture under uniaxial compressive loading over a range of testing conditions;

- To develop a 3D discrete element model by using a meso-scale approach and utilise the model to simulate the compression tests for the sand asphalt mixture;

- To develop a numerical sample preparation procedure in PFC3D to model the internal structure of the sand asphalt mixture;

- To implement a time dependent contact model in the DEM to simulate the viscoelastic properties of bitumen under the constant strain rate condition;

- To model the internal damage of the sand asphalt mixture at the meso-scale (i.e. aggregate-aggregate) by introducing a bond breaking criterion in the DEM;

- To investigate the strain rate (time) and/or temperature dependence of the sand asphalt mixture and simulate the characteristics by the numerical modelling;

- Ultimately, contribute to a better understanding of damage in the asphalt by relating the macroscopic response to the micromechanical properties at the meso-scale.

1.3 Thesis Structure

This thesis is organised as follows:

Chapter 1 – Introduction

The current chapter defines the problem and introduces the topic of this study. The general objectives of this research are also clearly stated.

Chapter 2 – Literature Review

Chapter 2 starts by reviewing the mechanical properties of asphaltic materials which are widely used in modelling constitutive behaviour of asphalts. This is followed by a brief review and a description of the two main distress mechanisms that are prevalent in well trafficked flexible pavements, i.e. fatigue cracking and permanent deformation. The monotonic behaviour of bitumens and asphalt composites and constitutive relationships that describe such behaviour are also described. This chapter also includes a review of the constitutive models based on continuum mechanics that have been well developed in the last few decades. The final part of this chapter reviews the behaviour of thin films of bitumen, which subsequently forms the background for a more realistic understanding of the contact stresses & strains when modelling the behaviour of asphalt mixtures using Discrete Element Modelling techniques.

Chapter 3- Discrete Element Modelling (DEM)

Chapter 3 starts by reviewing micromechanical models for asphalt. This is followed by a brief review and a description of the DEM and the software package PFC3D used in the modelling. This is then followed by a review of the development and application of the DEM in soil and rock, and more recently in asphalt. This chapter also reviews the theory and background of typical contact models in PFC3D.

Chapter 4- Experimental Work

Chapter 4 contains details of uniaxial compression tests performed on an idealised asphalt mixture over a range of strain rates and temperatures. The idealised asphalt mixture comprises approximately single-sized sand mixed with bitumen. As a first step to develop a micromechanical model to simulate the behaviour of asphalt mixtures, the behaviour of idealised asphalt mixtures are investigated. The selection and preparation of this type of idealised asphalt mixture are also presented in this chapter. A series of monotonic tests were performed to failure on this mixture under uniaxial compressive loadings and the stress-strain responses are presented and analysed in the last part of this chapter.

Chapter 5- Numerical Sample Preparation Procedure

Chapter 5 describes a procedure to generate a numerical sample in PFC3D that replicates the volumetric characteristics of the idealised sand asphalt mixture. A measurement method has also been introduced to quantify the stress and strain quantities of the numerical sample during simulations.

Chapter 6- Elastic Modelling

Chapter 6 presents the investigations performed to model elastic response of sand asphalt mixture by using an elastic contact model in DEM. The bond breakage has been introduced successfully to simulate the internal damage of sand asphalt under the compressive loadings. The effects of number and positions of particles, loading speed, bond strength variations and friction coefficient are examined. The elastic simulation results have been compared to the experimental data when its behaviour is dominated in the elastic region.

Chapter 7- Viscoelastic Modelling

Chapter 7 presents simulations used to model viscoelastic behaviour of sand asphalt mixture over a range of strain rate and temperatures. The analytical solution of Burger's viscoelastic contact model under a constant strain rate has been solved and described in this chapter. The Burger's model has been used to simulate time dependent shear and tensile normal contact behaviour of the sand asphalt mixture and elastic response has been assumed to represent the normal compressive behaviour. A computation time optimisation method has also been described in this chapter. The strain rate and/or temperature dependent bond strength has been justified and used in DEM simulations to simulate strain rate dependent compressive strength of sand asphalt mixture.

Chapter 8 – Conclusions and Recommendations for Future Work

Chapter 8 summaries conclusions from this research and presents recommendations for future research.

2 LITERATURE REVIEW

2.1 Introduction

Asphalt is a complex multi-phase material comprising bitumen, graded mineral aggregate and air. A range of asphalt types and compositions can be produced depending on the types and proportions of these components and on the aggregate grading. A typical continuously graded mixture (e.g. asphalt concrete) relies on an interlocking aggregate skeleton for its strength with the binder primarily acting as a lubricant to aid compaction and "glue" the mixture together. At the other extreme, a typical gap-graded mixture (e.g. stone mastic asphalt) will have a discontinuous aggregate grading (i.e. some stone sizes will not be present) and relies on a coarse aggregate skeleton bound by a bitumen/filler "mortar" for its strength. It has been shown that for both asphalt mixture types the micromechanical behaviour, at the scale of an aggregate particle, is an important factor in terms of overall material performance (Collop *et al.*, 2006).

This chapter starts by reviewing the mechanical properties of asphaltic materials (i.e. stiffness) which are traditionally used in characterising constitutive behaviour of asphalts. This is followed by a brief review and a description of the two main distress mechanisms that are prevalent in well trafficked flexible pavements, i.e. fatigue cracking and permanent deformation. The monotonic behaviour of bitumens and asphalt composites and constitutive relationships that describe such behaviour are also described. This chapter also includes a review of the constitutive models based on continuum mechanics that have been well developed in the last few decades. The final part of this chapter reviews the behaviour of thin films of bitumen, which subsequently forms the background for a more realistic understanding of the contact stresses & strains when modelling the behaviour of asphalt mixtures using Discrete Element Modelling techniques.

2.2 Review of Mechanical Properties of Asphalt

2.2.1 Stiffness of asphalt

Initial attempts at modelling asphalt were conducted by treating the composite as a soil (Nijboer 1948; Goetz and Chen 1950). Rate-independent plastic behaviour of asphalt had been assumed in these approaches, and this culminated in a viscoelastic description of asphalt behaviour in the 1950s. The most common approach was by van der Poel (1954) who introduced the concept of "stiffness" to describe the behaviour of pure bitumen as a function of loading time and temperature. He indicated the stiffness of bitumen at lower strains could be correlated with the penetration index and softening point of the bitumen. This research resulted in the well known van der Poel Nomograph (1954), by means of which, the deformation of bitumen can be calculated as a function of stress, time and temperature. Van der Poel (1955) extended the concept of stiffness to describe the behaviour of asphalt mixtures as a function of stiffness of bitumen (S_b) and the volume fraction of the aggregate (C_v). Heukelom and Klomp (1964) reported similar findings by proposing the following relationships for predicting the stiffness of an asphalt mixture:

$$\frac{S_{mix}}{S_{bit}} = \left[1 + \frac{2.5C_v}{n(1-C_v)}\right] \tag{2.1}$$

Where C_v is the volume fraction of the aggregate and n is defined by:

$$n = 0.83\log\left[\frac{4\times10^{10}}{S_{bit}}\right] \tag{2.2}$$

Where S_{bit} is the stiffness of the bitumen (Pa).

The above equations were derived from empirical fits to test data obtained from static and dynamic tests on well-compacted asphalt mixtures containing approximately 3% of air voids and C_v values ranging from 0.7 to 0.9.

Brown *et al.* (1986) modified this approach by re-defining the mixture stiffness as a function of bitumen stiffness and the percentage of voids in mixed aggregate (*VMA*), by proposing:

$$\frac{S_{mix}}{S_{bit}} = \left[1 + \frac{275.5 - 2.5VMA}{n(VMA - 3)}\right] \tag{2.3}$$

Where n is the same function of S_{bit} as in Equation 2.2.

Figure 2.1 shows a plot of bituminous mix stiffness versus bitumen stiffness for different values of *VMA* based on Equation 2.3. It should be noted that Equation 2.3 is valid for *VMA* values from 12 to 30% and $S_{bit} \geqslant 5\ MPa$. For higher value of bitumen stiffness ($S_{bit} \approx 1\ GPa$), the bitumen behaves as an elastic solid and the stiffness ratio is a measure of stiffening effect when rigid aggregate is included in an elastic matrix. However, for lower values of S_{bit}, the stiffness ratio becomes a function of the elastic, viscoelastic and viscous response of the material.

2.2.2 Permanent deformation of asphalt

Permanent deformation (i.e. rutting) occurs when material from under the wheel path of a truck flows to form a groove or rut (Thrower 1979). The two major mechanisms in asphalt materials that contribute to permanent deformation are densification and shear displacement. Densification is caused by the aggregate skeleton becoming more closely packed and it tends to occur relatively early in the life of pavement due to poor compaction during construction (Newcomb *et al.*, 1997). It has been reported by Eisenmann and Hilmer (1987) that good compaction of pavement during construction can reduce the possibility of further densification. Shear displacement is the process of lateral material flow, which can result in the development of shoulders on either side of a rut. Many researchers (Hofstra and Klomp, 1972; Eisenmann and

Hilmer, 1987; Collop *et al.*, 1995) have indicated that the shear displacement is a primary factor that causes the rutting if a pavement has been well compacted during construction while further densification is unlikely.

It is well documented (Cheung, 1995; Deshpande and Cebon, 2000; Dunhill, 2002) that bitumen is a thermoplastic material, and in the two extremes it can behave either as elastic solid or as a viscous fluid depending on temperature and loading time. At low temperatures and/or short loading times bitumen's response is predominantly elastic, whereas for high temperatures and/or long loading times the viscous properties are dominant. In the intermediate range, bitumen exhibits both elastic and viscoelastic behaviour and displays a time dependent relationship between applied stress and resultant strain. When a load is applied to an asphalt mixture, it deforms with an instantaneous elastic response after which the strain gradually increase with loading time. Upon removal of load the initial elastic strain recovers as does further delayed elastic strain leaving an irrecoverable small residual strain. This residual strain will be accumulated under many load applications and will lead to pavement rutting. The phenomenon of permanent strain accumulation is illustrated in Figure 2.2 and 2.3.

2.2.3 Fatigue characteristics of asphalt

Fatigue cracking has been defined by Read (1996) as follows:

Fatigue in bituminous pavements is a phenomenon of cracking. It consists of two main phases, crack initiation and crack propagation, and is caused by tensile strains generated in the pavement by not only traffic loading but also temperature variations and construction practices.

Crack initiation is generally described as the point at which the micro cracks have coalesced and formed a macro crack under the repeated application of tensile stresses. Crack propagation concerns the growth of the macro crack when the material undergoes further application of tensile stress, which normally leads to failure of materials.

During the course of a normal fatigue test, a load pulse is applied to a specimen in the form of an alternating stress or strain having a predetermined amplitude and the number of load applications required fail the specimen are determined. The tests are thereafter performed on several specimens at a range of stress or strain levels and the results are plotted as stress or strain against number of load cycles to failure on a log-log scale.

Typical results of a fatigue test on Hot Rolled Asphalt (HRA) have been plotted in Figure 2.4, in which it can be seen that for each test temperature a straight line passes through the mean values of the cycles to failure at each stress level. Figure 2.4 also shows that fatigue lines for different test temperatures are approximately parallel with longer lives at lower temperatures. When the results of fatigue tests are re-plotted in terms of strain as shown in Figure 2.5, it can be seen that the results from different stiffnesses coincide, indicating that strain is the criterion of failure and that the effects of temperature and loading time can be accounted for by their effect on stiffness. This is known as ‘strain criterion’ (Pell and Taylor, 1969) and tensile strain is generally accepted as the fatigue cracking performance criterion for bituminous materials (Brown, 1995).

The above criterion is restricted to a description of the crack initiation phase during fatigue failure, while during some test conditions (e.g. high temperatures) or in some test configurations, there may be considerable crack propagation during the test and these effects are shown in Figure 2.6, where the fatigue lines will be steeper and displaced.

The general relationship defining the fatigue life based on crack initiation is as follows:

$$N_f = K_1 \left(\frac{1}{\varepsilon_i} \right)^{K_2} \tag{2.4}$$

Where N_f = number of applications of load to initiate a fatigue cracking

ε_t = maximum value of initial tensile strain

K_1, K_2 = factors depending on the composition and properties of the mixture

The results shown in Figure 2.4 and 2.5 were obtained from tests performed under conditions of stress controlled mode (i.e. maximum stress amplitude maintained constant throughout the test). The “controlled stress” type of loading results in the specimen failing very quickly following crack initiation. Therefore, the difference between the two lines in Figure 2.6 is small. An alternative way to test the fatigue specimens is under the condition of “controlled strain”. Under this condition, a significant time is taken for cracks to propagate before failure. Under these conditions, the separation between the two lines in Figure 2.6 is large.

Unfortunately, the strain criterion does not account for the differences in fatigue life measured using controlled stress and controlled strain experiments. Van Dijk (1975) suggested that the differences in fatigue life determined under conditions of stress controlled and strain controlled can be explained by the dissipated energy concept. This is defined as the amount of energy that is lost (dissipated) from the asphalt, due to fatigue damage per cycle summed for entire life of specimen during cyclic loadings. This concept has been developed by Rowe (1993) who has shown that dissipated energy can be used to predict the fatigue life to crack initiation accurately.

Also, Carpenter and Shen (2006) developed a dissipated energy approach to study the phenomenon of healing in Hot-Mix Asphalt (HMA) in fatigue tests. They have conducted an analysis of healing and HMA fatigue behaviour by introducing a specifically designed fatigue-healing test. They claimed that healing does exist and its effect on fatigue life can be indicated by an energy recovery per second of rest period.

It has been well documented that the rate of crack propagation is controlled by the tensile stress at the crack tip (Read, 1996). The formation of a crack leads to local strain relief. Under controlled stress conditions it is easy to define the end point since the test has a relatively short crack propagation phase and hence, the failure point is clearly defined when the specimen has completely failed. However, testing under controlled strain conditions, has the effect of decreasing the tensile stress at the crack tip and hence retarding the rate of crack propagation. Therefore, it is usual to define failure in a controlled strain mode of fatigue testing as the point when the stiffness has decreased to 50% of its initial value.

Most fatigue tests are performed under simple loading conditions that involve continuous loading cycles of a specific magnitude, under a particular testing temperature and frequency. However, in reality the material is subjected to a succession of various magnitudes of load pulses and various time intervals between loading pulses, depending on the details of the traffic and temperature conditions. It has been shown that the damage caused by each magnitude of load pulse at various time intervals can be predicted by the results of simple loading tests, where the loading conditions remain unchanged, according to a linear damage hypothesis, such as Miner's rule as follows:

$$\sum_{i=1}^{j} \frac{n_i}{N_i} = 1 \tag{2.5}$$

Where n_i = number of cycles of strain level ε_i applied

N_i = number of cycles of strain level to produce failure in a simple loading test

j = number of different strain levels

2.3 Review of Monotonic Constitutive Behaviour

A flexible pavement comprising an asphaltic base can be assumed to behave as a plate in bending under traffic loading when laid out on a rigid supporting granular sub-base. Collop and Cebon (1995) revealed that shear stresses at the type-pavement interface can cause cracks to run from the surface down into the base layer. Alternatively, Brown and Brunton (1986) assumed that cracks usually initiate at the bottom of the asphalt layer and grow upwards. This creates a situation of crack opening, or mode I loading.

Fatigue cracking in asphalt pavements, as described in the previous section, can cause a loss of bending stiffness which leads to surface deformation and a significant deterioration of serving life. This process involves the growth of distributed micro cracks, and the development of visible macro cracks. The main sources of pavement distress which contribute to crack growth are repeated traffic and thermal loading. In order to understand the process of fatigue cracking, it is first necessary to examine the monotonic behaviour of bitumen and asphalts during a single loading cycle.

2.3.1 Monotonic constitutive behaviour of bitumen

Early experiments (usually creep tests) indicated that the constitutive behaviour of asphalt mixture is strongly dependent on the bituminous binder even though the mixture contains less than 10% by volume of bitumen (Ossa *et al.*, 2003). Experiments over a range of testing conditions (e.g. temperature, constant strain rate and loading stress) have been performed by many researchers to understand the constitutive behaviour of bitumen and bituminous materials. A typical creep test result of asphalt mixture is shown in Figure 2.7. In this figure although the initial elastic and the primary creep strains (Region 1) cannot be neglected, they occur quickly, and they can be treated in much the way that elastic deflection is allowed for in a structure. But thereafter, the material enters steady-state, or secondary creep (Region 2), and the strain increases steadily with time. It is usually this steady accumulation of strain with time that concerns us most.

Cheung and Cebon (1997) developed a deformation map (Figure 2.8) for bitumen over a wide range of temperatures and strain rates. Figure 2.8 shows the steady-state stress/strain relationship of a 50 pen bitumen at temperatures ranging from -10°C to 30°C. They described the steady-state uniaxial behaviour of pure bitumen by a Modified Cross Model (MCM) which relates steady-state stress (σ), steady-state strain rate ($\dot{\varepsilon}$), reference stress (σ_0), reference strain rate ($\dot{\varepsilon}_0$) and a material constant (n_c) as shown in Equation 2.6:

$$\frac{\sigma}{\sigma_o}=\frac{\dot{\varepsilon}}{\dot{\varepsilon}_0}\left(\frac{1}{1+\left(\frac{\dot{\varepsilon}}{\dot{\varepsilon}_0}\right)^{n_c}}\right) \tag{2.6}$$

This model becomes linear (Newtonian) creep at low strain rates and assumes a power-law creep relationship at higher strain rates. They also found that the temperature dependence of bitumen was controlled by the activation energy (Arrhenius equation) at low temperatures (T ≤ 20°C) and by the free volume (WLF equation) at higher temperatures (T ≥ 20°C):

$$\frac{\dot{\varepsilon}_{0c}}{\dot{\varepsilon}}=\exp\left(\frac{Q_c}{RT}\right), T \le T_d \tag{2.7}$$

$$\log\left(\frac{\dot{\varepsilon}_s}{\dot{\varepsilon}_0}\right)=\frac{-a_1(T-T_s)}{a_2+(T-T_s)}, T \ge T_d \tag{2.8}$$

The values of the material constants $R, \dot{\varepsilon}_{0c}, \dot{\varepsilon}_s, a_1, a_2, Q_c, T_s, T_d, n_c$ and σ_0 can be found in Cheung and Cebon (1997). Similar findings have been reported by Harvey *et al.* (2003) who conducted a series of tension tests on a 100 pen pure bitumen.

Cheung (1995) also performed an experimental study on pure bitumen tested in uniaxial tension and shear over a wide range of stresses, strain rates and temperatures. In isothermal conditions the constitutive behaviour of pure bitumen in uniaxial tension is given by:

$$\left(\frac{\dot{\varepsilon}}{\dot{\varepsilon}_0}\right)=\left(\frac{\sigma}{\sigma_0}\right)^n \tag{2.9}$$

Where $\dot{\varepsilon}_0$ is the reference strain rate, σ_0 is the reference stress and *n* is the power law coefficient. At ambient temperatures the power-law constitutive behaviour of pure bitumen in three dimensions can be generalised as the form:

$$\left(\frac{\dot{\varepsilon}_{ij}}{\dot{\varepsilon}_0}\right)=\frac{2}{3}\left(\frac{\sigma_e}{\sigma_0}\right)^n\frac{\sigma'_{ij}}{\sigma_e} \tag{2.10}$$

where $\sigma'_{ij}=\sigma_{ij}-\frac{1}{3}\delta_{ij}\sigma_{kk}$ is the deviator stress tensor, δ_{ij} is the Kronecker delta, and $\sigma_e=\left(\frac{3}{2}\sigma'_{ij}\sigma'_{ij}\right)^{1/2}$ is the von Mises effective stress. Equation 2.10 is applicable in describing steady-state constitutive behaviour of most metal, polymer and ceramics. Cheung and Cebon (1997) studied its applicability to bitumen by examining the measured behaviour of pure bitumen in shear. They indicated that the generalised form of power-law constitutive equation that relates the behaviour of bitumen in shear is given by:

$$\left(\frac{\dot{\gamma}}{\dot{\varepsilon}_0}\right)=\sqrt{3}^{\,n+1}\left(\frac{\tau}{\sigma_0}\right)^n \tag{2.11}$$

It can be seen from Equations 2.9 and 2.11 that the behaviour of pure bitumen in tension and shear are expected to be related by a factor of $\sqrt{3}^{\,n+1}$. It indicates that for bitumen behaviour in the linear region (n = 1), the shear strain rate is three times the tension strain rate for a given applied stress throughout the stress range. Lethersich (1942) performed a numerical analysis to investigate the mechanical behaviour of bitumen in the linear viscous region. He indicated that for small stress level bitumen viscosities are associated with a shear stress which is equal to one third of the tensile stress in a plane where the tensile and shear strain are equal. Consequently, it can be concluded that in the linear region the tensile stiffness of pure bitumen is approximately three times the shear stiffness of pure bitumen.

2.3.2 Monotonic constitutive behaviour of idealised asphalt mixture

Deshpande and Cebon (2000) performed uniaxial and triaxial compression tests on various types of idealised asphalt mixtures containing different volume fractions of rigid inclusions (ranging from 40% to 85%) under various strain rates and temperatures. Size effect of sand particles was also examined by using various sized sand particles in different mixtures. Constant strain rate tests were performed at 20 and 40°C on an idealised asphalt mixture with 64% volume fractions of sand. A typical data was shown in Figure 2.9, where the nominal stress is plotted against the nominal axial strain for various applied strain rates at 20°C. It can be seen in this figure that at a particular strain rate, the stress increases until the strain reaches approximately 4%. Beyond 4%, the stress starts to decrease. Following Ward (1983) and Cheung (1995) the "steady-state creep stress" is defined as the maximum observed stress. It can be seen in Figure 2.9 that at a constant temperature the value of the steady-state creep stress increases with increasing applied strain rate.

The uniaxial steady-state behaviour observed from these tests on a single type of mixture over a range of temperature from 0°C to 40°C is shown in Figure 2.10. It can be seen from this figure that the curves for mix at different temperatures have the same shape as the curve for pure bitumen at 20°C obtained by Cheung (1995), but are shifted by a stiffing factor *S*. Consequently, the MCM was modified by Deshpande and Cebon (2000) to describe the uniaxial steady-state creep behaviour of the idealised asphalt mixture by simply replacing $\dot{\varepsilon}/\dot{\varepsilon}_o$ in Equation 2.6 with $S\dot{\varepsilon}/\dot{\varepsilon}_o$:

$$\frac{\sigma}{\sigma_0} = \frac{S\dot{\varepsilon}}{\dot{\varepsilon}_0}\left(\frac{1}{1+\left(\frac{S\dot{\varepsilon}}{\dot{\varepsilon}_0}\right)^m}\right) \tag{2.12}$$

Where *S* is the stiffening factor due to the presence of aggregate. For example, it can be seen in Figure 2.10 that the stiffening factor for the mix at 20°C is approximately 1000. This indicates that at the same stress level, the mixture at 20°C has a steady strain rate of about 1000 times lower than that of pure bitumen at 20°C. They also reported that the stiffening effect is only dependent on the volume fraction of aggregate and is independent of the size and shape of aggregate. The stiffening factor increases with increasing volume fraction of aggregate in the mixtures. Consequently, Deshpande and Cebon (2000) concluded that the major effect of adding rigid spherical aggregate is to stiffen the bitumen without changing the form of the uniaxial steady - state stress - strain rate relationships or the temperature dependence.

Khanzada (2000) also investigated the constitutive behaviour of idealised asphalt mixture using simple laboratory tests. Two types of idealised asphalt mixture have been used: Mixture *A* which comprises approximately single-sized sand and Mixture *A/D* which comprises double sized sand. 50 pen grade bitumen was used as the binder mixed with sand to form different mixtures. A series of constant strain rate tests were performed on both types of idealised asphalt mixtures at 20 and 30°C. A typical axial stress-strain curve for Mixture *A/D* at 20°C has been shown in Figure 2.11. Similar findings have been reported by Khanzada that the constitutive behaviour of Mixture *A* and *A/D* follows the Equation 2.12. Khanzada also concluded that the temperature dependence of Mixture *A* and *A/D* was governed by the bitumen and was found to follow the free volume model (WLF equation), which was incorporated into Equation 2.8 for temperatures above 20°C.

Collop and Khanzada (1999) performed wheel tracking tests on the idealised asphalt mixtures *A* and *A/D* at three stress levels (500, 750 and 1000 kPa) and at three temperatures (20, 30 and 40°C). Figure 2.12 shows a typical testing result that the average rut depth plotted against number of cycles at 40°C for mixture *A/D*. It can be seen from this figure that after an initial period where rutting rate decreases, the rut depth increases approximately in proportion to the number of cumulative load passes. They explained that the initial behaviour might be associated with densification where the density of sample increases under early loading. The second part of the curve can be characterised by a steady-state rutting rate (gradient). They have also reported that the rutting rate of idealised asphalt mixture increases with increasing either temperature or contact stress.

2.3.3 Monotonic constitutive behaviour of realistic asphalt mixtures

Khanzada (2000) performed a series of uniaxial tests, triaxial tests and wheel tracking tests over a range of temperatures (20°C to 40°C) and applied stress levels (200 to 2000 KPa) to investigate the constitutive behaviour on realistic asphalt mixtures (HRA and DBM). The uniaxial steady-state constitutive behaviour of an HRA mortar, a 30/10 HRA mixture and a 10mm DBM mixture was found to have the same form as the steady-state deformation behaviour of the pure bitumen and idealised mixtures. Figure 2.13 shows the plot of steady-state constitutive behaviour of HRA mixture, HRA mortar and pure bitumen. It can be seen from this figure that the stiffening factor (*S*) of HRA mortar is about 200,000 which is a slightly smaller than result of HRA mixture. Figure 2.14 shows the stiffening factor of all testing mixtures increases with increasing the volume fractions of aggregate in the mixture. Figure 2.15 shows the dilation gradients (defined as ratio of volumetric strain to distortional strain) measured for the various realistic asphalt mixtures plotted as a function of volume fraction of the aggregate in the mixtures. It can be seen in this figure that the dilation gradients also increase with increasing volume fraction of aggregate in the mixture. Consequently, Khanzada concluded that increasing the volume fractions of aggregate in the mixture will result in stiffening the mixture and higher dilation gradient.

Dunhill (2002) performed a series of uniaxial compression and tension tests on DBM and HRA over a range of constant displacement rates (0.1, 1 and 10 mm/s) and temperatures (5, 20 and 35°C). In uniaxial monotonic compression tests, Dunhill found that both DBM and HRA exhibited the similar stress-strain response under the same testing condition whilst HRA shows a higher compressive strength than DBM due to the higher fractions of binder. The general trend of each mixture in compression tests is for the compressive strength to increase with increasing strain rate and/or decreasing temperature. Similar trend as compression tests has been observed in tension tests on DBM and HRA. Dunhill (2002) reported that the dominant failure mode in a well lubricated uniaxial compression test is that of axial splitting, and that the failure mode in a tension test is dependent on the stress applied to the test specimen.

Taherkhani (2006) also performed a comprehensive investigation in the constitutive behaviour of both DBM and HRA under uniaxial monotonic loading. Constant stress creep tests over a range of stress levels and temperatures, and constant strain rate tests over a range of strain rates and temperatures were conducted by Taherkhani. The steady-state deformation behaviour of the mixtures was found to be well captured by the Modified Cross Model (MCM) as Equation 2.12, with linear behaviour at low stress (<50 kPa for the HRA and 100 kPa for the DBM) and non-linear power-law creep behaviour at high stress (>400 kPa). The temperature dependency of the mixtures was found to be predicted by the WLF equation when the temperature is higher than 20°C.

2.4 Review of Constitutive Modelling of Asphalt

2.4.1 Elastic model

The simplest constitutive model for an asphalt mixture is based on the theory of linear elasticity. In this theory materials are usually assumed to be homogeneous, isotropic and linear elastic and characterised by time independent constants of proportionality between stress and strain (Huang, 1967). This kind of material is described as elastic, where the loading curve is identical to the unloading curve, and all the strains are recovered upon the removal of applied load. According to the Hooke's law, the stress and strain relationship of an elastic material is expressed as:

$$\{\sigma\} = [D] \times \{\varepsilon\} \tag{2.13}$$

where $\{\sigma\}$ and $\{\varepsilon\}$ are stress and strain tensor, respectively. [D] is the stiffness matrix of elasticity including two material constants (Young's modulus, E and Poisson's ratio, v) expressed as:

$$[D] = \frac{E}{(1+v)(1-2v)} \begin{bmatrix} 1-v & v & v & 0 & 0 & 0 \\ & 1-v & v & 0 & 0 & 0 \\ & & 1-v & 0 & 0 & 0 \\ & & & 0.5-v & 0 & 0 \\ & SYM & & & 0.5-v & 0 \\ & & & & & 0.5-v \end{bmatrix} \tag{2.14}$$

For asphaltic materials, the Young's modulus was replaced by a "stiffness modulus" since the stiffness varies with loading duration and temperature (van der Poel (1954)). It has been well documented (Monismith and Secor., 1962; Van de Loo, 1978;

McLean, 1977; Lu, 1998) that at low temperatures and short loading times, the prediction of asphalt pavement behaviour by using the linear elastic method is accurate enough for engineering purposes. A few researchers such as Peutz *et al.* (1968) and Eisenmann *et al.* (1977) successfully applied the linear elastic models in flexible pavement design and performance evaluation in the past. At present, the elastic model is still employed by Shell in the BISAR computer program for pavement structure analysis.

Non-linear elastic models are also employed to solve the problem of non-linear behaviour of asphalt mixtures. Hicks and Monismith (1972) and Starodubsky *et al.* (1990) demonstrated that stress-strain curves generally experience a linear and a non-linear period before reaching their peak value where the non-linear behaviour comes from the development of microcracks.

2.4.2 Linear viscoelastic model

Materials that exhibit time-dependant behaviour in their relationship between stress and strain can be described as viscoelastic. The behaviour of asphalt materials subjected to loading can be simply described as linear viscoelastic at low stress and strain levels (Moavenzadeh and Soussou, 1968). Viscoelastic description of the behaviour of bitumen became popular in 1950's when van der Poel (1954) introduced the stiffness modulus of bitumen as a function of loading time and temperature. Thereafter, the viscoelastic models have been widely developed to describe the behaviour of asphalt in the linear region (Starodubsky *et al.*, 1990; Sousa and Weissman, 1994).

Mechanical models based on springs and dashpots are widely used to establish a relationship between the stress and strain as a function of time for viscoelastic materials. The mechanical models are comprised of purely elastic elements (springs) and purely viscous elements (dashpots). These elements are combined in series as a Maxwell model, and parallel as a Kelvin model or combinations of both such that they can exhibit the desired elastic, viscoelastic and viscous properties.

Ossa *et al.*, (2005) has described that applications of mechanical models for the characterisation of asphalt mixtures have yielded reasonable agreement with experimental results at the condition of low stress and strain levels. The Burger's model, composed of a Maxwell model connected in series to a Kelvin model, has been introduced to describe linear viscoelastic behaviour of the asphalt material (Collop *et al.*, 2006). The generalised Burger's viscoelastic model is shown in Figure 2.16. The standard differential equation of stress-strain response under the conditions of constant stress has been solved and the creep response to a step change in stress σ_0 is presented as:

$$\varepsilon(t) = J(t)\sigma_o = \left\{ \frac{1}{K_0} + \frac{t}{C_\infty} + \frac{1}{K_1}\left[1 - e^{(-t/\tau_1)}\right] \right\}\sigma_o \tag{2.15}$$

Where: $J(t)$ is the creep compliance. K_0 is stiffness for the spring in the Maxwell model, K_1 is the stiffness for the spring in the Kelvin model, C_∞ is the viscosity for the dashpot in the Maxwell model and C_1 is the viscosity of the dashpot in the Kelvin model. $\tau_1 = C_1 / K_1$.

The features of viscoelastic behaviour represented by Burger's model are illustrated in Figure 2.17. Initial elastic response with strain *OA* occurs instantaneously when the stress is applied. A further delayed elastic strain *AB* is acquired in time. If the material is subjected to creep, it will also acquire a steadily increasing creep strain *BC*. When the stress is removed, there is an immediate elastic recovery (same magnitude to *OA*) and delayed elastic recovery *DE*, left with a permanent strain at *E* which is acquired through the action of creep.

2.4.3 Nonlinear viscoelastic model

It has been stated in the last section that at high stress and strain levels, the response of asphalt mixtures cannot be adequately modelled by a linear viscoelastic approximation. At higher stress (0.1 *MPa* to 1 *MPa*), experimental studies such as those conducted by Gaskins *et al.* (1960), Sisko (1965) and Welborn *et al.* (1966) found that bitumen behaves as a nonlinear viscous material.

Lai and Anderson (1973) suggested that the nonlinear viscoelastic behaviour of asphalt mixtures can be represented by a nonlinear generalised model that consists of a nonlinear dashpot connected in series to a nonlinear Kelvin chain. In this model, the nonlinear dashpot accounts for the time dependent irrecoverable strain (viscous flow) and the nonlinear Kelvin chain accounts for the power law time dependent recoverable strain (see Lai and Anderson (1973) for the constitutive equations). They claimed that this model can be used successfully in predicting the creep behaviour of an asphalt mixture under multiple-step loading and repeated loading.

Cheung and Cebon (1997) developed a deformation mechanism for bitumen over a wide range of temperatures, stresses and strain-rates. They showed that the transition from linear viscous behaviour at low stresses to nonlinear viscous behaviour of the bitumen at higher stresses can be captured by the Modified Cross model. The bitumen model proposed by Cheung and Cebon (1997b) relates the steady-state stress and the steady-state strain-rate through the Equation 2.6 where the behaviour of the bitumen is governed in the nonlinear regime.

Harvey (2000) developed a rheological model consisting of Maxwell and Kelvin elements in series, based on linear springs and nonlinear (power-law) dashpots (as sketched in Figure 2.18) and this model was found to provide a reasonable representation of the tensile behaviour of thin films of bitumen over a range of testing conditions such as temperature, strain rates and aspect ratios. Harvey (2000) stated that the nonlinear viscoelastic model can successfully predict the tensile stress-strain response of bitumen when either rupture in thick ductile films or voiding in thin bitumen films has been included.

Although nonlinear constitutive models for bitumen can be found in the literature, they have rarely been applied to specific engineering problems. The main drawback of applying the nonlinear viscoelastic model in practice is that these models usually require many calibration constants and complex fitting procedures. In the modelling of the constitutive behaviour of bitumen and bituminous mixtures, linear viscoelastic models are still the popular choice (Cheung and Cebon 1997).

2.4.4 Finite element model

During the last decade Finite Element Methods (FE) has become a popular choice for modelling the deformation behaviour of bituminous mixtures (Sepehr *et al.*, 1994; Long, 2001; Collop *et al.*, 2003; Sadd *et al.*, 2004). These models usually implement the viscoelastic or viscoelastoplastic constitutive model to the FE modelling. For example, Long (2001) used a nonlinear viscoelastic extension to the models proposed under the SHRP-A-415 (1994). Collop *et al.* (2003) developed a viscoelastoplastic model with damage for asphalt based on the model proposed by Scarpas and Blaauwendraad (1998).

2.5 Review of Verification and Validation of a Numerical Model

2.5.1 Verification and validation (V&V) in computer modelling

A critical question has been raised in the recent years by developers of computer codes, analyst who uses the codes and decision makers who rely on the results of the analyses: How should confidence in modelling and simulation be critically assessed? Verification and validation (V&V) of the computational simulations are believed by many researchers as the primary methods for building and quantifying this confidence (Kleijnen, 1995; Balci, 1997; Oberkampf, 2001; Oberkampf and Barone; 2005).

A brief definition of verification and validation is raised by Oberkampf *et al.* (2004): *Verification* is the process of determining that a model implementation accurately represents the developer’s conceptual description of the model and the solution to the model. *Validation* is the process of determining the degree to which a model is an accurate representation of the real world from the perspective of the intended uses of the model.

Briefly, verification is the assessment of the accuracy of the solution to a computational model while validation is the assessment of the accuracy of the computational simulation by comparison with experimental data. Therefore, in verification, the relationship of the simulation to the real world is not the main concerning issue and but in validation, the relationship of the computation and the real world (i.e. experimental data) is the issue.

Fundamentally, V&V are tools for assessing the accuracy of the conceptual and computerized models (Oberkampf, 1998). Some important implications and subtleties in the definitions of V&V need to be addressed. The first significant feature is that both V&V are "process of determine" which means they are going activities that do not have a clearly defined completing point. Indeed, one cannot prove that complex computer codes have no errors. Thus, V&V activities can only assess the correctness or accuracy of the specific cases that are tested.

The emphasis on "accuracy" is the second feature that is common in the definitions of V&V. This feature assumes that a measure of correctness can be determined. In the verification process of a model, accuracy is generally measured in relation to benchmark solutions of simplified, or closely related, model problem (Oberkampf *et al.* (2004)). However, Oberkampf (2004) further claimed that in the solution with discontinuities or singularities, the most reliable benchmark solutions are analytical solutions.

Simply put, verification provides evidence that the conceptual model is solved correctly by the discrete-mathematics computer code without addressing whether the conceptual model has any relationship to the real world. Validation, on the other hand, provides evidence for how accurately the computational model simulates the real world for system response of interest. Verification, thus, is the first step of the validation process and is much less involved than the more complex statistical nature of validation. The statement given by Roache (1998) concludes this in a succinctly way: Verification deals with mathematics; validation deals with physics.

2.5.2 Calibration and validation

One definition of *calibration* is given by Trucano *et al.* (2006) as to adjust a set of code input parameters associated with one or more calculations so that the resulting agreement of the code calculations with a chosen and fixed set of experimental data is maximized (which also requires a quantitative specification of the agreement). As a comparison, the concept of *validation* can be interpreted as to quantify our confidence in the predictive capability of a code for a given application through comparison of calculations with a set of experimental data.

It is still unclear between the distinct difference between calibration and validation when both of them are eventually compared to the experimental data. Trucano *et al.* (2006) argued that it is dangerous to replace validation with calibration, and that validation provides information that is necessary to understand the ultimate limitations of calibration. Since calibration is the process of improving the agreement of a code calculation or set of code calculations with respect to a chosen set of benchmarks through the adjustment of parameters implemented in the code, it has been further claimed that calibration and validation can differ simply through the choice of benchmarks. It has been found by Velasco (1987) that a benchmark set can be chosen specifically to facilitate the act of calibration and need not be relevant to validation, or verification for that matter.

The fundamental purpose of benchmark is to draw specific conclusions from their comparison with calculations. In the case of verification, this purpose is to assess the mathematical accuracy of the numerical solutions. For validation, this purpose is to assess the physical fidelity for a stated application of the mathematical equations solved in the code. For calibration, the purpose is to choose parameter values that improve the agreement of the code calculations with the chosen benchmarks, in the belief that such tuned accuracy improvement will increase the believed credibility of the code (Trucano *et al.* (2006)). The choice of benchmarks must vary depending on the purpose of the comparisons.

2.6 Review of Thin Film Behaviour of Bitumen

Genin and Cebon (1998) performed a study of observation of crack surfaces in asphalt test specimens and have revealed that cracks in typical asphalt composite tend to run through the binder film rather than along the aggregate-binder interface, or through the aggregate itself. In practice, the binder consists of a mixture of bitumen and graded aggregate or filler. The bitumen is believed to be acting as an adhesive in the binder whilst the filler serves to stiffen it. Most approaches for describing constitutive behaviour of asphalt mixtures rely on empirical models that do not explicitly consider the complex nature of the interaction between aggregate particles separated by bitumen.

One approach towards modelling the deformation behaviour of mixtures with high volume fractions of rigid particles in a deformable matrix is to consider the microstructure of the composite as consisting of randomly distributed rigid aggregate particles, separated by thin films of bitumen (Cheung and Cebon, 1997). In this approach, it has been assumed that the deformation behaviour of each contact is primarily controlled by the mechanical properties of the bitumen film. Cocks (1994) reported that a bounding solution to the macroscopic behaviour can be obtained by a set of variational arrangements involving the microscopic behaviour of individual contacts and by an assumed compatible displacement field in the mixture.

It is therefore necessary to examine the constitutive behaviour of thin films of bitumen as a first step to understand the complex behaviour of asphalt mixtures. This section reviews the thin films behaviour of bitumen.

2.6.1 Stiffening factor

A thin film contact between adjacent aggregate particles can be idealised as two equivalent parallel rigid surfaces separated by a layer of bitumen whose thickness is assumed to be small compared with local radii of curvature of the particles. Cheung (1995) indicated the fact that in a contact between spherical particles the contact pressure decreases rapidly as the film thickness increases. As the film gets thinner, there is a stiffening effect, giving rise to an effective Young's modulus. For elastic contact behaviour in compression, Nadai (1963) suggested that the effective Young's modulus for an incompressible material subject to axisymmetric deformation is:

$$E_n^{ai} = \frac{E_m}{8} A^2 \tag{2.16}$$

where E_m is the Young's modulus of the film material and A is the aspect ratio, which is defined as the ratio of particle diameter to film thickness. The stiffening effect is most pronounced for incompressible films.

Cottrell (1964) analyzed the stress in a thin film of linear viscoelastic material while Cheung and Cebon (1997) derived solutions for the stresses in thin films of non-linear (power-law) viscous and viscoelastic materials in compression. Previous experimental results have shown that the nominal failure stress of axially loaded butt joints increases with declining film thickness. Kinloch (1982) stated that this is the case for a wide range of polymeric adhesives. Adams and Coppendale (1979) reported a similar observation with regard to the yield stress of ductile butt joints compared to uniaxial specimens. By using a von Mises yield criterion, the ratio of thin film of uniaxial yield stress was also found to increase with rising Poisson's ratio. However, Adams and Coppendale (1979) noted that the failure stress of brittle butt joints was lower than that of brittle uniaxial specimens due to the presence of stress concentrations on the joints. The tests performed by Dukes and Bryant (1969) showed that the fracture stress in joints with thicker films was lower than that in thinner films. Kinloch (1982) raised a hypothesis that the thin film stiffening effect was responsible for this rise in failure stress with aspect ratio.

Cheung (1995) suggested that for compressible material subject to axisymmetric deformation, the elastic behaviour of a compressible contact be conveniently summarised by the following empirical equation:

$$\frac{E_n^{ac}}{E_n^{ai}} = 1 - \left[1 + \frac{3}{8}\frac{K/E_m}{(5/8)A^2}\right]^{-1} \tag{2.17}$$

where K is the bulk modulus of film material. However, these approaches are only applicable for an elastic material that is subject to compression. For a viscous contact in compression, Cheung (1995) proposed a "thin film stiffening factor (ψ_s)" when the material is subjected to axisymmetric deformation:

$$\psi_s = \left(\frac{n}{2n+1}\right)\left(\frac{n+2}{2}\right)^{\frac{1}{n}}\left(\frac{A}{\sqrt{3}}\right)^{\frac{n+1}{n}} \tag{2.18}$$

where n is the power law creep component and A is the aspect ratio. The relationship between the thin film stiffening factor and the aspect ratio reproduced from Equation 2.18 is plotted in Figure 2.19. It should be noted that the equation 2.17 and 2.18 were only studied by using finite element (FE) analysis and no experimental validation has been reported. Harvey (2000) further modified the "thin film stiffening factor" by introducing the thick film adjustment with the following equation:

$$\psi_{sf} = \left(\frac{A}{A_0}\right)^{\frac{n+1}{n}} + 1 \tag{2.19}$$

where A_0 is a reference aspect ratio with a constant of 3.1 and $A < 8$ (for thick films). This is also shown in Figure 2.19 (as square symbols). It can be seen from this figure that the bitumen film stiffness increases at higher aspect ratios. Therefore, it has been concluded that the normal stiffness of bitumen film is dependent on the aspect ratio of the film.

2.6.2 Axial stress-strain response

Harvey and Cebon (2003) performed an extensive tensile testing on bitumen films to map out the fracture behaviour of 100 pen bitumen over a range of strain rates and temperatures. Two types of specimens were tested: Double cantilever beam joints (DCB) and butt joints and both ductile and brittle behaviour were investigated in the tests. For tests on bitumen films with aspect ratios (A) of 8 to 50, at temperatures 20°C, Figure 2.20 shows a power-law increase in peak stress with strain rate. It can be seen in this figure that thin film peak stress is essentially independent of aspect ratio, for the range of strain rate tested. This figure also reveals that there is similar rate dependence for thin film as for uniaxial samples (the thick solid line presents the thick film results whilst the thin solid line is uniaxial curve). Harvey (2000) proposed a power-law viscous equation by giving the normalised stress in a viscous film as a function of the normalised strain rate, as follows:

$$\frac{\sigma}{\sigma_0} = \psi_s \left(\frac{\dot{\varepsilon}}{\dot{\varepsilon}_0} \right)^n \tag{2.20}$$

Where the values of reference stress, σ_0, the reference strain rate, $\dot{\varepsilon}_0$ and the stiffening factor, ψ_s can be found in Harvey (2000).

A temperature-compensated strain rate was also proposed by Harvey (2000) to enable comparison of the results of constant strain rate tests at different temperatures. The temperature-compensated strain rate was defined as:

$$\dot{\varepsilon}_T = \dot{\varepsilon} \cdot \exp\left(\frac{-Q}{R} \left(\frac{1}{T_1} - \frac{1}{T_0} \right) \right) \tag{2.21}$$

Where an experimental result obtained at a strain rate of $\dot{\varepsilon}$ and a temperature T_1, is shifted to a temperature-compensated strain rate $\dot{\varepsilon}_T$ and at a reference temperature T_0. The value of the activation energy, Q and the universal gas constant R can be found in Harvey (2000).

Harvey and Cebon (2005) have claimed that there are three main regimes of behaviour of bitumen film in butt joints tests: ductile, brittle and transition. Their findings were summarised in Figure 2.21 where failure strain is plotted against $\dot{\varepsilon}_T$ (over fifteen decades of temperature-compensated strain rate) in a double logarithmic scale. It can be seen from this figure that the failure strain is film thickness and strain rate independent in either ductile or brittle region and is approximately 2.6 in the ductile region and 0.04 in the brittle region of behaviour (failure was defined as where the load fell to less than 10% of its peak value). It can also be seen in this figure that in the transition region the failure strain is generally film thickness independent, though the values cover the range from the ductile regime to those in the brittle regime.

It should be noted that although the thin film of bitumen plays an important part in characterising the contact behaviour of adjacent particles which are separated by thin film of bitumen, the stiffness stiffening effect has not been included in developing the numerical modelling in this thesis. However, a better understanding of the constitutive behaviour of bitumen as a thin film between contacting aggregates can provide a more realistic assumption in developing sophisticated contact models and this will be addressed in Chapter 8 for future research recommendations.

2.7 Summary and Conclusion

The literature review presented in this chapter indicated that the constitutive behaviour of asphalt mixtures at the macro-scale is reasonably well understood. It is time, loading rate and temperature dependent viscoelastic behaviour. Asphalt materials are usually assumed to be linear viscoelastic at small strain rates and/or low stress level. However, at large strain rates and/or high stress level the behaviour of asphalt mixtures are generally non-linear viscoelastic and cannot be directly modelled by a linear viscoelastic approximation. This understanding will be applied to model contact behaviour in Discrete Element Modelling (DEM) in this project.

A number of constitutive models based on continuum mechanics are available to describe the behaviour of asphalt mixtures. These models have been successfully applied in predicting the behaviour of asphalts, although large calibration factors are required. Nevertheless none of the aforementioned models has been shown to be adequately capable of comprehensively describing the behaviour of asphalts. It is likely that a greater insight into the performance of asphalt mixtures can be gained by a better understanding of micromechanics of asphalt at the aggregate level.

The principals of verification, calibration and validation within numerical modelling and simulations have been reviewed in this chapter. It has been revealed that verification is the assessment of the accuracy of the solution to a computational model while validation is the assessment of the accuracy of the computational simulation by comparison with experimental data. However, it has also been found that calibration cannot replace the validation to give a reasonable confidence in applying the modelling results to understand the real world.

2.8 Figures

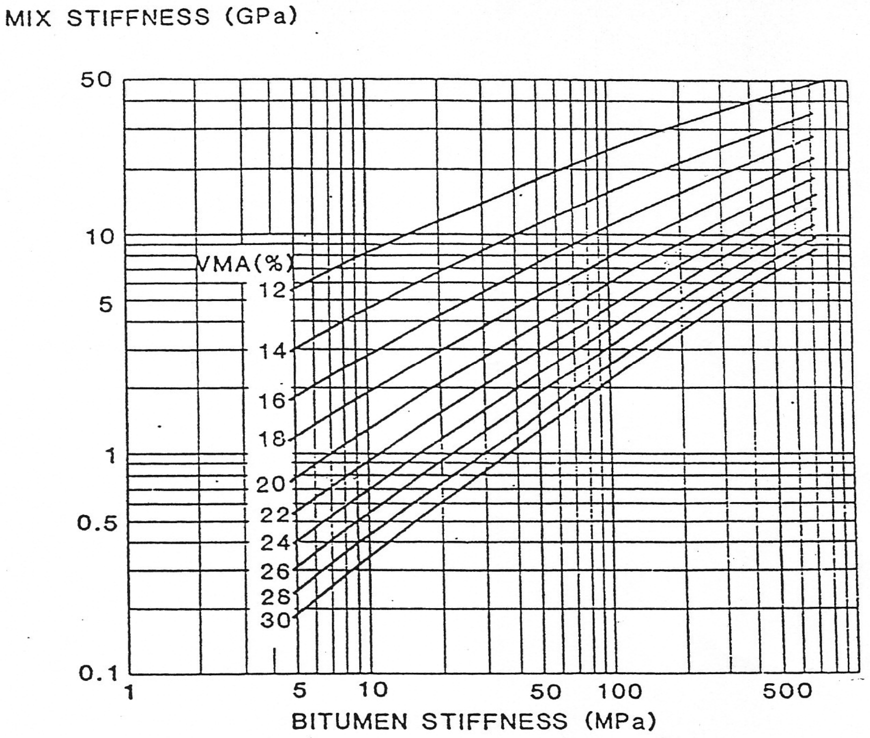

Figure 2.1: Nottingham Nomograph for the prediction of mix stiffness (Brown *et al.*,1986).

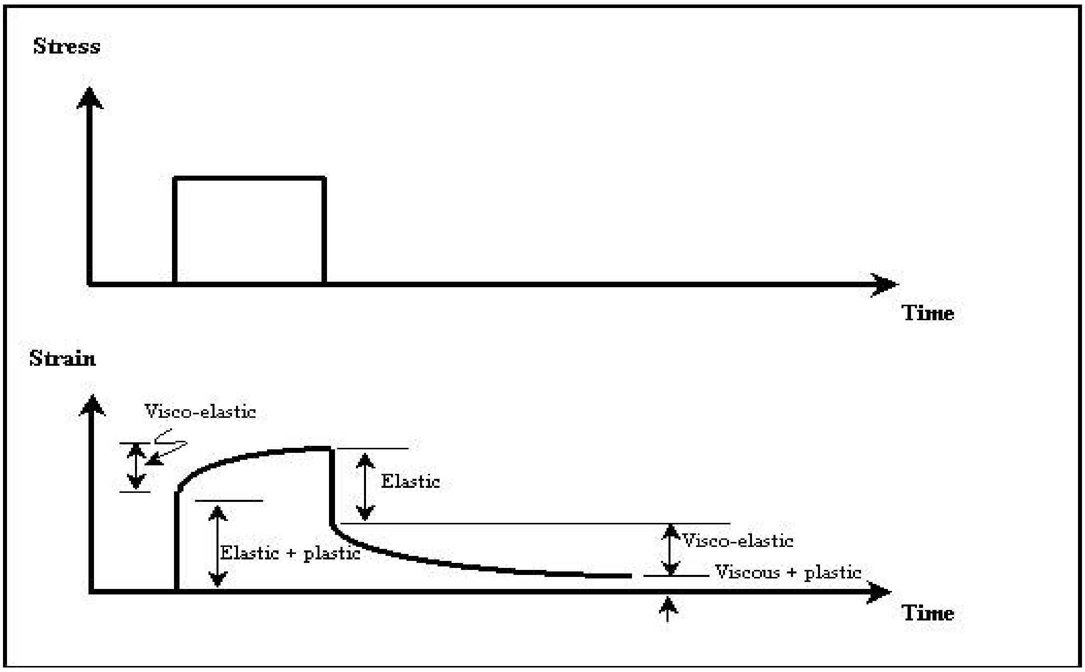

Figure 2.2: Strain response of asphalt mixtures under single load (Khanzada, 2000).

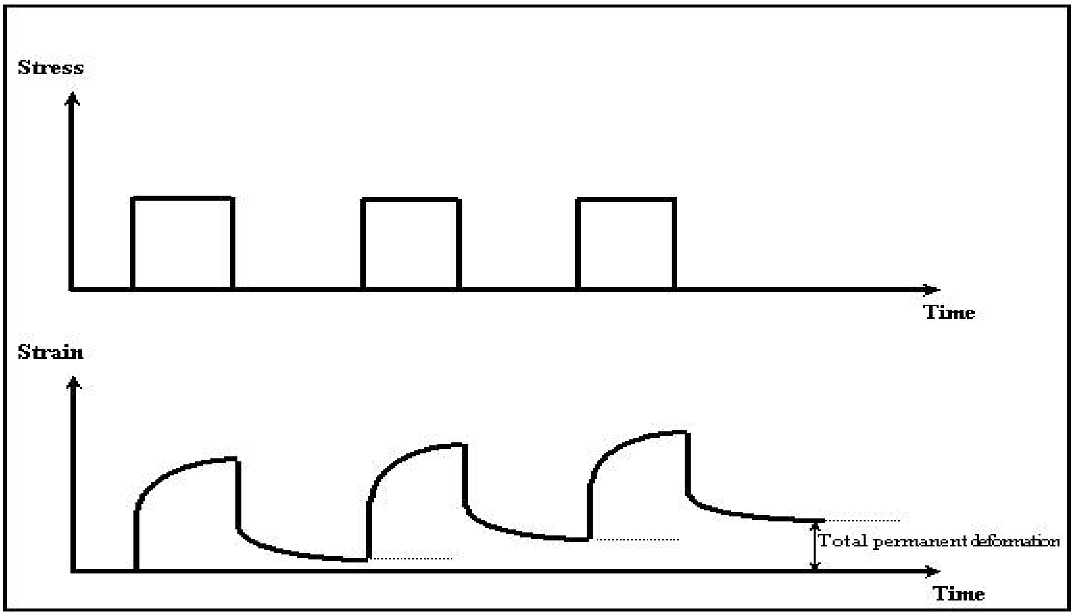

Figure 2.3: Accumulation of residual strain of asphalt mixtures under repeated load (Khanzada, 2000).

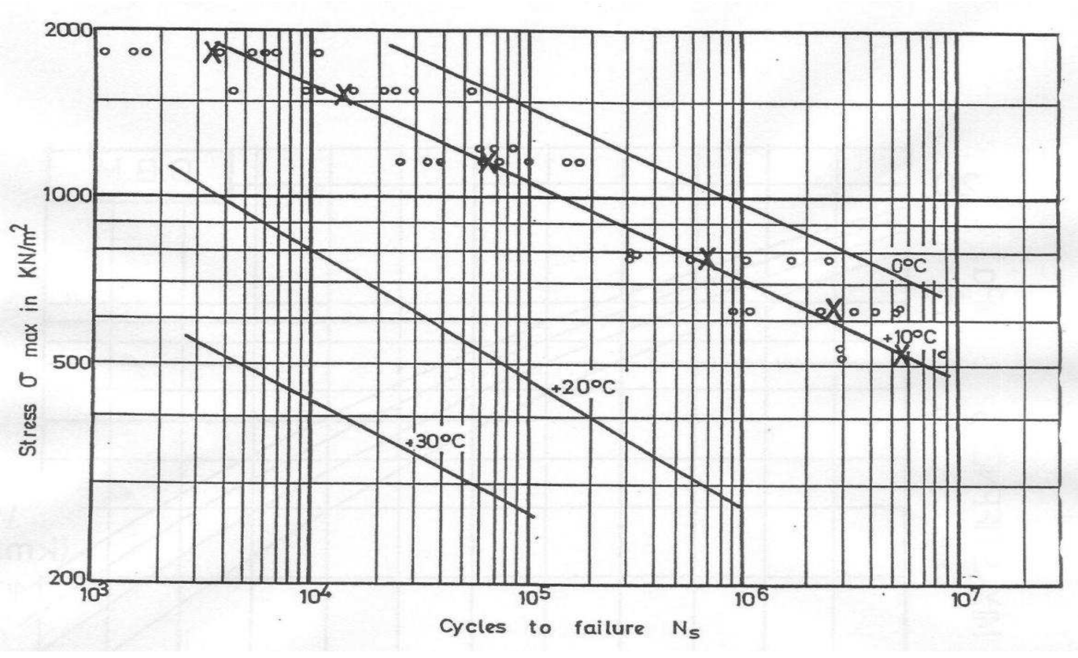

Figure 2.4: Typical fatigue lines in terms of initial stress (Read, 1996).

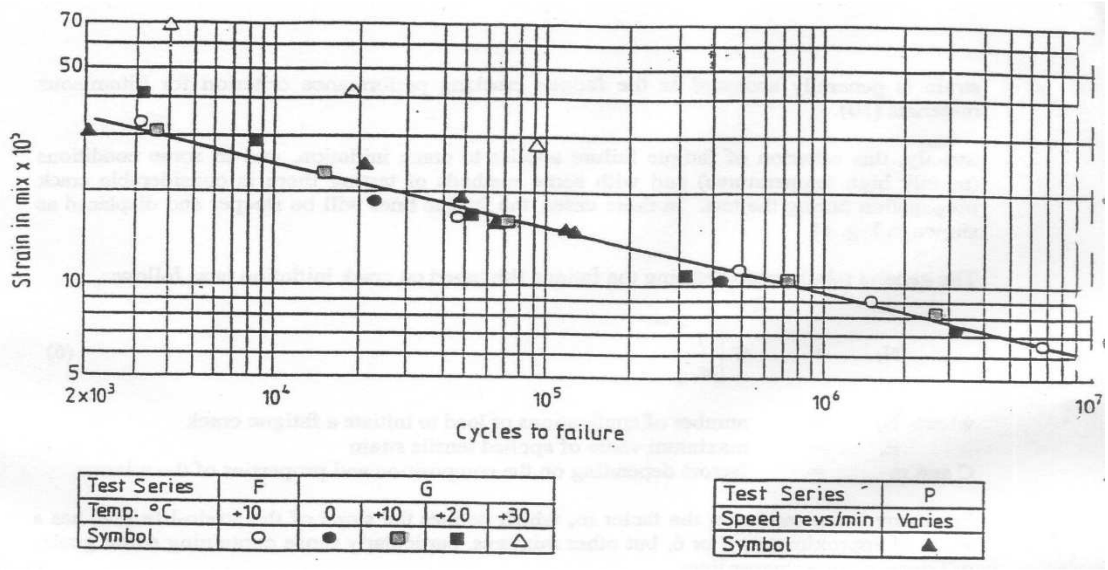

Figure 2.5: Typical fatigue lines in terms of initial strain (Read, 1996).

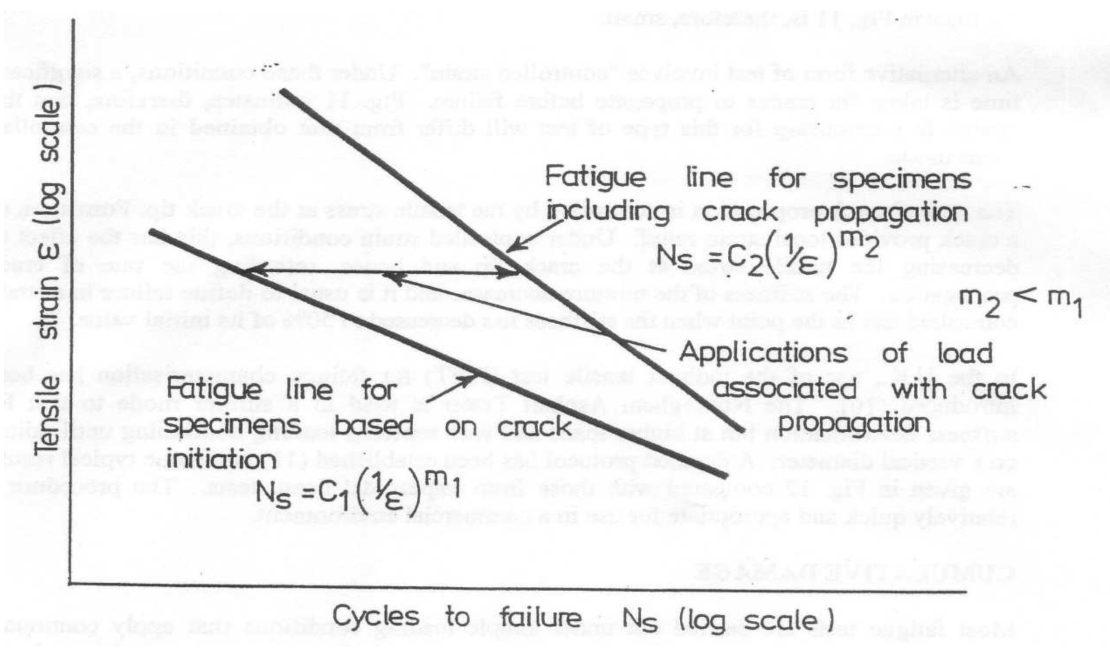

Figure 2.6: Effect of crack propagation on fatigue line (Brown, 1978).

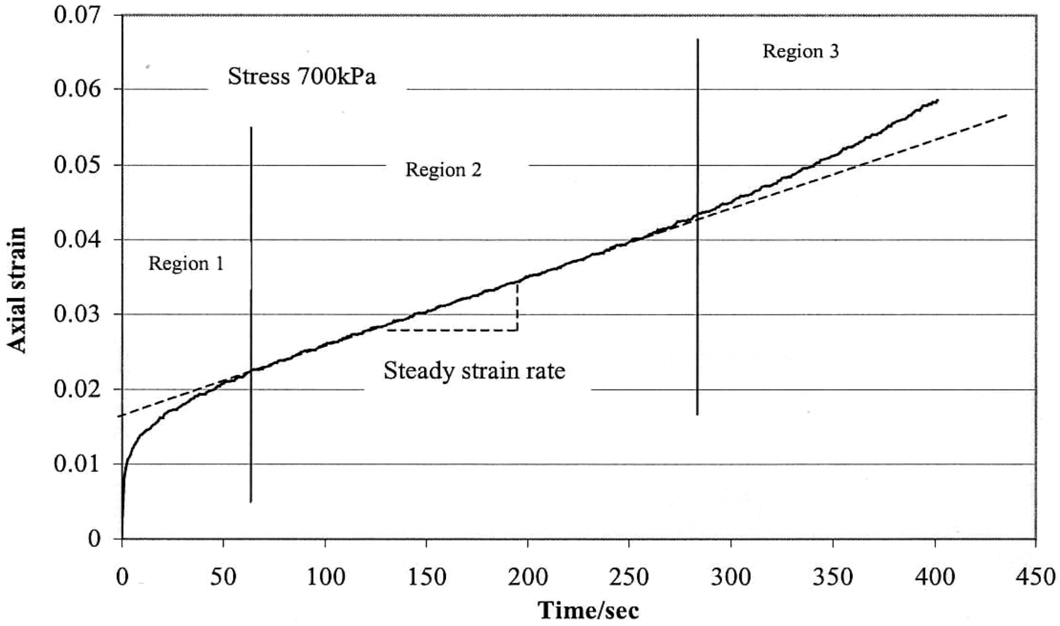

Figure 2.7: A typical creep test result of mixture *A/D* at 20°C (Khanzada, 2000).

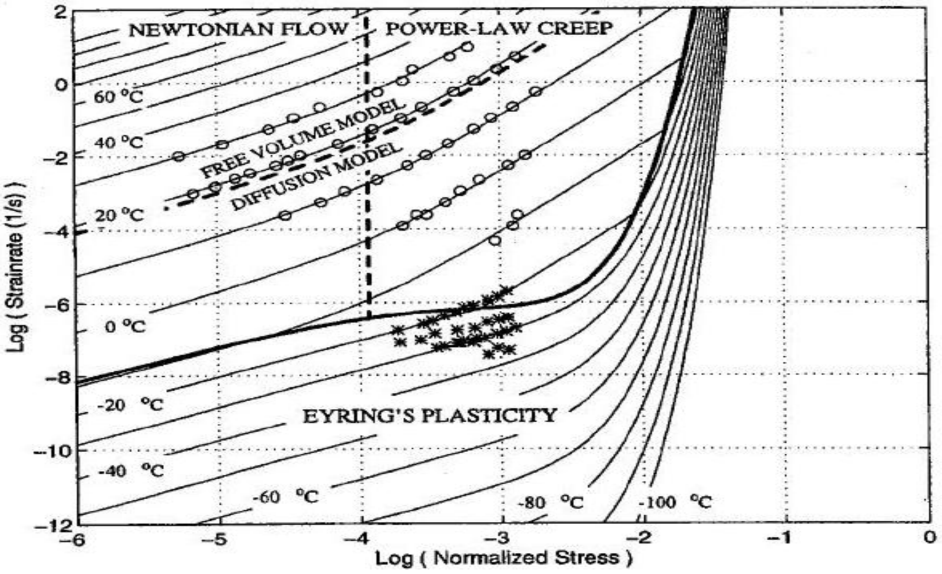

Figure 2.8: Steady-state stress and strain rate deformation mechanism map for bitumen in tension (Cheung, 1995); Stress is normalised by 1 *GPa*.

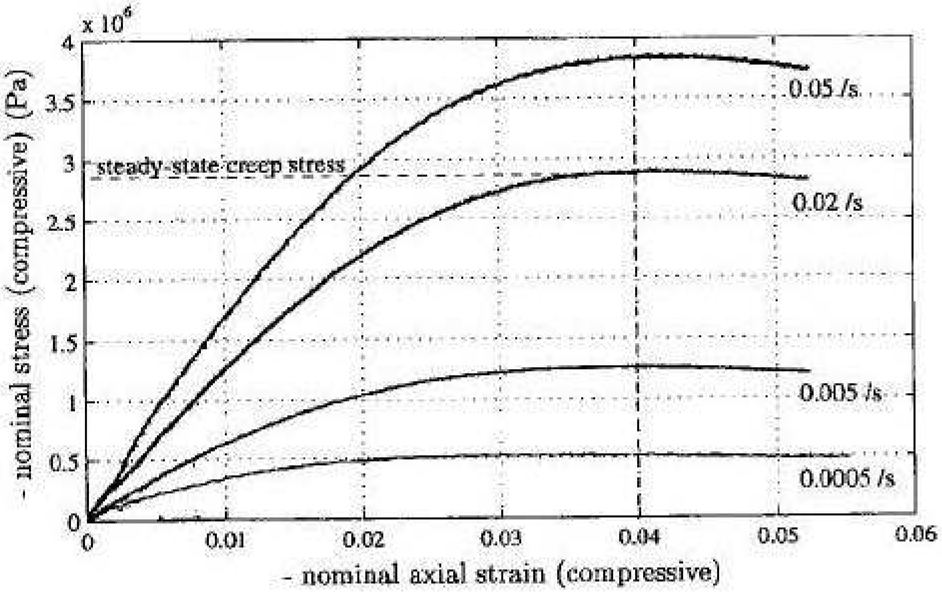

Figure 2.9: A typical data for constant strain rate tests of sand asphalt at 20°C (Deshpande and Cebon, 2000).

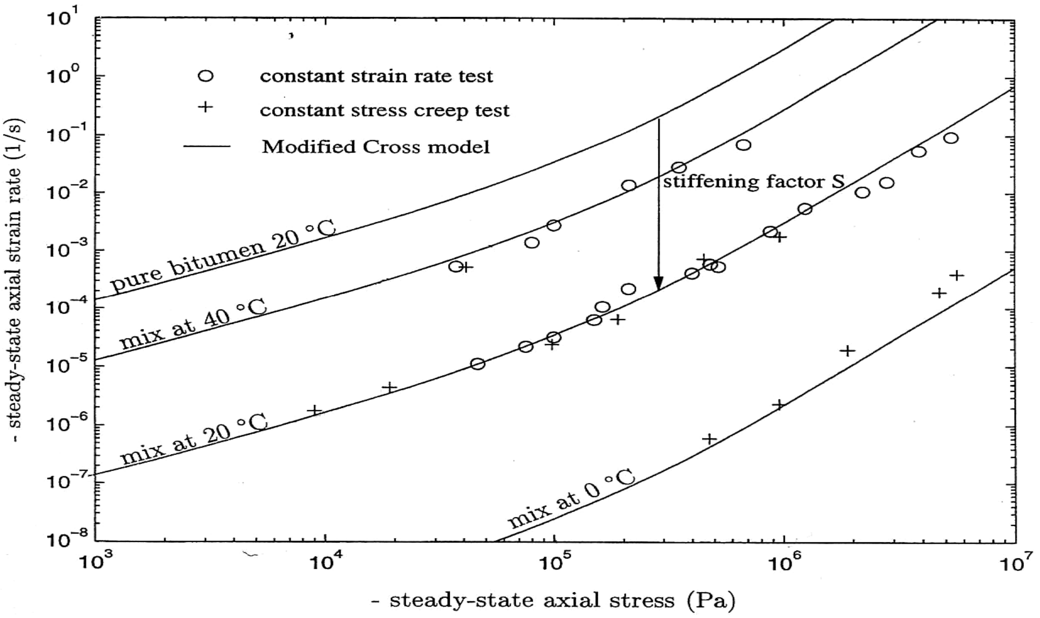

Figure 2.10: Deformation map of idealised mixture *A* (Deshpande and Cebon, 2000).

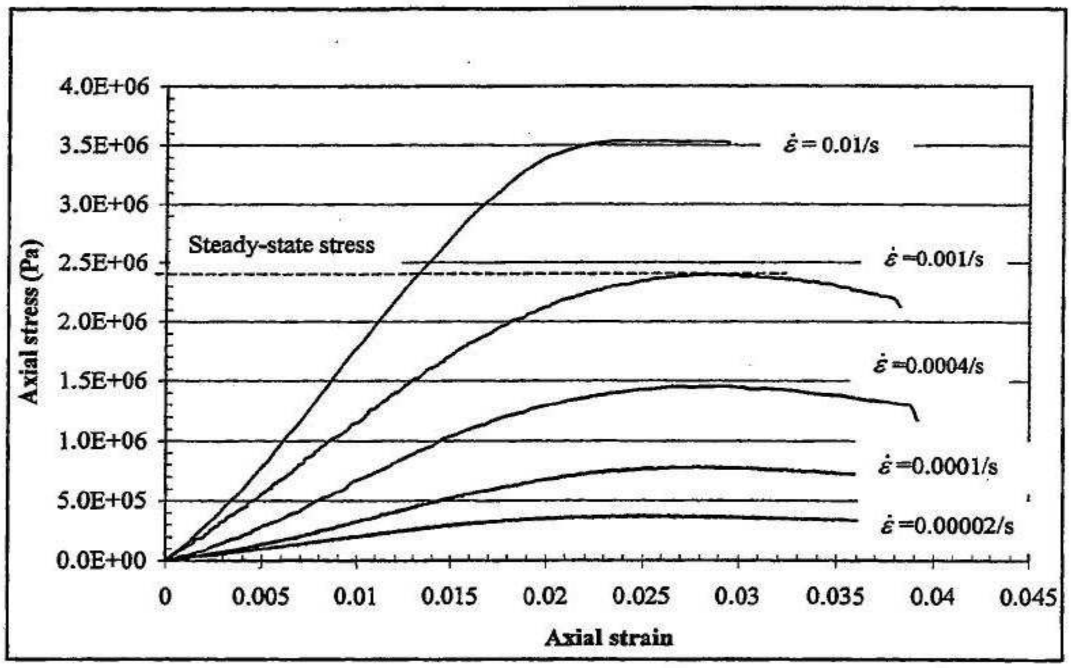

Figure 2.11: A typical result for constant strain rate tests in mixture *A/D* at 20°C (Khanzada, 2000).

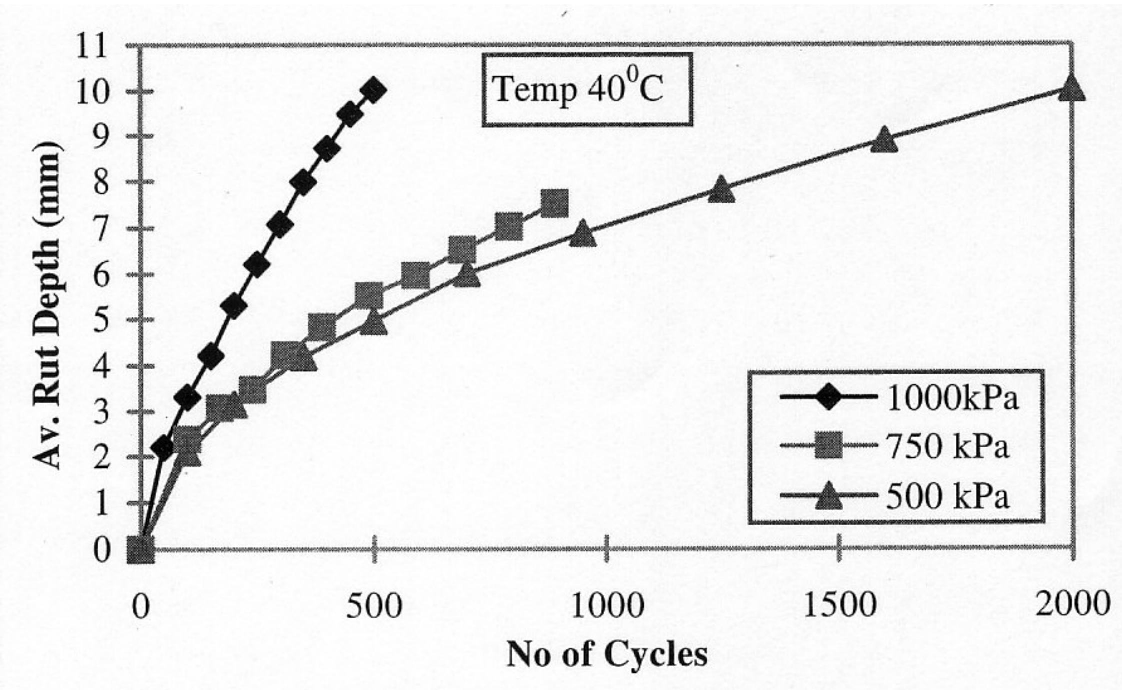

Figure 2.12: tracking test results for mixture *A/D* at 20°C (Collop and Khanzada, 1999).

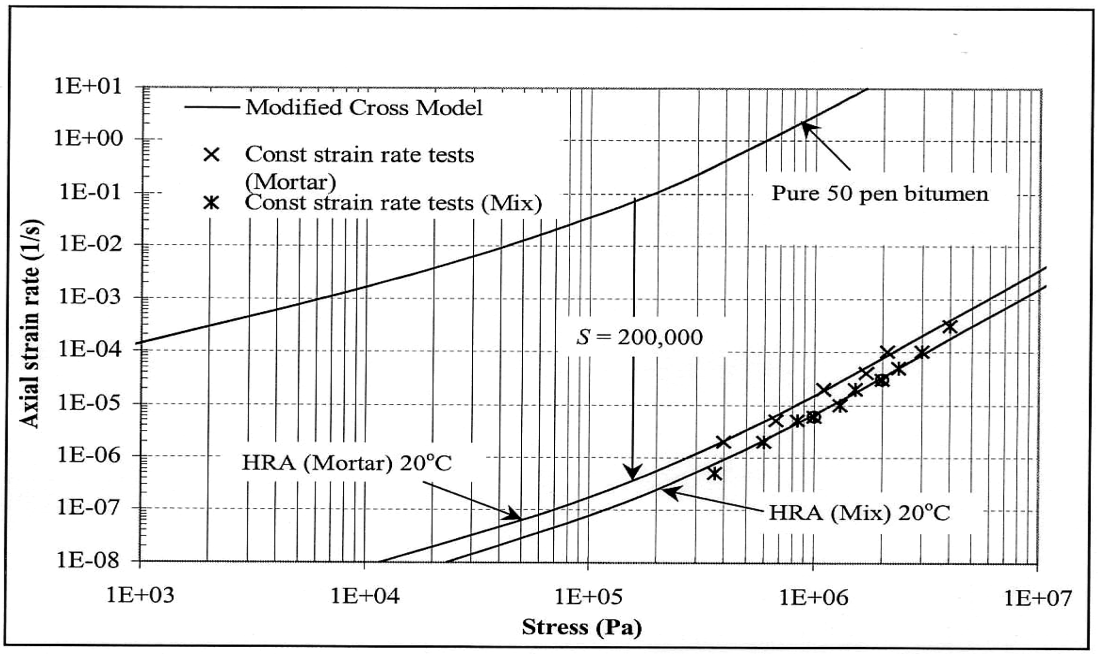

Figure 2.13: Steady state deformation behaviour of HRA mortar and mixture at 20°C (Khanzada, 2000).

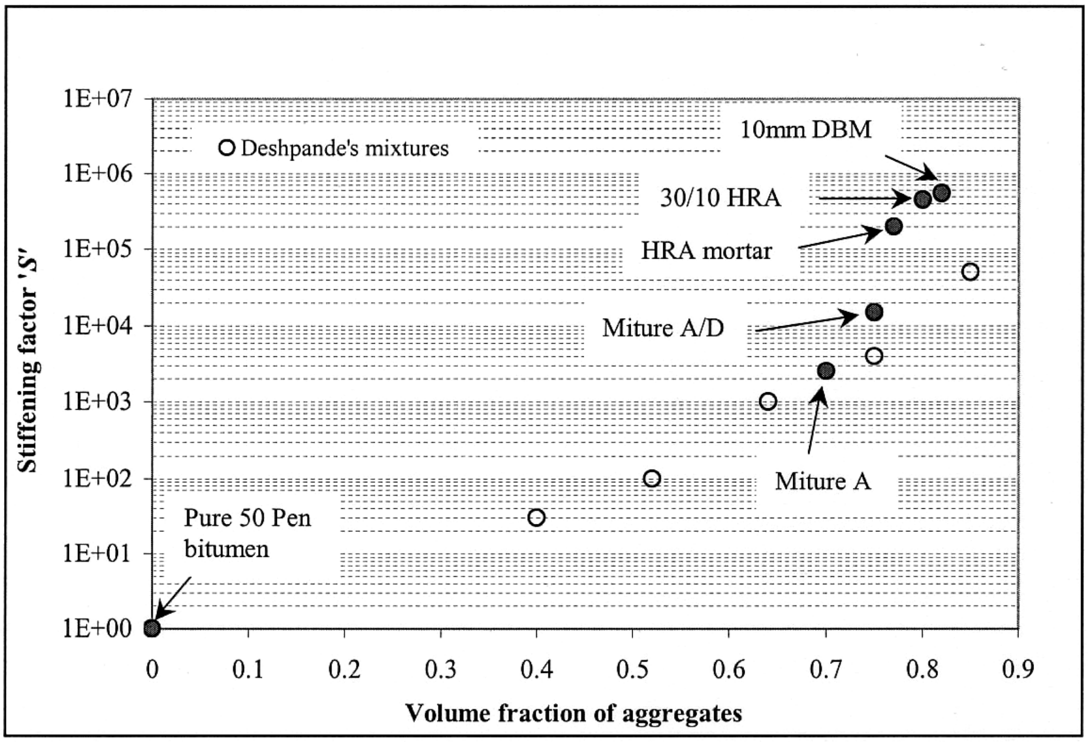

Figure 2.14: Variation of stiffening factor (*S*) with volume fraction of aggregate (Khanzada, 2000).

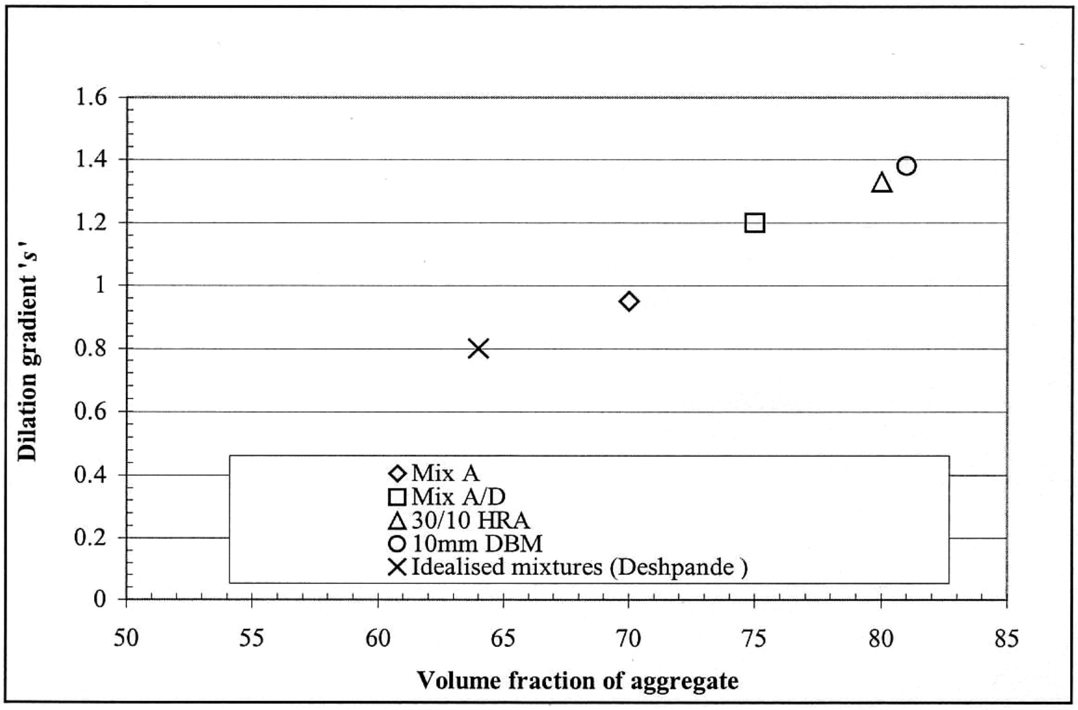

Figure 2.15: Variation of dilation gradient with volume fraction of aggregate (Khanzada, 2000).

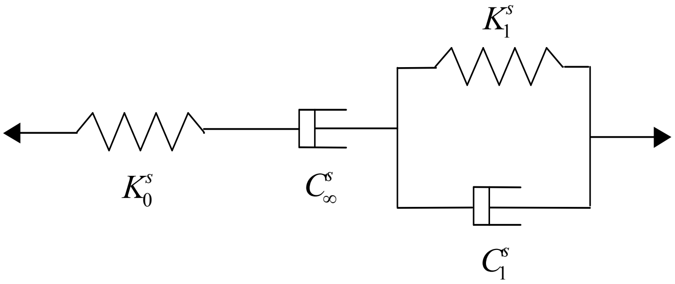

Figure 2.16: Generalised Burger's viscoelastic model in shear direction.

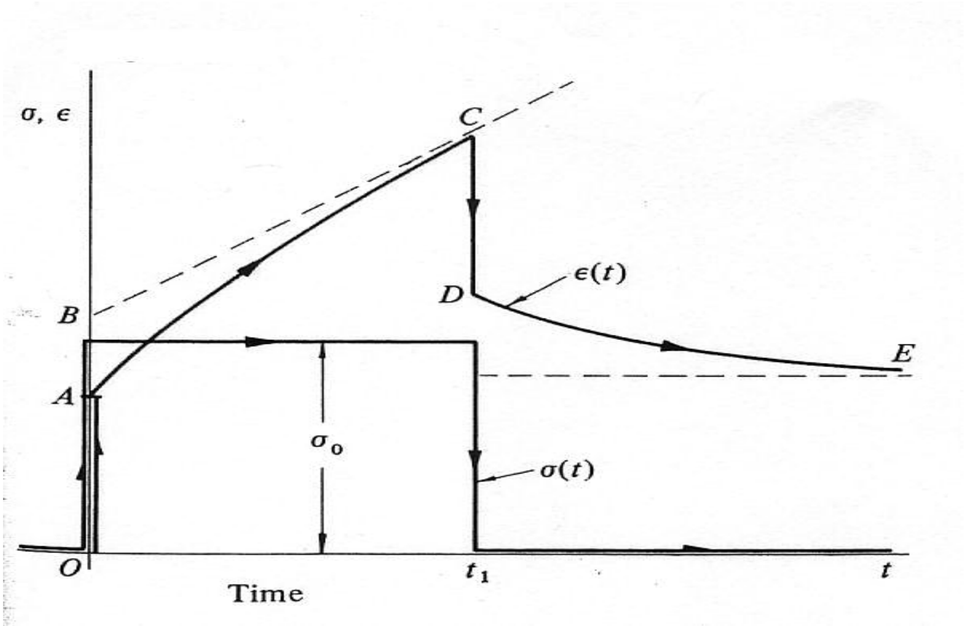

Figure 2.17: Viscoelastic response of stress and strain (Johnson, 1985).

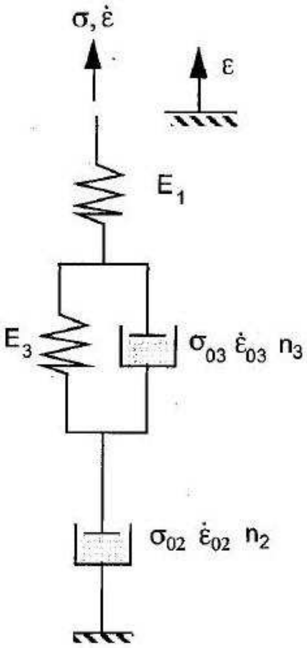

Figure 2.18: Sketch of 4-element spring-dashpot rheological model (Harvey 2000).

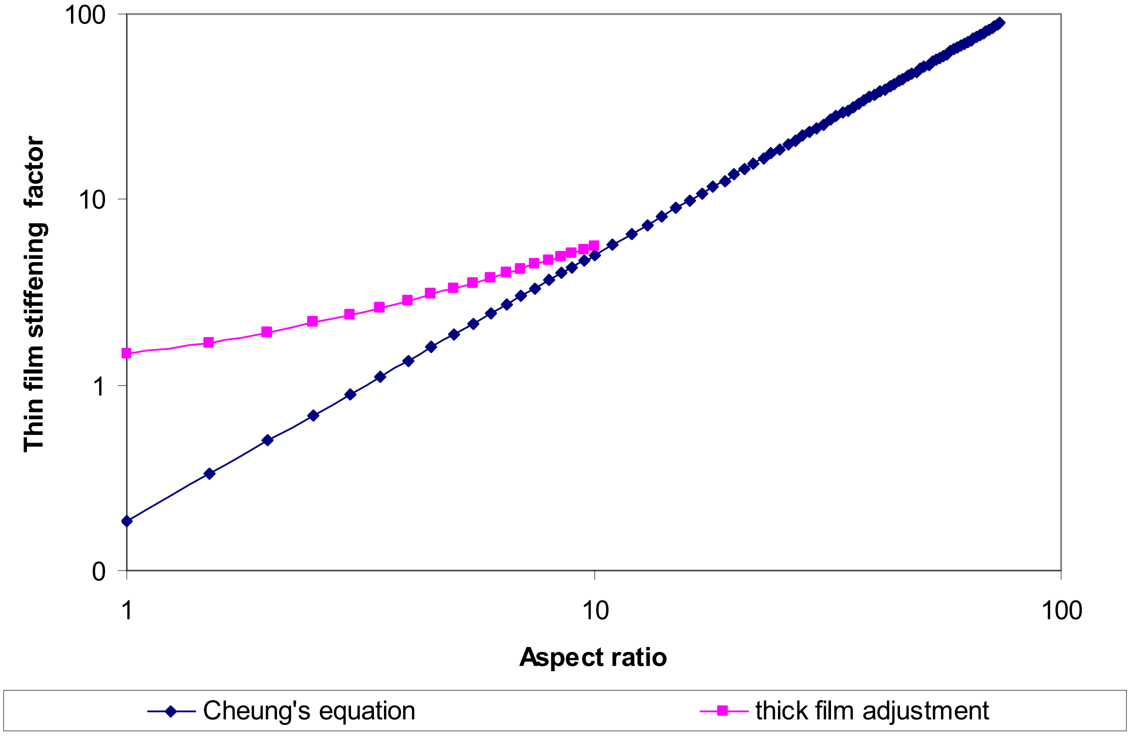

Figure 2.19: Thin film stiffening factor with thick film adjustment (Harvey 2000).

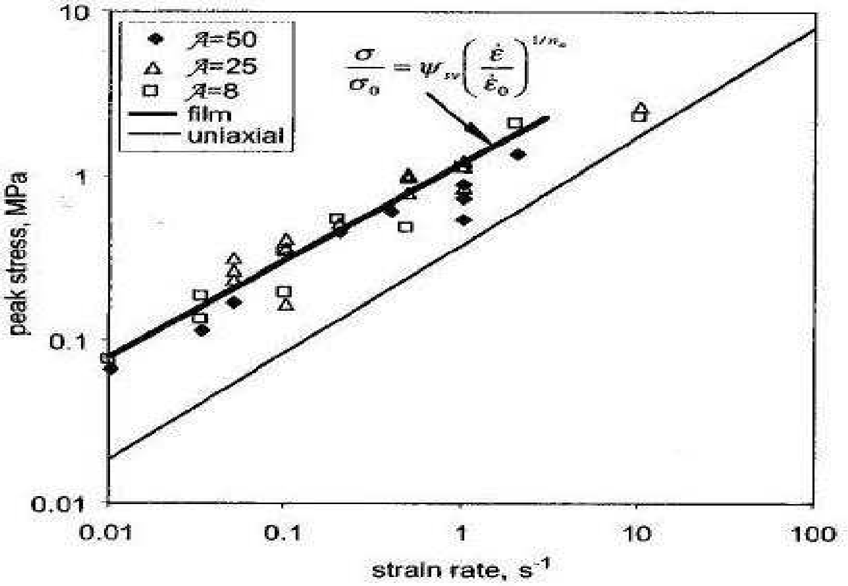

Figure 2.20: Plot of peak stress against strain rate for butt joints of side 25mm with films of three aspect ratios, compared with uniaxial results (Harvey 2000).

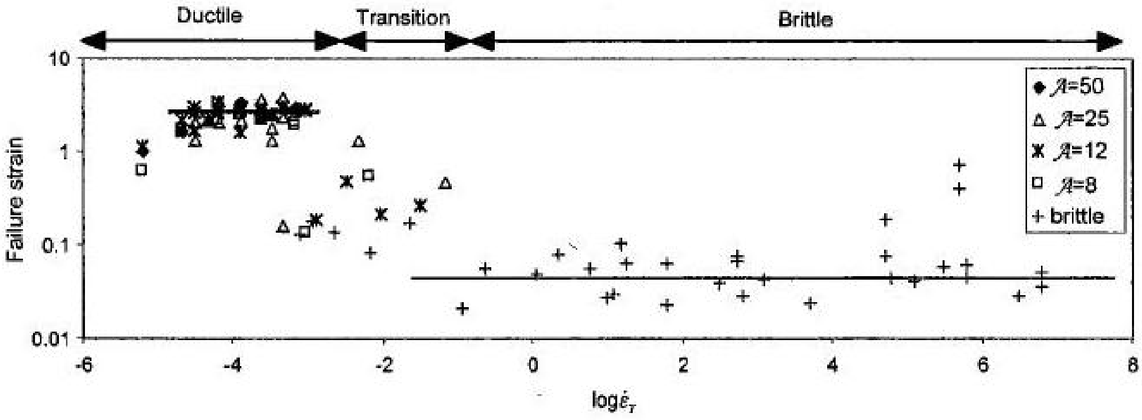

Figure 2.21: Performance of butt joints over a wide range of temperatures and strain rates (Harvey and Cebon, 2005).

3 *DISCRETE ELEMENT MODELLING*

3.1 Review of Micromechanical Model

The previous chapter reviewed the mechanical properties, constitutive behaviour of bitumen and asphalt and the constitutive continuum models of asphalt mixtures at present. The preliminary conclusion is that the traditional approaches are not capable of fully describing the comprehensive behaviour of asphalt materials. One of the major limitations with all the continuum approaches is that the micromechanical behaviour of the mixture is not explicitly included in this approach which means that it is not easy to relate observed behaviour to the micromechanics of the material. It also indicates a strong need to develop a new micromechanical model to better understand the constitutive behaviour of asphalt materials at the level of contacting aggregates. The following subsections review some of the micromechanical models that have developed to model the behaviour of asphalt mixtures in the past a few decades.

3.1.1 The three phase composite sphere model

The approach of micromechanical modelling of asphalt is poorly developed and the physical mechanisms of constitutive behaviour of asphalt are not well understood. Van der Poel (1954) reported an early attempt to model elastic behaviour of asphalt by using an assumed microstructure. A method developed for dilute dispersions by Frohlich and Sack (1946) was adopted by Van der Poel to calculate the rigidity of a concentrated solution of elastic spheres in an elastic medium. While the reported results show good agreement with experiments for volume fractions of aggregate up to 60%, certain errors in the calculation technique were later reported by Christensen and Lo (1979).

3.1.2 The bitumen film creep model

Hills (1973) developed a micromechanical model for modelling creep behaviour of asphalt mixtures. He proposed a theoretical model considering bitumen as forming a binder layer between a pair of adjacent particles (See Figure 3.1). In this model, the internal structure of the asphalt mixture is described in terms of the bitumen film thickness, and the evolution of this state variable as a function of the macroscopic straining of the material. The macroscopic strain of a mixture was assumed to be accommodated on a microscopic scale by displacements of adjacent particles in both shear and compression. These displacements were assumed to be independent of each other. During deformation the macroscopic strain of the mixture was only related to the shear displacements of adjacent particles and the rate of strain was dependent on the magnitude of stresses, the thickness of bitumen (which changes as a function of time) and the bitumen properties. The bitumen was modelled as an incompressible, linear viscous fluid. He indicated that this model had a good agreement with experimental results and was capable of modelling linear, shear and volumetric strains in uniaxial compression tests.

Hills' model was based on an empirical estimation of evolution of film thickness under deformation, rather than on a theoretical analysis of thin film bitumen deformation. The general form of the constitutive equations proved by this model is therefore, depending entirely on curve fitting to experimental data. A method was developed by Collop (1994) and Collop *et al.* (1995) to obtain the parameters for Hills' model from fundamental mixture parameters (e.g. *VMA*). Collop *et al.* (1995) used this modified model to estimate the rutting of flexible pavements undergoing accelerated tests and good agreements were reported.

Following the idea of Hills, Cheung *et al.* (1999) used the isolated contact modelling approach to analyze the deformation behaviour of asphalt which is idealised as a random distribution of rigid spheres separated by thin films of bitumen. A qualitatively good agreement was reported between predictions from this model and the experimental results, although the isolated contact model substantially underpredicted the “stiffening” effect of the aggregate.

3.1.3 Microstructure model

Saad *et al.* (2002) indicated that the load carrying behaviour in an asphalt mixture is related to the local load transfer between aggregate particles, and this is taken as micromechanical response. They developed a micromechanical model to simulate the asphalt microstructure by replacing the aggregate/binder system with an equivalent finite element network that represents the load carrying behaviour between aggregates in the multi-phase material. They assumed there is an effective binder zone between neighbouring particles through which the micromechanical load transferring occurs between this particle pair. A representative model has been introduced based on some simplified assumptions. An elliptical aggregate model as shown in Figure 3.2(b) has been presented to replicate a typical asphalt material (Figure 3.2(a)). After that, two models were developed. The first model incorporated a network of frame elements which were connected by a special stiffness matrix to predict the load transfer between connected particles, as shown in Figure 3.2(c). The second model incorporates the commercial ABAQUS finite element code using a rectangular strip to simulate the effective binder zone, Figure 3.2(d). As shown in Figure 3.3, this model employed four-node quadrilateral elements to simulate binder and two-node rigid elements to model aggregate.

Experimental verification has been conducted on specially designed compression and indirect tension samples, which allow the measurement of aggregate displacement and rotations using video image and computer analysis. As a result, they stated that the model simulation of these tests give results that compared favourably (within 1.5 to 7%) with the experimental data, which indicating a good agreement. However, this model is limited to the two-dimensional behaviour of asphalt mixture.

3.1.4 The discrete element model

The Discrete Element Method (DEM) was first introduced by Cundall (1971) for the analysis of rock mechanics problems. DEM is a numerical technique capable of describing the mechanical behaviour of assemblies of discs and spheres. It is implemented in a computer program which allows finite displacement and rotation of discrete bodies. This method refers to a particular discrete element scheme and by tracing the individual particle displacement, contact forces and displacement of a stressed assembly of particles can be determined. The movements of particles were caused by the propagation of disturbance from wall and particle motion throughout the particle system. A number of researchers, for example Rothenburg and Bathurst (1992), Chang and Meegoda (1993), Sitharam (1999), Buttlar and You (2001), Ullidtz (2001) and Collop *et al.* (2004, 2006) have attempted to model bituminous mixtures using DEM. More reviews of applications of DEM in soil and asphaltic materials are presented in the following sections.

The following section in this chapter presents a detailed review of the development and application of DEM in soil and asphaltic materials (Section 3.2). It is then followed by the detailed description of a specific program in DEM, Particle Flow Code in 3D (PFC3D), in section 3.3. The basic calculation procedure in PFC3D is given in sub-section 3.3.2. A mechanical time-step is introduced to represent the dynamic behaviour in DEM and a detailed description of the servo-control mechanism is given in sub-sections 3.3.3 and 3.3.4, respectively. An elastic contact model and a Burger's viscoelastic contact model are described in sub-sections 3.4.1 and 3.4.3 respectively, together with description of contact bond in sub-section 3.4.2.

3.2 Development and Application of DEM

3.2.1 Application of DEM in soil mechanics

The Discrete element method has been widely applied in soil and rock mechanics. In the early 70's, Cundall (1971) introduced a computer program to model the progressive failure of a discrete block system where interaction between blocks is governed by friction and stiffness. In his research, the basic DEM theories such as the force-displacement law, the law of motion and the calculation cycle were introduced.

In the late 70's, Cundall and Strack (1979a) developed a computer program, BALL in two dimensions by incorporating the DEM theory described in (Cundall, 1971).

BALL was used to model the granular assemblies comprised distinct particles which displace independently and interact only at contact points. The effects of damping and speed of loading were also investigated and then the model was validated by comparing force vectors obtained from photoelasitc analysis undertaken by de Josselin de Jong and Verruijt (1969). The BALL program was further developed by Cundall and Strack (1979b) to simulate the behaviour of assemblies of discs under conditions of loading and unloading. By using computer interactive graphics the internal mechanism within a granular mass and the response to stress probe has been studied which led to the development of constitutive law for soil. Cundall concluded that DEM and BALL were valid tools for research into the behaviour of granular assemblies.

In the early 80's, Cundall *et al.* (1982) further developed the BALL by improving methodologies for measurement of granular assemblies in simulation. Various forms of boundary conditions and determinations of average stresses and strains were described. A catalogue of observed mechanisms such as force chains, particle rotations and locked-in shear force were presented at the particle interaction level while macroscopic effects (e.g. friction and fabric on dilation) were also investigated. In the late 80's, Cundall (1988a, b) developed a DEM program called TRUBAL to extend the simulation to three dimensional assemblies. TRUBAL were used to generate a dense random packed assembly of spheres to the desired porosity. A numerical 'servo-control' algorithm was introduced to equilibrate the sample under the desired isotropic stress. Biaxial tests were performed and a good agreement was obtained between the numerical results and the experimental results proposed by Ishibashi and Chen (1988). However, there was a discrepancy in volumetric strain between the numerical results and results from triaxial extension tests. Cundall explained that this was due to the presence of an initial fabric in the physical sample.

The first version of PFC3D for DEM simulations was released in 1995 by the Itasca Consulting Group Inc. Hazzard *et al.* (2000) used PFC3D to analyse the crack nucleation and propagation in brittle rock. In their paper, the mechanical behaviour of different rock types has been well reproduced by considering the micromechanical structure of different rocks. The cracking of rock models has also been examined and the cracking pattern has been found to agree with laboratory results.

McDowell and Harireche (2002a, b) used PFC3D to model the fracture of soil grains. They modelled a soil particle as an agglomerate of balls bonded together with a contact bond, shown in Figure 3.4. In order to replicate the real soil particle crushing experiments realistic particle parameters and gravity were used in agglomerate preparation. They demonstrated the possibility of obtaining the correct size effect on sample strength. They further used PFC3D to model one dimensional normal compression of sand. Odeometer tests have been performed on small and large agglomerates and they concluded that the yield stress tends to decrease by increasing the agglomerate size. Furthermore, the yield stress predicted by the model was lower than the experimental results and they explained the phenomenon that it is probably due to the different shape of agglomerate compared to real sand. As a result, they concluded that DEM with PFC3D is a powerful tool in modelling the behaviour of crushed soil particles and it is capable of providing the micromechanical insight into the further soil behaviour.

Powrie *et al*. (2005) used PFC3D to capture the essential macro-features of soil behaviour as observed from laboratory tests. They modelled each particle as two spheres bonded together with a high strength bond so that each pair of spheres behaves as a single rigid particle, as shown in Figure 3.5, and prepared a sample by joining many of this sphere pairs together for biaxial simulations, as shown in Figure 3.6. The effects of loading platen friction, initial sample porosity and inter-particle friction angle were investigated. They found that the peak effective angle of friction and volumetric dilation of the sample increased proportionately with the particle shape factor (defined as $(R+r)/R$ in Figure 3.5). They concluded that a numerical sample with 10,000 particles comprising pairs of bonded spheres of shape factor 1.5 and inter-particle friction angle of 26° have demonstrated the ability to model the behaviour of soil as observed in the laboratory.

McDowell *et al*. (2005) utilised the DEM to model the geogrid-reinforced aggregate using computer code PFC3D. A model for the geogrid was developed by bonding many small balls together to form the desired geometry and evaluated by simulating standard tests. They modelled the interaction between ballast and geogrid by simulating pull-out tests and compared with experimental data. The peak mobilised resistance and the displacement necessary to mobilise peak pull-out force was well predicted by this model. Additional simulations were performed on the large-scale pull-out tests and cyclic triaxial tests to examine the zone of influence of the geogrid and they concluded that the DEM holds much promise as a tool for investigating ballast-geogrid composite system.

Lu and McDowell (2008) successfully applied DEM in modelling the mechanical behaviour of railway ballast under triaxial conditions. Lu and McDowell reported that the effects of particle shape and interparticle friction in modelling shear behaviour of ballast can be realised by introducing weak parallel contact bonds between clumps and that realistic volumetric change can be modelled by adding breakable asperity to the main body of a particle. In particular, they have indicated that the monotonic shear behaviour of railway ballast can be correctly modelled under a range of confining pressures, providing micromechanical insight into the behaviour.

3.2.2 Application of DEM in asphalt

The Discrete element method (DEM) is an approach capable of modelling the micromechanical behaviour of an asphalt mixture. This method has been widely used in soil and rock materials and attempts have been carried out in modelling asphalt mixtures during the past decades. A few applications of DEM in simulating asphalt behaviour are reviewed in this subsection.

Rothenburg and Bathurst (1992) invested a micromechanical model of asphalt in which the material is represented as a set of discrete elastic particles bonded with viscoelastic bitumen. In this model, the binder was treated as an incompressible fluid and an aggregate/binder interaction model was developed to represent the behaviour of asphalt concrete. They performed a few simulations of creep tests and reached the conclusion that the asphalt exhibits steady state creep when the number of frictional contacts is below a certain minimum.

Chang and Meegoda (1993) presented a microscopic model, ASBAL, based on the discrete element method (DEM). In order to represent the asphalt mixture (HMA in their simulations), they introduced a viscoelastic element, Burger's element (which consists of a Maxwell element and a Kelvin element), to simulate experimental tests with different microscopic parameters under varied types of loading such as monotonic and cyclic loading. They showed that under monotonic loading, a typical HMA test exhibits non-linear behaviours and permanent deformation was modelled under cyclic loading. Meegoda and Chang (1994) extended this model to investigate the temperature influence on stress-strain behaviour and internal structure of hot mixed asphalt. They simulated compression tests under four different temperatures and concluded with the higher strength and stiffness at lower temperatures.

Buttlar and You (2001) used DEM to develop a two-dimensional model of an indirect tension test which comprises 130 cylindrical stones (12.5mm in diameter) arranged in a hexagonal packing structure glued together with asphalt mastic (See Figure 3.7). They validated predictions with experimental data (for the same material) and obtained a good agreement. Buttlar and You (2001) extended this approach to develop a microfabric discrete element modelling (MDEM) to simulate the Stone Mastic Asphalt (SMA) microstructure. This approach is a two-dimensional model extended from a traditional DEM approach, where various material phases are modelled with clusters of very small discrete elements. The two dimensional aggregate geometry of the mixture has been captured with a high-resolution optical scanner. However, this model is proved to under-predict mixture stiffness, since each particle (aggregate) is assumed to be coated with matrix material and calibration technique is not sufficiently accurate (Buttlar and You, 2004). Lately, they developed a technique to calibrate the MDEM model to experimental results by expanding aggregates to create additional aggregate contact. This improvement is shown to provide better modulus estimates and believed to be more representative of the actual three-dimensional behaviour (Buttlar and You, 2004).

Collop *et al*. (2003, 2004) presented a DEM model to investigate the use of PFC3D to simulate the behaviour of a highly idealised asphalt mixture (containing single-sized sand mixed with bitumen) in uniaxial and triaxial compression creep tests. A numerical sample preparation procedure has been developed and both elastic and viscoelastic simulations have been carried out to investigate the behaviour of permanent deformation of this asphalt mixture. They found that a sample containing 4500 particles is required for the Young’s modulus and Poisson’s ratio to be within

2% of the values calculated using a much larger number of particles (Collop *et al.,* 2003; Lee, 2006). They also found that the bulk modulus was linearly dependant on the normal contact stiffness and independent of the shear contact stiffness. Poisson's ratio was found to be dependant on only the ratio of shear contact stiffness to the normal contact stiffness. They stated that the numerical results have all been validated with the experimental data (Collop *et al.,* 2004).

Collop *et al*. (2006) further developed the DEM 3D model to simulate the dilation behaviour of uniaxial creep tests in an idealised asphalt mixture. A viscoelastic Burger's model has been adopted in their simulations. They have found that the dilation gradient under uniaxial conditions increases as the ratio of compressive to tensile contact stiffnesses increase as a function of time in the viscoelastic simulations. The simulation results have been compared to experimental results and a good agreement has been found.

Kim *et al.* (2008) developed a cohesive zone model with viscoelastic properties which was implemented in 2-D DEM and used this model to simulate the fracture behaviour of asphalt concrete in a disk-shaped compact tension test. They concluded that viscoelastic DEM simulations were found to realistically capture rate effects in the fracture of asphalt mixtures at low temperatures. They also found that the use of a heterogeneous microstructure combined with a viscoelastic bulk material would lead to better agreement with experimental data.

Mahmoud (2008) introduced an approach that combines DEM and image processing techniques to model the resistance of asphalt to fracture. This approach was used to determine the internal forces that develop within the aggregate structure under loading. It was concluded that a high rate of increase in forces indicates less breakage of aggregate particles and vice verse. However, their findings are limited to stone-to-stone contact between coarse aggregate particles (e.g. HMA) and the simulations were 2-D in nature.

Most of approaches that utilises DEM to model asphalt mixtures are restricted to two-dimensional (2-D) whilst 3D model is still poorly developed at present. Since asphalt is a complex multiphase mixture that its component is physically structured 3D in nature, there is a strong need to develop a 3D DEM in modelling asphalt mixture providing well understanding of contact mechanism in asphalt.

3.3 Particle Flow Code in Three Dimensions (PFC3D)

3.3.1 Introduction

PFC3D has been developed by ITASCA Consulting Group Inc. to model movement and interaction of stresses in assemblies of rigid spheres. It is classified as a Discrete Element Code by Cundall and Hart (Cundall and Hart, 1992) since it allows finite displacements and rotations of discrete bodies.

PFC3D can be adopted to simulate the mechanical behaviour of a system comprising a series of particles. A particle represents a body that occupies a certain amount of space. In this approach, each distinct particle displaces independently and interacts with others only at contacts. The particle is assumed to be rigid but can deform locally at contact points whose behaviour is controlled by the contact force calculated based on the overlapping magnitude and contact stiffness in normal and shear direction. In PFC3D, spherical particles are referred as ‘balls’ while boundaries are referred to as ‘walls’. The balls and walls interact with each other via the similar contact force mechanism as a ball-ball contact.

Damage behaviour in PFC3D can be modelled by introducing bonds at contacting points where the bond breaks when inter-particle forces at contact exceed a specified bond strength in either normal or shear direction. This allows tensile forces to be developed between particles and includes the formation of micro-cracks in the modelling. Macroscopic behaviour can be modelled by treating a solid as an assembly of many small particles and stresses and strains can be measured by averaging their quantities over a representative measurement volume.

3.3.2 Basic calculation cycle

The PFC3D calculation cycle is shown in Figure 3.8. This cycle is based on a time stepping algorithm which requires the repeated application of a force-displacement law to the contacts, the law of motion to each ball and a constant updating of wall positions. The contacts (ball-ball and ball-wall) are traced during the simulation and they can be formed or removed automatically. At the start of a time step, the contact forces are updated based on relative motion between two contacting balls via a force-displacement law. The law of motion is then applied to update the velocity and position of each ball based on the resulting force and moment arising from contact and body forces acting on the ball. The force-displacement law and the law of motion are described in the following sub-sections.

Force-displacement Law

The force-displacement law is described for contacts between both ball to ball and ball to wall. The law is applied at the start of each cycle to contacts to obtain new contact force. The contact forces vector F_i is resolved into normal and shear components with respect to the contact plane:

$$F_i = F_i^n + F_i^s \tag{3.1}$$

where F_i^n and F_i^s denotes normal and shear components respectively. The normal contact force vector is given by:

$$F_i^n = K^n U^n n_i \tag{3.2}$$

where K^n is the normal contact stiffness, U^n is the overlapping magnitude of two contacting balls and n_i is the unit normal vector. For a ball to ball contact, the normal vector is directed along the line between two ball centres. For a ball to wall contact, the normal vector is directed along the line defining the shortest distance between the ball centre and the wall.

It is worth mentioning that the normal contact stiffness is a secant modulus which relates total displacement and force while the shear contact stiffness is a tangent modulus which relates the incremental displacement and force. When a contact is formed, the shear force is initialised to be zero. Each subsequent relative shear displacement will cause an incremental shear force to be developed and added to its current value to form a new shear force for next cycle. The incremental shear force is calculated using:

$$\Delta F_i^s = -K^s V_i^s \Delta t \tag{3.3}$$

where K^s is shear contact stiffness, V_i^s is the shear component of contact velocity and Δt is the time step. The new shear force is then calculated by summing the incremental shear force vector with the shear force existing at start of the time step as follows:

$$F_i^s = \left\{F_i^s\right\}^{current} + \Delta F_i^s \tag{3.4}$$

The updated contact force and moment will be used to calculate the acceleration of balls using Newton's 2nd law of motion and then integrated to give velocity and displacement and hence updated position of contacting balls. This will be detailed in the law of motion in the following sub-section.

Law of Motion

The motion of a rigid particle is determined by the resultant force and moment vector acting upon it. The motion is resolved into two vector components, one relates the resultant force to translational motion and the other relates the result moment to rotational motion of the particle. The equation for translational motion is expressed in vector form as:

$$F_i = m\left(\ddot{x}_i - g_i\right) \tag{3.5}$$

where F_i is the sum of all external forces acting on the particle, m is the total mass of the particle, $\ddot{x}_i$ is the acceleration of particle and g_i is the body force acceleration vector (i.e. gravity loading).

The equation for rotational motion is given in the vector form as:

$$M_i = I\dot{\omega}_i = \left(\frac{2}{5}mR^2\right)\dot{\omega}_i \tag{3.6}$$

where M_i is the resultant moment acting on particle, I is the moment of inertia of a particle, $\dot{\omega}_i$ is the angular acceleration of a particle and R is the radius of a spherical particle.

The equations of motion, given by Equation (3.5) and (3.6) are integrated using a centred finite difference procedure involving a time step Δt. The quantities of $\dot{x}_i$ and ω_i are computed at the mid-intervals of $t \pm \Delta t/2$, whilst the quantities $x_i, \ddot{x}_i, \dot{\omega}_i, F_i$ and M_i are computed at the primary intervals of $t \pm \Delta t$. The translational and rotational accelerations at time t are calculated as:

$$\ddot{x}_i^{(t)} = \frac{1}{\Delta t}\left(\dot{x}_i^{(t+\Delta t/2)} - \dot{x}_i^{(t-\Delta t/2)}\right)$$

$$\dot{\omega}_i^{(t)} = \frac{1}{\Delta t}\left(\omega_i^{(t+\Delta t/2)} - \omega_i^{(t-\Delta t/2)}\right) \tag{3.7}$$

The translational and rotational velocities at time $t \pm \Delta t/2$ can be solved by substituting Equation (3.7) into Equations (3.5) and (3.6) as:

$$\dot{x}_i^{(t+\Delta t/2)} = \dot{x}_i^{(t+\Delta t/2)} + \left(\frac{F_i^{(t)}}{m} + g_i\right)\Delta t$$

$$\omega_i^{(t+\Delta t/2)} = \omega_i^{(t-\Delta t/2)} + \left(\frac{M_i^{(t)}}{I}\right)\Delta t \tag{3.8}$$

Therefore, the position of particle centre is updated by integrating velocities in Equation (3.8) giving:

$$x_i^{(t+\Delta t)} = x_i^{(t)} + \dot{x}_i^{(t+\Delta t/2)}\Delta t \tag{3.9}$$

In conclusion, given the values of $\dot{x}_i^{(t-\Delta t/2)}$, $\omega_i^{(t-\Delta t/2)}$, $x_i^{(t)}$, $F_i^{(t)}$ and $M_i^{(t)}$, Equation (3.8) is used to obtain $\dot{x}_i^{(t+\Delta t/2)}$ and $\omega_i^{(t+\Delta t/2)}$. Then, Equation (3.9) is used to obtain $x_i^{(t+\Delta t)}$. The values of $F_i^{(t+\Delta t)}$ and $M_i^{(t+\Delta t)}$, to be used in next cycle, are obtained by the application of the Force-displacement law.

3.3.3 Mechanical timestep

The PFC3D time-stepping algorithm assumes that velocities and accelerations are constant within each timestep. Therefore, the timestep in the PFC3D calculation cycle must be small enough to assure the disturbance can only propagate to its neighbour during a single timestep. The computed calculation produced by Equation (3.8) and (3.9) will remain stable if the timestep does not exceed the critical value. PFC3D has the ability to estimate the critical timestep at the start of each calculation cycle. Then the actual timestep is treated as a fraction of this estimated critical value.

The estimation of the critical timestep is determined firstly by considering a one-dimensional mass spring system described by a point mass (*m*) and spring stiffness (*k*). The critical timestep is given by (Bathe and Wilson, 1976) as:

$$t_{crit} = \frac{T}{\pi}$$

$$T = 2\pi\sqrt{m/k} \tag{3.10}$$

where *T* is the period of the system. Now, consider the infinite series of point mass and springs in Figure 3.9(a), which illustrates the contacts in the system. When the masses are moving synchronized opposing motion, there is no motion at the centre of each spring. The motion in a single point mass is described by two equivalent systems shown in Figure 3.9(b) and 3.9(c). Therefore, the critical timestep in this system is found by using Equation (3.10) to be:

$$t_{crit} = 2\sqrt{m/(4k)} = \sqrt{m/k} \tag{3.11}$$

3.3.4 Servo-control mechanism

The compressive stress (or load) on a numerical sample in PFC3D is applied by moving the wall (or loading platen) with a specify velocity. For simulations that require constant loading throughout the test (e.g. constant stress creep test), the servo-control mechanism is implemented. This servo function is called on every calculation cycle to determine the current wall stresses and then adjusting the wall velocities in such a way to reduce the difference between measured stress and required stress. The calculation algorithm for servo-control mechanism is described as below:

$$\dot{u}^{(w)} = G(\sigma^{measured} - \sigma^{required}) = G\Delta\sigma \tag{3.12}$$

where G is the 'gain' parameter estimated using following reasoning. The maximum increment in wall force arising from wall movement in one timestep is:

$$\Delta F^{(w)} = k_n^{(w)} N_c \dot{u}^{(w)} \Delta t \tag{3.13}$$

where, N_c is the number of contacts on the wall and k_n is the average stiffness of these contacts. Hence the change in mean wall stress is

$$\Delta\sigma^{(w)} = \frac{k_n^{(w)} N_c \dot{u}^{(w)} \Delta t}{A} \tag{3.14}$$

where A is the wall area. For stability reasons, the change in wall stress must be less than the difference between the measured and required wall stress. To fulfil this stability requirement, a relaxation factor α is introduced such that

$$\left|\Delta\alpha^{(w)}\right| < \alpha\left|\Delta\sigma\right| \tag{3.15}$$

Substituting Equations (3.12) and (3.14) into Equation (3.15)

$$\frac{k_n^{(w)} N_c G\left|\Delta\sigma\right|\Delta t}{A} < \alpha\left|\Delta\sigma\right|$$

$$G = \frac{\alpha A}{k_n^{(w)} N_c \Delta t} \tag{3.16}$$

where G is the 'gain' parameter to be substituted in Equation (3.12) for adjusting the wall velocity to achieve the required wall stress in numerical servo-control.

3.4 Constitutive Contact Model

3.4.1 Contact stiffness model

This section describes the elastic contact model for two contacting entities (either ball-wall or ball-ball) subjected to loading in normal and/or shear direction. The contact stiffness relate the contact forces and relative displacement in the normal and shear direction via Equation 3.12 and 3.13. The normal contact stiffness is given in

Equation 3.12 and the shear contact stiffness is given in Equation 3.18. The contact stiffness for the elastic contact model are computed assuming that the stiffness of the two contact entities act in series.

$$K^n = \frac{k_n^{[A]} k_n^{[B]}}{k_n^{[A]} + k_n^{[B]}} \tag{3.17}$$

$$K^s = \frac{k_s^{[A]} k_s^{[B]}}{k_s^{[A]} + k_s^{[B]}} \tag{3.18}$$

where superscript (A) and (B) denote the two entities in contact. The parameters of normal stiffness (k_n) and shear stiffness (k_s) of two contacting entities are specified in PFC3D, and the contact stiffnesses are then computed using Equation 3.12 and 3.13. This contact stiffness is multiplied by the magnitude of the overlap to obtain the contact forces.

3.4.2 Bonding and slip model

This section describes the contact bond adopted in PFC3D to model a bonded material. It has been defined that the particles bonded together with a contact bond cannot slip but they can roll over each other. Figure 3.10 shows the rolling between two balls with a contact bond. It can be seen from this figure that two identical balls (A and B) are joined together by a single contact bond. Ball A has rotated about ball B (fixed) without slipping and bond breakage. The contact bond will remain between ball A and ball B when ball A moves to a new position.

The contact bonds have a specified strength in both normal and shear directions. In the normal direction, contact bonds allow tensile forces to develop at a contact when the overlapping magnitude between a pair of contacting balls is less than zero. The balls are bonded with the normal tensile forces are limited by the normal contact bond strength. If the magnitude of the tensile normal contact force equals or exceeds the normal contact bond strength, the bond breaks and both normal and shear contact forces are set to zero.

In the shear direction, the shear forces of two bonded balls are limited by both the shear contact bond strength and friction between contact balls. If the magnitude of the shear contact force equals or exceeds the shear contact bond strength, the bond breaks but the contact forces are not altered providing the shear force does not exceed the friction limit. A coefficient of friction is set so that the slip model will be activated when the bond breaks; the shear force is resisted if it does not exceed the friction limit.

3.4.3 Burger's viscoelastic model

A Burger's contact model is a user defined contact model implemented in PFC3D to simulate the time dependant behaviour of a material (e.g. asphalt). This contact model is written in the C++ programming language. The Burger's model is represented in Figure 3.11. This model contains a Kevin element and Maxwell element connected in series and can be used in both normal and shear direction together at a contact point. The properties of the Burger's model are listed in Table 3.1.

The total displacement of a Burger's model u (sum of the displacement of the Kelvin element and the Maxwell element) and its first derivative are given by:

$$u = u_k + u_{mk} + u_{mc}$$

$$\dot{u} = \dot{u}_k + \dot{u}_{mk} + \dot{u}_{mc} \tag{3.19}$$

where u_k is the displacement of the viscoelastic component in the Kelvin element, u_{mk} is the displacement of elastic component in the Maxwell element and u_{mc} is the displacement of viscoplastic component in the Maxwell element.

The contact force using stiffness (K_k) and viscosity (C_k) of the Kelvin element is given by:

$$f = K_k u_k + C_k \dot{u}_k \tag{3.20}$$

The contact force using stiffness (K_m) and viscosity (C_m) of the Maxwell element is given by:

$$f = K_m u_{mk} \tag{3.21}$$

$$\dot{f} = K_m \dot{u}_{mk} \tag{3.22}$$

$$f = C_m \dot{u}_{mc} \tag{3.23}$$

From Equation 3.20 the velocity of the Kelvin element is given by:

$$\dot{u}_k = \frac{-K_k u_k + f}{C_k} \tag{3.24}$$

Using a central difference approximation of the finite difference scheme for the time derivative and taking average values for u_k and f gives:

$$\frac{u_k^{t+1} - u_k^t}{\Delta t} = \frac{1}{C_k}\left[-\frac{K_k(u_k^{t+1} + u_k^t)}{2} + \frac{f^{t+1} + f^t}{2}\right] \tag{3.25}$$

Therefore

$$u_k^{t+1} = \frac{1}{A}\left[B u_k^t + \frac{\Delta t}{2C_k}\left(f^{t+1} + f^t\right)\right] \tag{3.26}$$

Where:

$$A = 1 + \frac{K_k \Delta t}{2C_k}$$

$$B = 1 - \frac{K_k \Delta t}{2C_k} \tag{3.27}$$

For the Maxwell element, the displacement and first derivative are given by:

$$u_m = u_{mk} + u_{mc}$$

$$\dot{u}_m = \dot{u}_{mk} + \dot{u}_{mc} \tag{3.28}$$

Substituting Equations (3.22) and (3.23) into Equation (3.28) gives,

$$\dot{u}_m = \frac{\dot{f}}{K_m} + \frac{f}{C_m} \tag{3.29}$$

Using central difference approximation of the finite difference scheme and taking the average value for f,

$$\frac{u_m^{t+1} - u_m^t}{\Delta t} = \frac{f^{t+1} - f^t}{K_m \Delta t} + \frac{f^{t+1} + f^t}{2C_m} \tag{3.30}$$

therefore:

$$u_m^{t+1} = \frac{f^{t+1} - f^t}{K_m} + \frac{\Delta t (f^{t+1} + f^t)}{2C_m} + u_m^t \tag{3.31}$$

The total displacement and first derivative of the Burger's model are given by:

$$u = u_k + u_m$$

$$\dot{u} = \dot{u}_k + \dot{u}_m \tag{3.32}$$

Using finite difference scheme for time derivative gives:

$$u^{t+1} - u^t = u_k^{t+1} - u_k^t + u_m^{t+1} - u_m^t \tag{3.33}$$

Substituting Equations (3.26) and (3.31) into (3.33), the contact force, f^{t+1}, is given by

$$f^{t+1} = \frac{1}{C}\left[u^{t+1} - u^t + \left(1 - \frac{B}{A}\right) u_k^t - Df^t \right] \tag{3.34}$$

where

$$C = \frac{\Delta t}{2C_k A} + \frac{1}{K_m} + \frac{\Delta t}{2C_m}$$

$$D = \frac{\Delta t}{2C_k A} - \frac{1}{K_m} + \frac{\Delta t}{2C_m} \tag{3.35}$$

In conclusion, the contact force f^{t+1} can be calculated from known values for u^{t+1}, u^t, u^t_k and f^t. Verification of the Burger's contact model in PFC3D was performed by ITASCA (2003) and also by Kim *et al.* (2007).

3.5 Summary

The traditional approach to model mechanical behaviour of asphalt is insufficient due to the poor understanding of micromechanics of heterogeneous material. Recent developments in both theory and computer technology have allowed the further investigation of asphalt behaviour in a microscopic scheme using DEM. DEM has been widely adopted in soil and rock mechanics whilst many programming codes have been developed since the 1970's. PFC3D has been applied in a wide range of applications by many researchers (Section 3.2).

PFC3D and its calculation algorithms were described in Section 3.3. The calculation cycle in PFC3D is a time-stepping algorithm involving the repeated application of the force-displacement law and the law of motion. The mechanical time step and servo-control mechanism was described afterwards. A contact bond has been introduced in modelling the bonded material. The Burger's model is implemented to simulate the time dependant behaviour of asphalt. In conclusion, PFC3D has been approved to be a very powerful DEM programming code available to model asphalt materials.

3.6 Tables

Properties	**Notation**
Normal stiffness for Kelvin element	K_{kn}
Normal viscosity for Kelvin element	C_{kn}
Normal stiffness for Maxwell element	K_{mn}
Normal viscosity for Maxwell element	C_{mn}
Shear stiffness for Kelvin element	K_{ks}
Shear viscosity for Kelvin element	C_{ks}
Shear stiffness for Maxwell element	K_{ms}
Shear viscosity for Maxwell element	C_{ms}
Friction coefficient	f_s

Table 3.1: Properties in a Burger's Model.

3.7 Figures

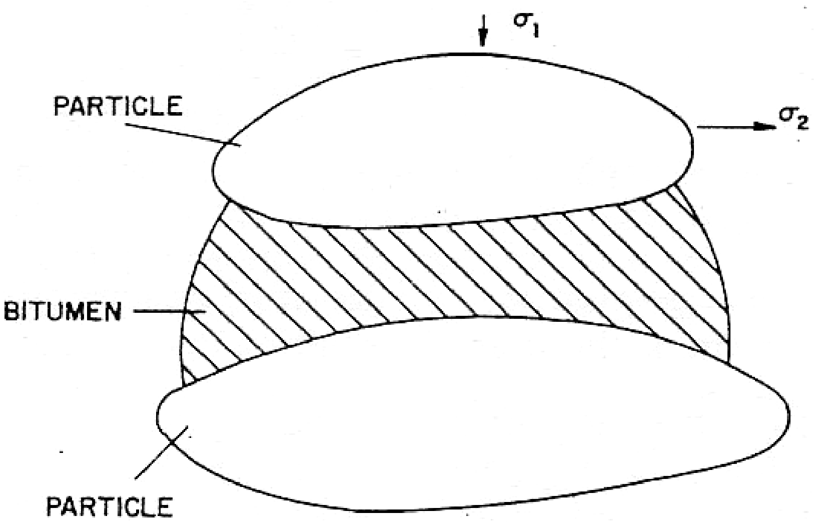

Figure 3.1: Illustration of thin film between two particles (Hill, 1973).

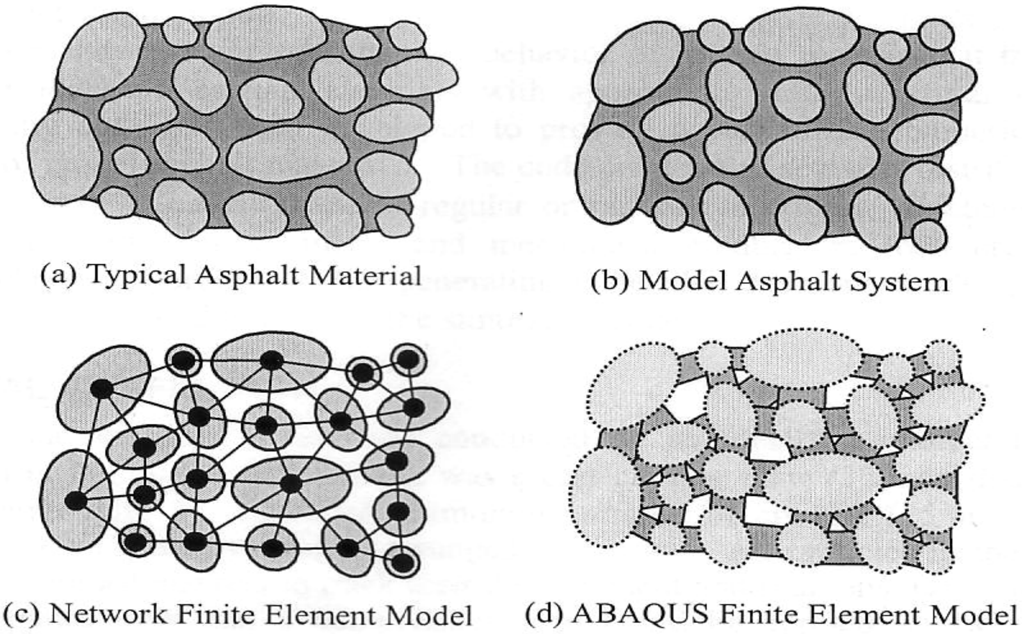

Figure 3.2: Illustration of asphalt modelling concept (Saad *et al*., 2002).

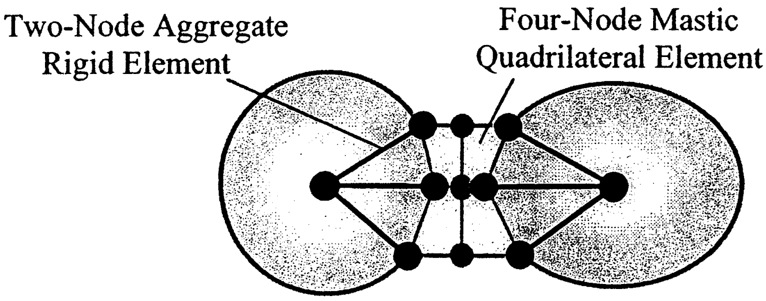

Figure 3.3: ABAQUS modelling scheme for a typical particle pair (Saad *et al*., 2002).

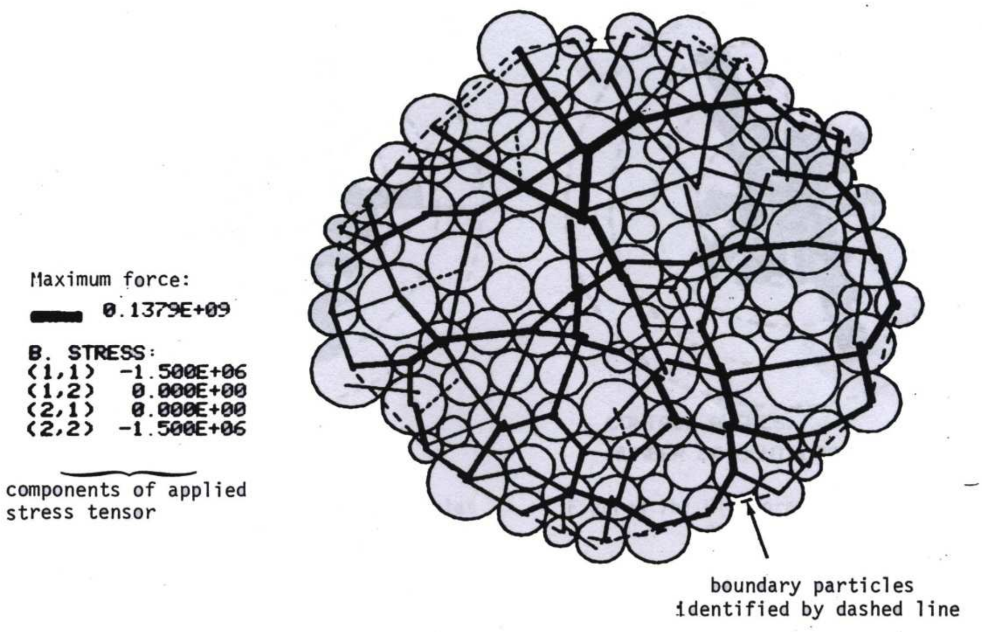

Figure 3.4: Initial state of 100-disc test (McDowell, 2002).

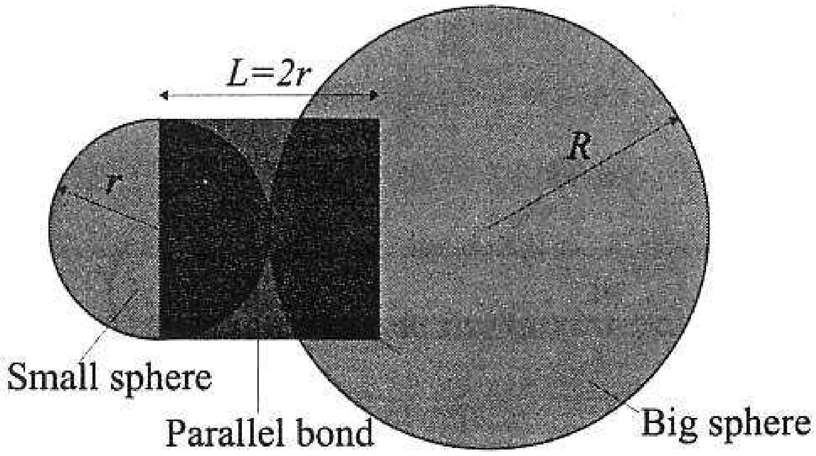

Figure 3.5: Schematic illustration of a bonded particle (Powrie *et al.*, 2005).

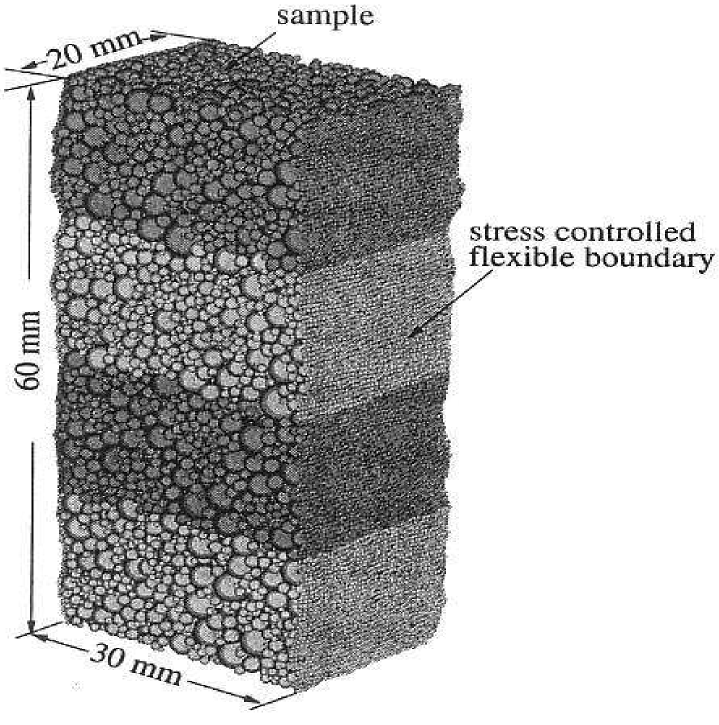

Figure 3.6: Typical sample with 10,000 particles (Powrie *et al.*, 2005).

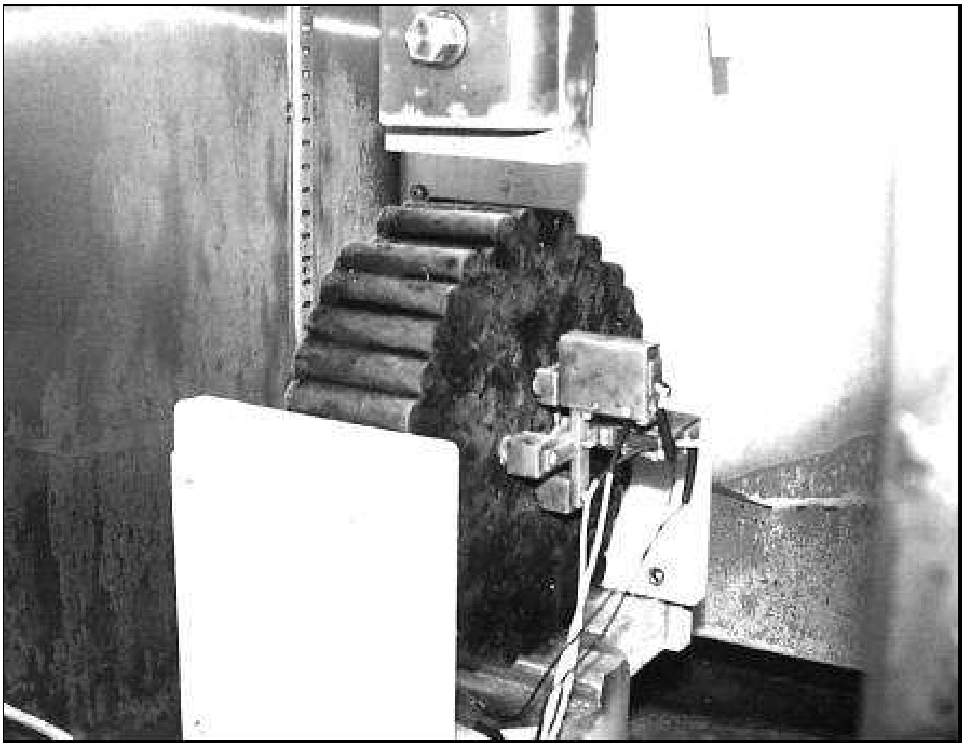

Figure 3.7: Testing of synthetic specimen using IDT (Buttlar and You, 2001).

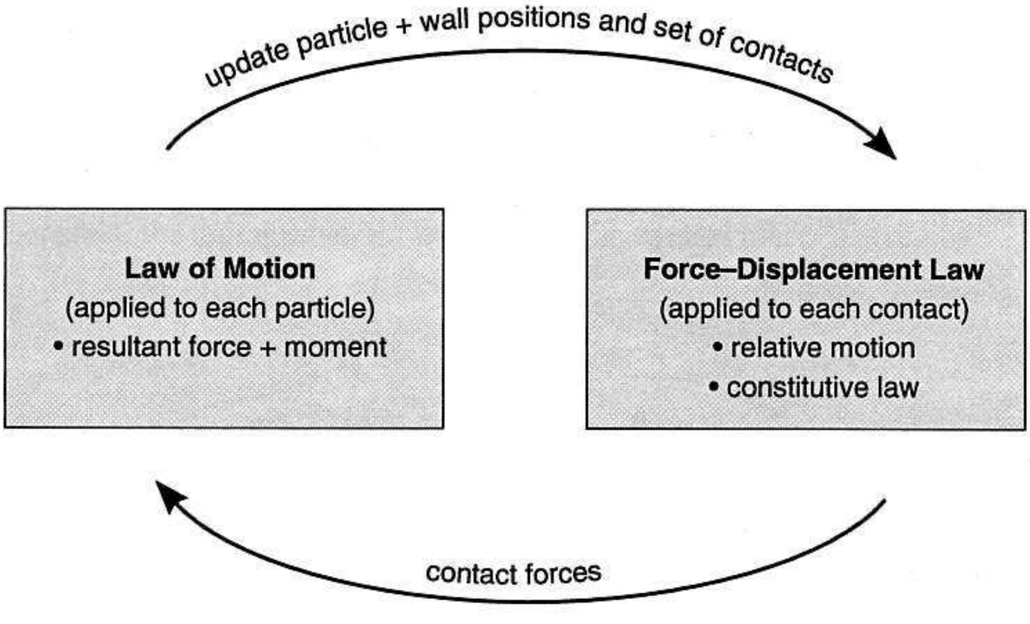

Figure 3.8: Calculation cycle in PFC3D (ITASCA, 2003).

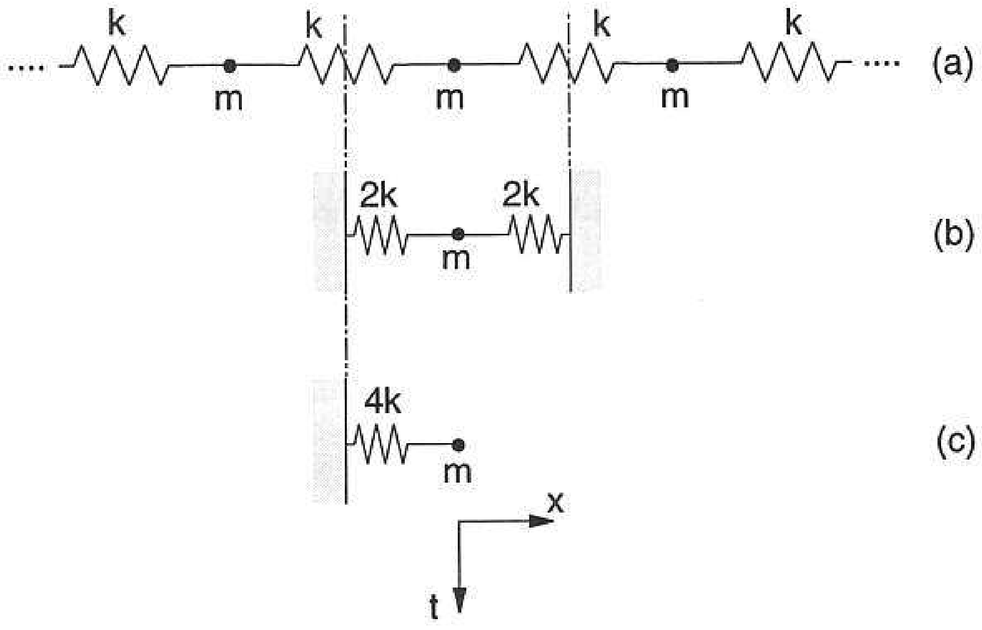

Figure 3.9: Multiple mass spring system (ITASCA, 2003).

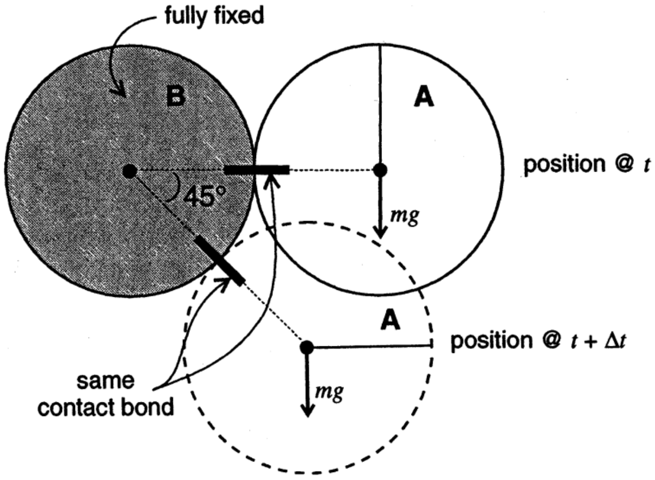

Figure 3.10: Rolling at a contact bond (ITASCA, 2003).

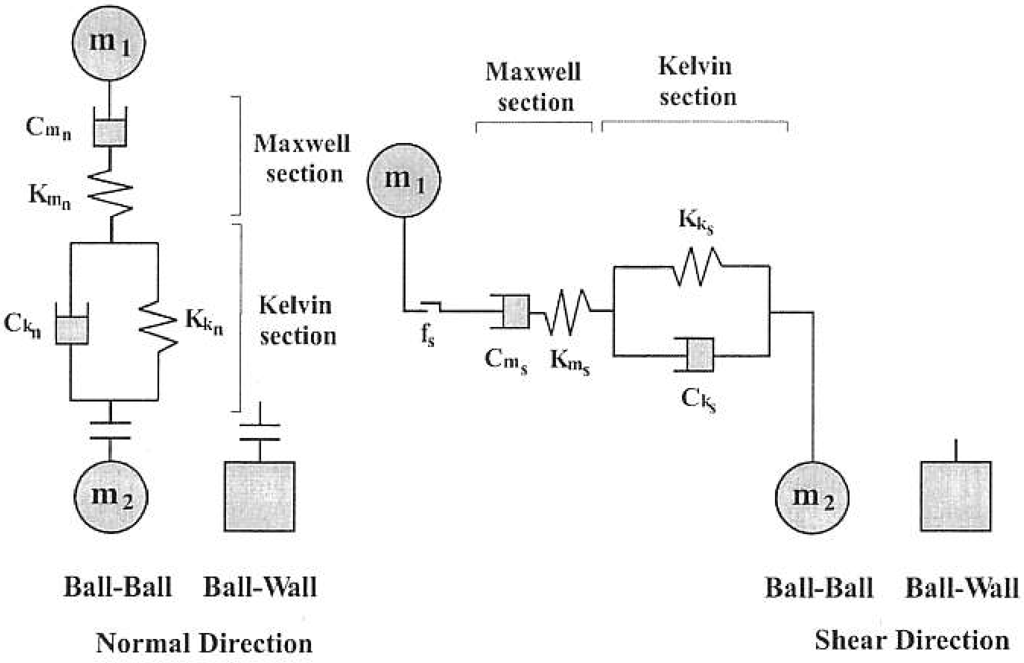

Figure 3.11: Burger's contact model in PFC3D (ITASCA, 2003).

4 EXPERIMENTAL WORK

4.1 Introduction

In general, asphaltic materials are considered as complex multiphase composites comprising bitumen, graded aggregate and air voids. The mechanism of damage in an asphalt mixture is a complicated process and is still not well understood. The microstructure of an asphalt mixture depends on the manufacturing process (particularly compaction) and can be idealised as rigid particles embedded in a matrix of voided bitumen (Fordyce 1996). The two main load carrying mechanism are either through aggregate contact (which depends on inter-particle friction and particle interlock) or through the "stiffness" of the bitumen matrix (Khanzada, 2000). The previous review (Chapter 2) has concluded that the mechanical behaviour of asphalt mixtures can be significantly influenced by the mechanical properties of the bitumen.

This chapter contains details of uniaxial compression tests performed on an idealised asphalt mixture over a range of strain rates and temperatures. The idealised asphalt mixture comprises approximately single-sized sand mixed with bitumen. As a first step to develop a micromechanical model to simulate the behaviour of asphalt mixtures, the behaviour of idealised asphalt mixtures are investigated. The selection and preparation of this type of idealised asphalt mixture are presented in Section 4.2. A series of monotonic tests were performed to failure on this mixture under uniaxial compressive loadings (as described in Section 4.3) and stress-strain responses were measured carefully and are presented in Section 4.4.

4.2 Idealised Asphalt Mixtures

4.2.1 Material selection

A type of idealised asphalt mixture comprising approximately single-sized sand mixed with bitumen was used in this experimental work. This type of material was chosen is because its packing characteristics are well understood (dense random packing) and because the behaviour of this mixture is dominated by the bitumen phase, whilst the complex aggregate interlock effects are minimised (Collop *et al.*, 2004). The idealised asphalt mixture was designed to have the following volumetric proportions; 70% sand, 20% bitumen and 10% air voids. A 40/60 penetration grade bitumen was used with a softing point of 53.5°C. The sand was relatively single-sized, with a particle size distribution varying between 1.18mm to 2.36mm in diameter.

4.2.2 Specimen preparation

Deshpande and Cebon (2000) investigated the influence of various compaction procedures in the laboratory and concluded that either single plunger compression in multiple layers or double plunger compression in single layers gave satisfactory homogeneous test specimens. Consequently, a cylindrical split mould (shown in Figure 4.1), 75mm in diameter and 150mm in height, was manufactured and used to cast the specimen and a vibrating Kango hammer compactor was used for specimen compaction. The diameter of the cylindrical mould was chosen so that it was at least 10 times greater than the size of largest particles. The ratio of the height to the diameter of the compacted specimens was chosen to be approximately one. A lubricant consisting of a mixture of natural soap and glycerine was applied to the inner surfaces of the mould to prevent sticking of the asphalt mixture. However, the end plate of vibrating Kango hammer could not be lubricated because traces of lubricant would be left on each compacted layer of the specimen. Consequently, a wooden disc was fixed to the underside of the hammer head and this was lubricated by silicone to prevent sticking of the mixtures during compaction.

The specimen was compacted to an initial height of approximately 100mm and then trimmed to give a final height of 75mm. The specimens were compacted from only one side in three layers and care was taken to insure that the top surface of each specimen was flat and smooth. Following compaction, the specimens were allowed to cool to room temperature for at least 12 hours. The moulds were then carefully dismantled to avoid any surface damage and the geometry and density of the specimens were measured before being trimmed. After that the specimens were stored in a cold room at 5°C. Figure 4.2 shows a typical specimen of idealised asphalt mixture after preparation.

The influence of friction between the specimen and loading platens on compression test results is a well documented problem. It is known that, by inducing a large lateral force, the loading platens confine the ends of specimen, which may lead to the overestimation of the compressive strength and cause the well known barrel-shaped specimen failure. Many researchers have shown that combinations of different types of plastic sheet and lubricant may reduce or eliminate the friction at the interface between the test specimens and the loading platens (Erkens, 2002; Dunhill, 2002; Taherkhani, 2006). As a friction reduction system, Erkens (2002) and Dunhill (2002) used a plastic film of Luflexen coated with a thin layer of a soft soap on both sides. Luflexen was selected for its low yield strength, high ultimate strain and high resistance to rupture. Taherkhani (2006) reported that a polyethylene foil named EXCEED was used in his research which has shown a similar friction reduction characteristic to Luflexen. Therefore, a similar friction reduction system to Dunhill (2002) was employed in this research to minimize the confining effects of the loading platens. This comprised a plastic film, 50 μm in thickness ('Luflexen') which was coated with a liquid soap ('Zalpon') supplied by Diverseylevler Ltd. Figure 4.3 shows the deformations of two specimens after the same monotonic test; one tested using the friction reduction system (Figure 4.3a) whilst another without any friction reduction system (Figure 4.3b). It can be seen in the figure that the specimen tested with friction reduction system is almost uniform deformed throughout the specimen whilst the one without the friction reduction system has shown a typical barrel-shaped failure.

4.3 Monotonic Uniaxial Compression Tests

4.3.1 Testing equipment

A hydraulic testing machine was used for conducting the uniaxial compression tests, as shown in Figure 4.4. The equipment consists of a temperature-controlled cabinet, with a 0°C to 50°C operating range, mounted on an INSTRON loading frame, a 100 kN servo-hydraulic actuator with displacement range of ± 50 mm. The loading frame was controlled by a 'Rubicon' digital servo-control system. An external pump supplied the hydraulic power for the equipment and a desktop computer was used for data acquisition.

For constant strain rate testing, a monotonically increasing displacement was applied to each test specimen through the actuator. A Linear Variable Differential Transformer (LVDT), connected to an actuator piston, monitored the movement/stroke of the crosshead and provided the feedback signal for the control system. The control system compared this signal with the input command and the difference was returned to the servo-valve, which reduced the difference by adjusting the oil flow.

4.3.2 Testing protocol

Asphalt is a well-known viscoelastic material whose properties are both temperature and loading rate dependent. It exhibits glassy elastic behaviour when the temperature is low and/or the loading time is short and viscous behaviour when the temperature is high and/or the loading time is long. In the intermediate range of test conditions, asphalt behaves viscoelastically. Consequently, a series of monotonic uniaxial compression tests were designed to test the idealised asphalt mixture over a range of strain rates and temperatures. Firstly, in order to investigate the brittle behaviour of the idealised asphalt mixture, a set of tests was performed under a constant strain rate of 0.1s^{-1} and a test temperature of -20°C. These conditions were chosen to minimise viscoelastic effects so that the response was primarily in the elastic region of behaviour.

In order to investigate the time and temperature dependent viscoelastic properties of the idealised asphalt mixtures, three additional sets of tests were performed. The first set of tests was performed at a temperature of 20°C and three different strain rates (0.02s^{-1}, 0.1s^{-1}and 0.5s^{-1}) to introduce more ductility (viscoelasticity) into the behaviour. The strain rate dependency was also investigated in this set of tests. The second set of tests was the same as the first set except that tests were performed at a temperature of 10°C. The third set of tests was performed at a constant strain rate of 0.02s^{-1} over a range of temperatures (0, 10 and 20°C) so that temperature-compensated strain rate effect can be investigated by comparing with the other two sets of tests. The details of testing conditions have been summarised in Table 4.1.

4.4 Experimental Results and Analysis

4.4.1 Brittle response

As indicated in the previous section, for the initial set of tests, the testing conditions were chosen at a temperature of -20°C and a constant strain rate of 0.1s^{-1} so that viscoelastic effects can be minimised whilst its primary response was dominated by elastic region of behaviour. For a constant strain rate test, a constant axial displacement rate (velocity) was applied to the specimen until a preset termination axial strain level was reached. It should be noted that nominal stress was calculated rather than the true stress which takes into account the change of cross sectional area of the specimen during the test.

In total, three repeated tests were undertaken and the results are shown in Figure 4.5 where axial nominal stress is plotted against axial strain. It can be seen from this figure that the curves can be divided into three regions. In the early stages of the test, the stress increases approximately in proportion to the strain (i.e. linear behaviour). There is then a small region of hardening where the slope of the stress-strain curve decreases as the peak stress (compressive strength) is approached. Beyond the peak, the material then softens and the stress decreases rapidly as failure occurs. It can also be seen from Figure 4.5 that repeatability is quite good between the three individual test results.

4.4.2 Ductile response

The first set of tests was performed at a temperature of 20°C at three different strain rates, ($0.02s^{-1}$, $0.1s^{-1}$and $0.5s^{-1}$). A typical result is shown in Figure 4.6 where axial stress is plotted against axial strain for different strain rates. It can be seen that the general shape of the stress-strain curves are similar to those shown in Figure 4.5 although, as expected, the peak stress is reached at a higher strain and there is a significantly greater amount of post-peak response indicating greater ductility. It can also be seen that the peak stress (compressive strength) increases as the strain rate increases and the strain level where peak stress occurs is approximately independent of strain rate. Figure 4.6 also shows that the stiffness values increase as strain rate increases.

The second set of tests was performed at a temperature of 10°C and at three different strain rates ($0.02s^{-1}$, $0.1s^{-1}$ and $0.5s^{-1}$). A typical result is shown in Figure 4.7 where axial stress is plotted against axial strain for different strain rates. It can be seen that the general shape of curves are similar to those shown in Figure 4.6 although, as expected, the peak stress for each strain rate is slightly higher than the corresponding test result at 20°C. The axial strain where peak stress occurs did not show much dependence on strain rates. It can also be seen in Figure 4.7 that the axial stress when testing at $0.5s^{-1}$ drops faster in the softening region than its counterpart at 20°C which indicates some transient behaviour from ductile to brittle has occurred.

The third set of tests was performed at a strain rate of $0.02s^{-1}$ over three temperatures (0, 10 and 20°C) to investigate the effect of temperature variations on the mixture. Figure 4.8 shows typical results from this test set, where the axial stress is plotted against axial strain for three temperatures. It can be seen in this figure that the general shape of curve at each test temperature is similar and that the peak stress values increase as the temperature decreases.

Figure 4.9 summaries the peak stresses plotted as a function of strain rates on double logarithmic scales for these three sets of tests. It can be seen in this figure that a general trend has been observed for peak stress to increase as either strain rate increases or as temperature decreases. It can also be seen in this figure that peak stress is approximately proportional to strain rate when plotted on double logarithmic scales with a gradient of approximately 0.29 for tests performed at 20°C (triangle symbol). A similar gradient has also been observed from this figure for the tests performed at 10°C (square symbol).

As Figure 4.9 shows, at a certain temperature a plot of the peak stress against strain rate on double logarithmic scales is linear. The power law relation summarising the results is as follows:

$$\left(\frac{\sigma_p}{\sigma_0}\right)=\left(\frac{\dot{\varepsilon}}{\dot{\varepsilon}_0}\right)^n \tag{4.1}$$

Where σ_0, the reference stress is 10.3 *MPa*, $\dot{\varepsilon}_0$, the reference strain rate is 0.1s^{-1} for 10°C. The power law exponent n = 0.29 and is approximately independent of temperature. Assuming Arrhenius-type temperature dependence, the experimental data can be fitted to a similar equation to Equation 2.21 as follows,

$$\left(\frac{\sigma_p}{\sigma_0}\right)=\left(\frac{\dot{\varepsilon}}{\dot{\varepsilon}_0}\right)^n\left(\exp\left(\frac{k}{T}\right)\right)^n \tag{4.2}$$

Data from tests at three temperatures (0, 10 and 20°C) gave an Arrhenius constant k of 13.4×10^3 K. The previous literature has indicated that strain rate applied at various temperatures (T_1) can be converted to equivalent strain rate at a reference temperature T_0, using an Arrhenius model for $T \leq 20°\text{C}$ (see section 2.5.3). This temperature correction to the strain rate is valid only in the diffusion-controlled region shown on the deformation mechanism map of Cheung and Cebon (1997), Figure 2.9. In this study, a shift factor based on the Arrhenius model is used for all tests performed over the temperature range 0°C to 20°C. The equivalent temperature-compensated strain rate is given by:

$$\dot{\varepsilon}^T=\dot{\varepsilon}\left(\exp\left(k\left(\frac{1}{T_1}-\frac{1}{T_0}\right)\right)\right) \tag{4.3}$$

Where, the Arrhenius constant k is the same value as in Equation 4.2. A reference temperature T_0 of 283 K (10°C) was chosen for a generalised form. Note that in this investigation, a reference temperature of 283 K (10°C) was adopted rather than the glass transient temperature T_g. This is because T_g of sand asphalt mixtures lies outside the range of temperatures tested here and that the applicability of the model at rather low temperature is unclear. This form can be used to convert the strain rate ($\dot{\varepsilon}$) that applies at an arbitrary temperature (T_1) varying 0 to 20°C to a temperature-compensated strain rate ($\dot{\varepsilon}_T$) at the reference temperature (T_0) of 10°C. For example, for the sand asphalt tested at the strain rate of 0.02s^{-1} at 20°C, the temperature-compensated strain rate is approximately 0.004s^{-1} at the reference temperature of 10°C providing the peak stress is constant. The summary of conversions between strain rates and temperature-compensated strain rates has been given in Table 4.2.

Figure 4.10 shows a plot of peak stress versus temperature-compensated strain rate which was shifted to the reference temperature of 10°C by using the Equation 4.3. Consequently, a mater curve can be further generalised by normalising each peak stress by the stress at 0.1s^{-1} at 10°C. Figure 4.11 shows the normalised peak stress plotted against the temperature-compensated strain rate over three temperatures (0, 10 and 20°C). It can be seen in this figure that the normalised peak stress is approximately proportional to the temperature-compensated strain rate on a double logarithmic scale with a gradient of approximately 0.29. The data shown in Figure 4.11 can be fitted to the following equation:

$$\left(\frac{\sigma_{T,\dot{\varepsilon}}}{\sigma_0}\right)=\left(\frac{\dot{\varepsilon}_T}{\dot{\varepsilon}_0}\right)^n\left(\exp\left(k\left(\frac{1}{T}-\frac{1}{T_0}\right)\right)\right)^n \tag{4.4}$$

Where σ_0, the reference stress is 1 MPa, $\dot{\varepsilon}_0$, the reference strain rate is 0.1s^{-1} at the reference temperature of 10°C and Arrhenius constant k is the same as in Equation 4.2.

Figure 4.12 shows the initial stiffness plotted as a function of strain rates on a double logarithmic scale for tests performed at 0, 10 and 20°C. It can be seen in this figure that the initial stiffness is approximately proportional to strain rate on double logarithmic scales with a gradient of approximately 0.29 for the sand asphalt at 20°C (diamond symbol). A similar gradient can also be observed from this figure for the sand asphalt tested at 10°C (cross symbol).

Figure 4.13 shows the normalised initial stiffness (normalised by the stiffness at 0.1s^{-1} and 10°C) plotted against the temperature-compensated strain rate which was also shifted to the reference temperature of 10°C by using the Equation 4.3. It can be seen in this figure that a linear relationship between the normalised stiffness and temperature-compensated strain rate can be observed in a double-logarithmic scale with a gradient of approximately 0.29 for the tests at three temperatures. The data as shown in Figure 4.13 can also be fitted to an equation similar to Equation 4.4 as follows,

$$\left(\frac{K_{T,\dot{\varepsilon}}}{K_0}\right)=\left(\frac{\dot{\varepsilon}_T}{\dot{\varepsilon}_0}\right)^n\left(\exp\left(k\left(\frac{1}{T}-\frac{1}{T_0}\right)\right)\right)^n \tag{4.5}$$

Where K_0, the reference stiffness is 1 $MPa, \dot{\varepsilon}_0$, the reference strain rate is 0.1s^{-1} at the reference temperature of 10°C and Arrhenius constant k is the same as in Equation 4.2.

It should be noted that the same gradient observed for normalised peak stress and initial stiffness with respect to the temperature-compensated strain rate will be used in this thesis to scale the contact bond strength and stiffness in further DEM simulations (as described in subsection 7.7.3).

4.5 Summary and Conclusions

The following conclusions can be drawn from this chapter:

- A highly idealised asphalt mixture comprising approximately single-sized sand mixed with bitumen was selected as the testing material for its well known volumetric properties and in order to simplify the tests.

- The procedure to prepare the idealised asphalt mixture specimens has been described and a lubrication system has been introduced to reduce the end-confinement of specimens during testing.

- A series of tests have been performed on the idealised asphalt mixture under monotonic compressive loading over a range of strain rates and temperatures. The axial stress-strain response under each testing condition was measured carefully.

- A set of tests was performed under low temperature (-20°C) and fast strain rate conditions ($0.1s^{-1}$) so that the primary response of the mixture is dominated by the elastic region of behaviour. The general shape of the stress-strain response has been divided into three well defined regions: elastic region, hardening region and post-peak softening region. Three individual tests were performed under the same testing condition and repeatability is quite good between the three individual test results.

- A series of tests were performed over a range of temperatures (10°C and 20°C) and strain rates ($0.02s^{-1}$, $0.1s^{-1}$ and $0.5s^{-1}$) to investigate ductile behaviour of the idealised asphalt mixture. For each temperature condition, the general stress-strain response has shown a power-law increase of peak stress as strain rate increases with an exponent of 0.29 which is temperature independent.

- Additional tests were performed at $0.02s^{-1}$ over three temperatures (0, 10 and 20°C) to investigate the temperature dependence of the ductile behaviour of the mixture. A constitutive relationship has been generalised between the peak stresses and the temperatures.

- It has been found that for all testing strain rates applied at various temperatures can be converted to the temperature-compensated strain rates at a reference temperature of 10°C by using an Arrhenius model. A linear relationship can be found between normalised peak stresses and temperature-compensated strain rates in a double logarithmic scale with a gradient of approximately 0.29.

- It has been found that the normalised initial stiffness is approximately proportional to the temperature-compensated strain rates in a double logarithmic scale with a gradient of approximately 0.29.

4.6 Tables

Temperature (°C)	**Strain rate (s^{-1})**		
-20	--	0.1	--
0	0.02	--	--
10	0.02	0.1	0.5
20	0.02	0.1	0.5

Table 4.1: Summary of testing conditions.

	0°C			**10°C (reference)**			**20°C**		
$\dot{\varepsilon}$ (s^{-1})	0.02	0.1	0.5	0.02	0.1	0.5	0.02	0.1	0.5
$\dot{\varepsilon}_T$ (s^{-1})	0.1	--	--	0.02	0.1	0.5	0.004	0.02	0.1

Table 4.2: Summary of temperature compensations of strain rates.

4.7 Figures

Figure 4.1: Photograph showing split mould.

Figure 4.2: Photograph showing a typical specimen of idealised asphalt mixture.

(a)

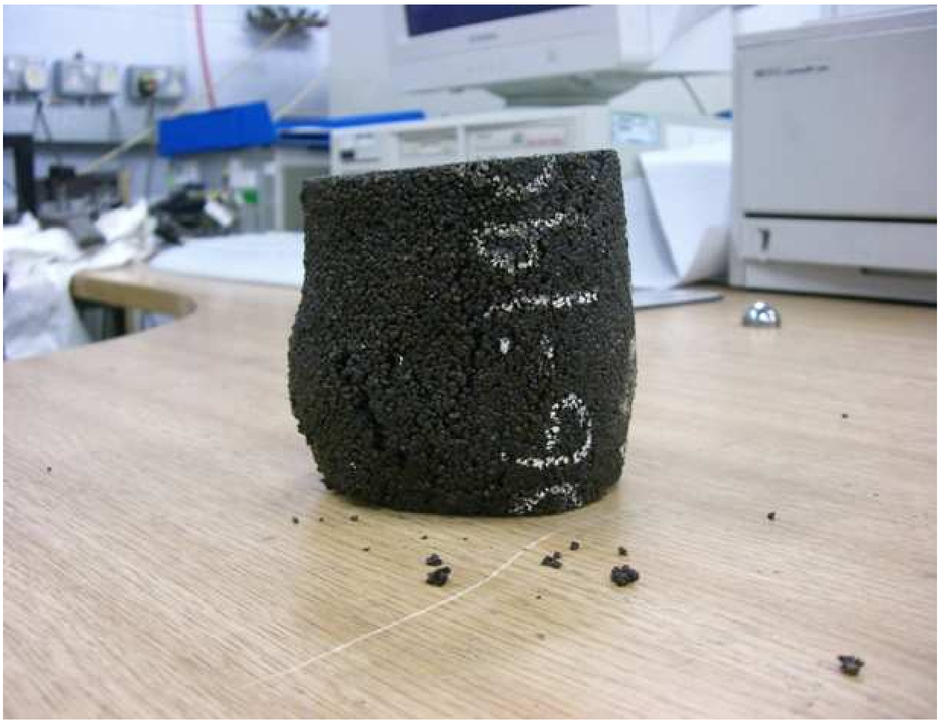

(b)

Figure 4.3: Photograph showing specimens tested with friction reduction system (a) and without friction reduction system (b).

Figure 4.4: Photograph showing experimental apparatus.

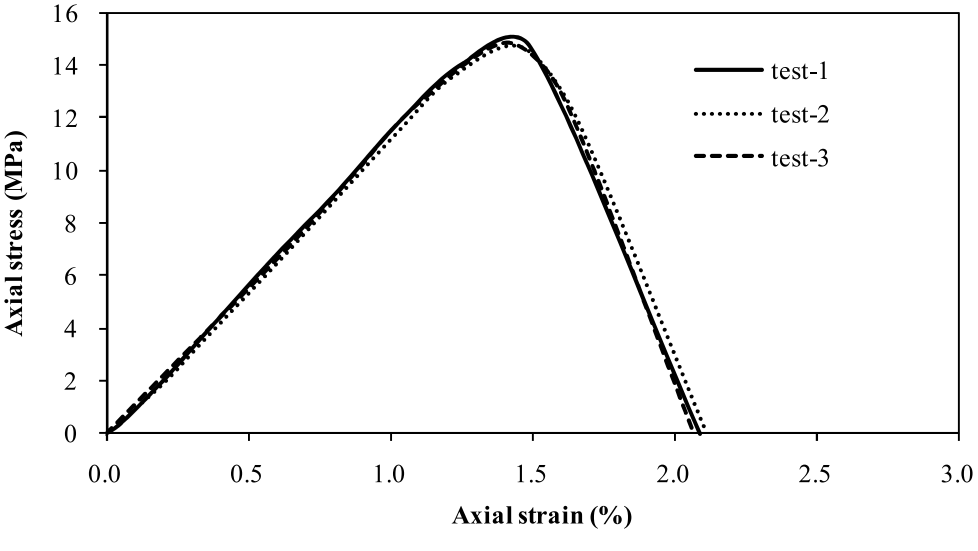

Figure 4.5: Stress-strain response of experiments performed in the brittle elastic regime of behaviour.

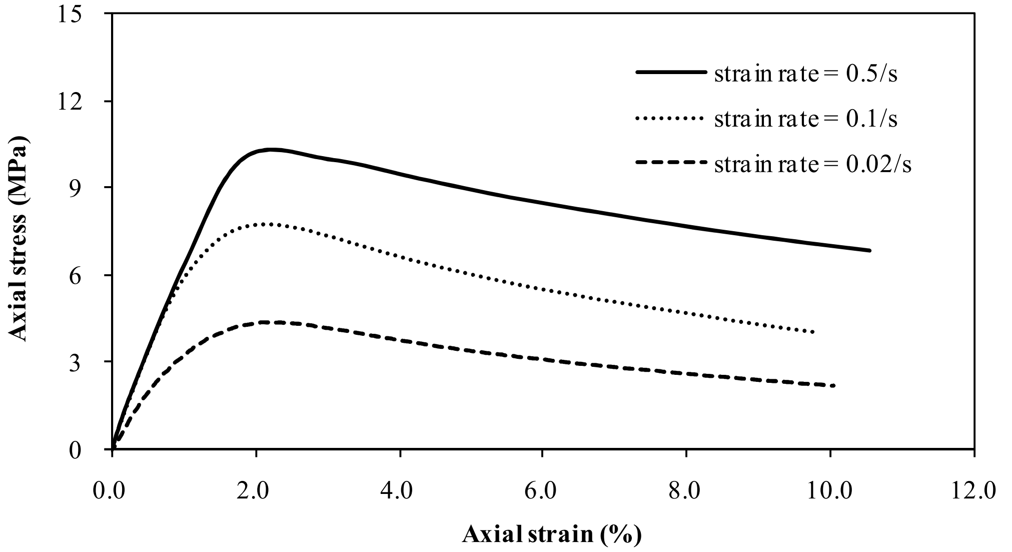

Figure 4.6: Stress-strain response of experiments performed at 20°C.

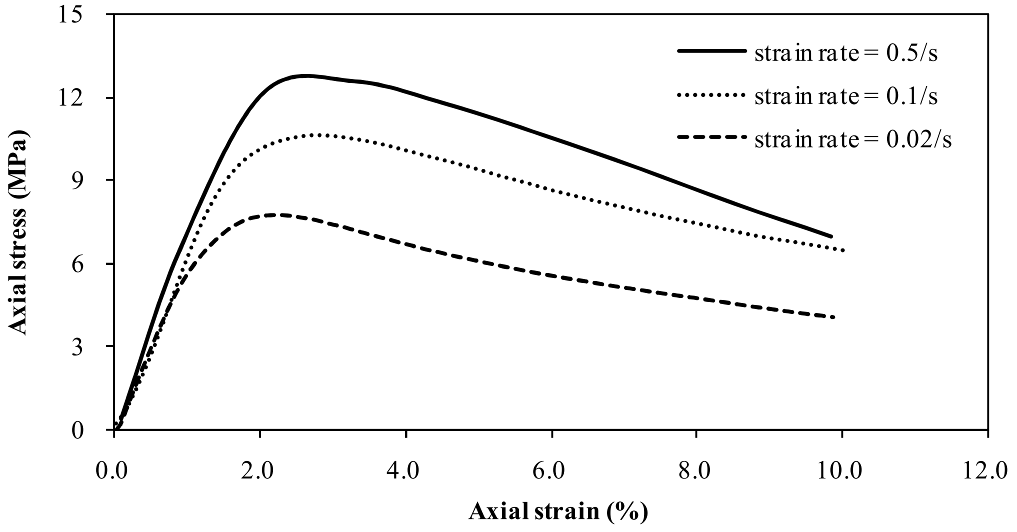

Figure 4.7: Stress-strain response of experiments performed at 10°C.

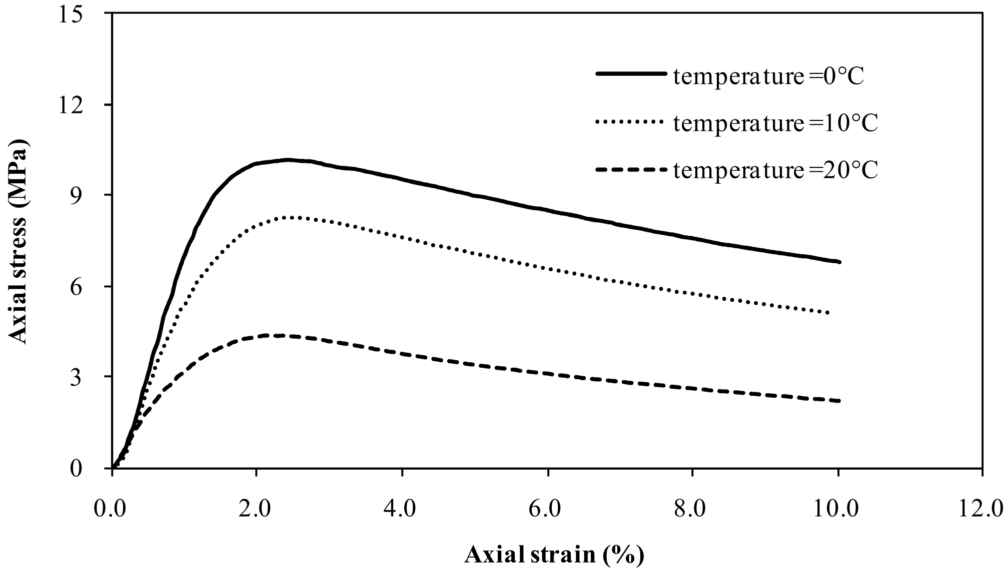

Figure 4.8: Stress-strain response of experiments performed at strain rate of $0.02 s^{-1}$.

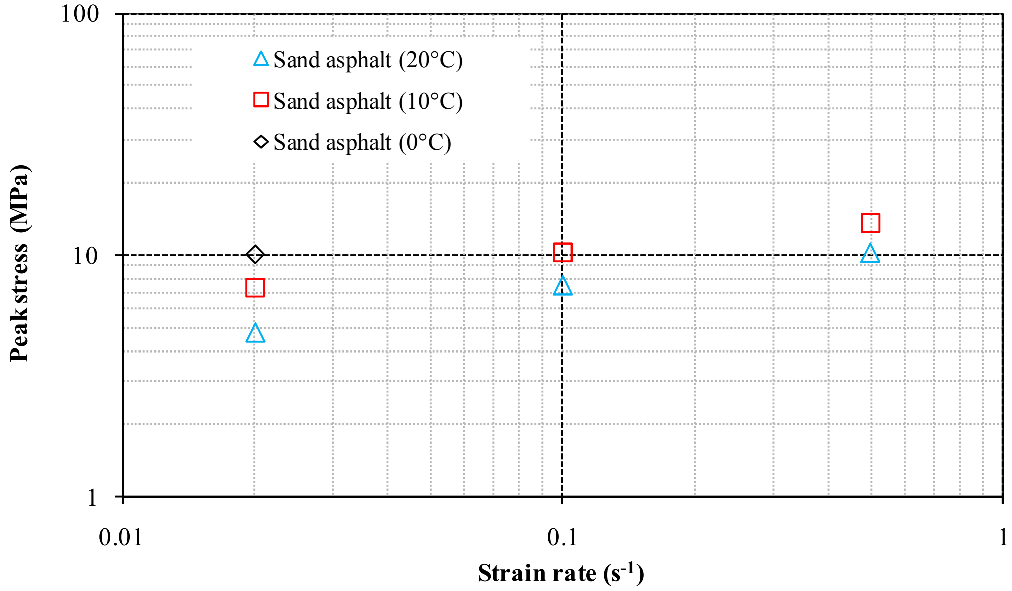

Figure 4.9: Peak stress (compressive strength) plotted against strain rate in a double logarithmic scale for sand asphalt tested at 0, 10 and 20°C.

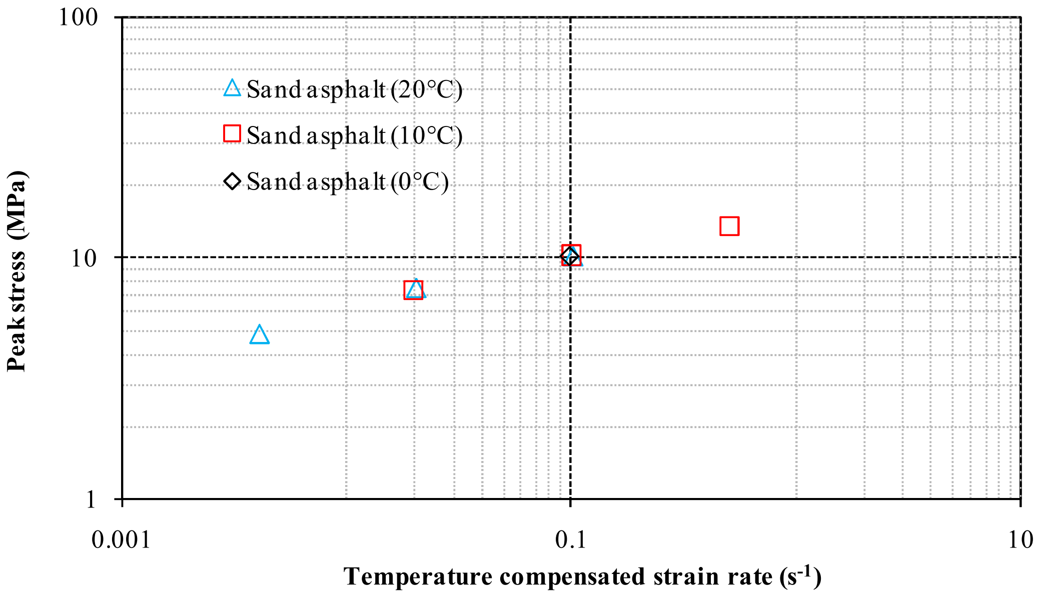

Figure 4.10: Peak stress plotted against temperature-compensated strain rate in a double logarithmic scale for sand asphalt tested at 0, 10 and 20°C.

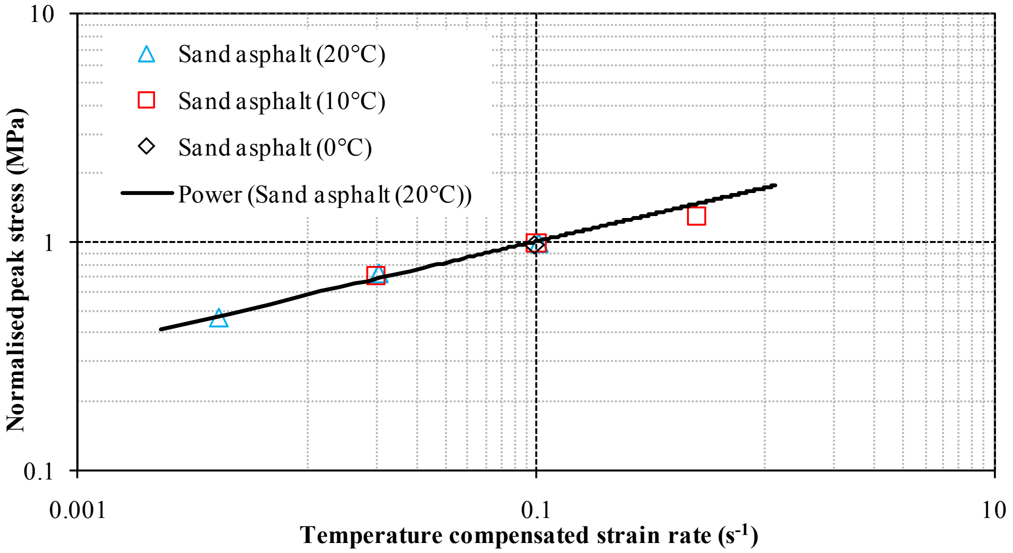

Figure 4.11: Normalised peak stress plotted against temperature-compensated strain rate in a double logarithmic scale for sand asphalt tested at 0, 10 and 20°C.

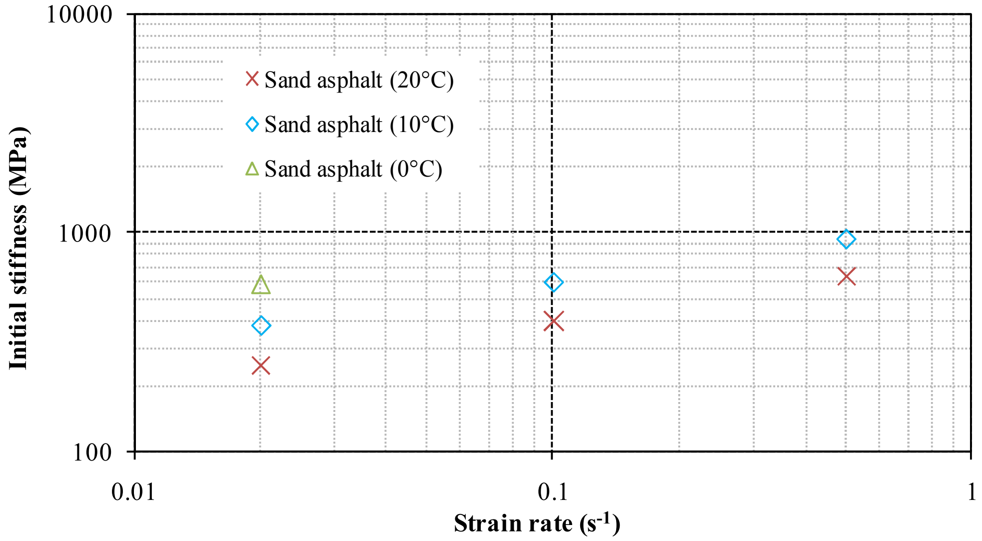

Figure 4.12: Initial stiffness plotted against strain rate in a logarithmic scale for sand asphalt tested at 0, 10 and 20°C.

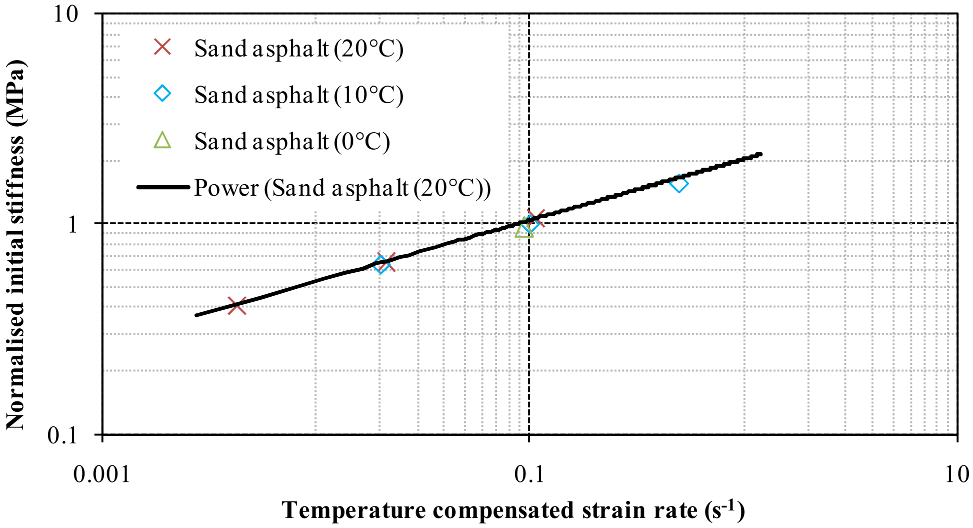

Figure 4.13: Normalised stiffness plotted against temperature-compensated strain rate in a double logarithmic scale for sand asphalt tested at 0, 10 and 20°C.

5 NUMERICAL SAMPLE PREPARATION PROCEDURE

5.1 Introduction

It was noted in Chapter 4 that sand asphalt has been selected in this project is because its packing characteristics are known (dense random packing) and the behaviour of the mixture is dominated by the bitumen phase whilst complex aggregate interlock effect will be minimized. Since the objective of this project is to model simple laboratory tests (uniaxial compression tests) using the DEM approach, it was necessary to generate an artificial numerical sample to replicate the idealised asphalt mixture. It was important to ensure that the sample was initially isotropic and densely packed (i.e. similar to a laboratory prepared sand asphalt specimen). Therefore, a numerical sample preparation procedure has been developed to prepare cylindrical samples comprising single-sized particles of known radius (i.e. sand size).

This chapter starts by reviewing the packing characteristics of spheres. The details of generating an initially isotropic and densely packed numerical sample in PFC3D are described in Section 5.3. Some features of the generated sample (e.g. strain and stress measurements) are introduced in Section 5.4 and summary is given in Section 5.5.

5.2 Review of Packing Characteristics of Spheres

It is important to understand packing characteristics of spheres before generating a numerical sample in the DEM simulation. The basic parameter related to packing spheres is the packing density, which is the ratio of the volume of the spheres to the overall volume of numerical sample. Since the packing characteristics of a highly idealised asphalt mixture is known dense random packing, it is important to refer to this background and review the packing characteristics of spheres.

Scott (1960) defined dense random packing as the upper limit of packing density when equal sized-spherical balls are poured into a rigid container. His experimental work showed that the packing density is 0.63 for dense random parked spheres. The same result has been observed by Sohn and Moreland (1968) when they conducted a series of experiments on sand to investigate the size distribution effect on packing density.

The number of contacts (coordination number) between adjacent spheres is another important parameter in characterising the packing spheres. Berzrukov *et al.* (2001) found that contacts between spheres determine the physical connectivity of the packed spheres and the transfer of forces. By using the spatial statistic approach, they found that the average coordination number is 6 for dense randomly packed spheres. However, for real packing of equal spheres, Bernal and Mason (1960) observed an average coordination number of 6.4 for a “random close” packing with a packing density of 0.62.

Consequently, it was decided that the numerical sample generated to replicate the idealised asphalt mixture comprising approximately singe-sized sand should have dense random packing and a target density of 0.63 and an average coordination number of 6.

5.3 Numerical Sample Preparation

5.3.1 Boundary and particle generation

The general principal to prepare a numerical sample is that the particle assembly will be generated and compacted within a set of confining boundaries. Therefore, the first step is to generate the boundary (wall in PFC3D) as the confinement for the particles (balls in PFC3D) which are generated in the second step. The boundary is a set of confining planes that has arbitrarily defined contact properties for interaction with the particles. The finite walls act as a boundary constraint to restrict the movement of particles through the boundaries. Contact forces between the boundary and particles are determined by force-displacement law, which is the same as a ball-ball contact as described in subsection 3.3.2. In a uniaxial simulation, the top and bottom boundaries act as loading platens whilst the lateral boundary is removed after the sample preparation. The typical boundaries generated for a cylindrical sample are shown in Figure 5.1.

After generation of boundaries, a dense randomly packed sample with an approximate volume percentage of 64% solids is generated. The desired number of particles generated to occupy the available space is calculated using the following equation:

$$N = \frac{3V(1-n)}{4\pi R^3} \tag{5.1}$$

Where N is the target number of particles to be generated, V is the total volume of given space, n is the desired porosity and R is the radius.

The particles are set to be generated to the same final particle size. The particles are firstly generated to half of their final size randomly within the boundaries such that no two particles overlap with each other, as shown in Figure 5.2. Then, the particle radii are increased to their final values, as shown in Figure 5.3.

It should be noted that the procedure above can only generate the sample to the final porosity that is close to the required porosity. The true porosity of the sample will be measured by using the ‘Measurement Sphere’ as described in section 5.4.1.

5.3.2 Isotropic equilibrium state

To generate a numerical sample to replicate the idealised asphalt mixture, it is important to ensure that the sample is initially isotropic and free of internal force. However, after the particles are expanded to their final radii, there is a relatively large amount of particle overlap at contact points which results in a non-uniform distribution of contact forces within the sample.

To achieve an isotropic equilibrium condition, the particles are allowed to re-orient themselves until the internal stresses within the sample are approximately isotropic. This is achieved by including a pre-load cycling in the program where the particles are allowed to 'settle' to equilibrium so that the contact forces of particles will be distributed uniformly. It should be noted that during the pre-load cycling, the friction coefficient between the wall and particle is set to zero temporarily to facilitate the re-orientation process.

It has been aware that a sample prepared under the above conditions has a high level of isotropic stress (typically ≈ 10 *MPa*). It should be noted that the sample must have a low (or negligible) internal stress prior to testing. This can be done by slightly reducing the radii of particles and cycling to the equilibrium state. When the radii of all the particles are reduced, the magnitude of overlap between particles decreases, which causes a reduction in the contact forces in the sample. During this process, the particles are again allowed to re-orient themselves so that the sample can be maintained at equilibrium isotropic state. The effect of the reduction in particle radii on the isotropic stress is shown in Figure 5.5. It is suggested by ITASCA (2003) that the isotropic stress needs to be reduced to less than 1% of the uniaxial compressive strength. Consequently, an initial stress of 1 *KPa* is used in the following simulations.

The contact force distribution under isotropic equilibrium state is shown in Figure 5.6. The lines in the figure represent the compressive forces while the thickness of the lines corresponds to the magnitude of compressive force. It can be seen from this figure that the contact forces are uniformly distributed throughout the sample which is expected under an isotropic equilibrium state.

5.3.3 Preparation of bonded particles

The previous subsection described the preparation of a "stress free" numerical sample. To represent asphalt mixture as a composite material, a procedure of preparation of a bonded sample is described in this subsection. In PFC3D, a contact bond cannot be created until the particles have a real contact with the non-zero overlap. Therefore, a high coordination number (defined as the average number of contacts per particle) is required to create a good contact bond network so that its behaviour can be fully represented in modelling. It has been suggested by Rothenburg *et al.* (1992) that the particle assembly needs at least four contacts per particle on average to carry the load. It has also been shown by Collop *et al.* (2004) that a particle assembly with at least 4 contacts per particle on average is necessary to model the internal contact structure of sand asphalt mixture.

To create a sample with a good contact network, it is necessary to make sure that every particle has a minimum of four contacts with its neighbouring particles. This is done by firstly scanning every contact in the sample to detect particles with less than four contacts. These particles are then expanded slightly (typically less than 1%) to create additional contacts with neighbouring particles. During this process, the particles are also allowed to re-orient themselves to assure the sample is in an isotropic equilibrium state. It has been shown by Lee (2006) in a similar numerical sample generation procedure in PFC3D that particles with less than four contacts comprise typically 5 to 8% of total number of particles in the sample. Figure 5.7 shows a typical image of the location of these particles in a numerical sample.

After completing the above procedure, a numerical sample is prepared in a dense randomly packed state with low isotropic internal stresses and a minimum of four contacts per particle. To prepare a bonded sample, normal and shear contact bonds are added to all contacts in the sample shown in Figure 5.8. It should be noted that a new contact bond will be created automatically as new contacts formed in the sample during simulations.

5.3.4 Preparation of uniaxial simulations

This subsection describes the procedure to prepare the numerical sample for uniaxial simulations. The cylindrical numerical sample is confined by the top, bottom and lateral walls. The top and bottom walls simulate the loading platens while the lateral wall acts as the confinement (in triaxial simulation). To prepare the sample for uniaxial simulation, the lateral wall has to be removed (deleted in PFC3D) to give zero confinement to the sample. As described in previous sections, the sample is prepared to a low internal stress condition before removing the lateral wall. However, removal of the lateral wall causes some unloading resulting in a self-equilibrium set of compressive and tensile locked-in forces. After the sample re-settles to a equilibrium state, a typical locked-in force distribution (compression and tension) in the sample is shown in Figure 5.9. It should be noted that the typical locked-in forces are less than 0.01% of the average contact force in the sample. Therefore, the locked-in forces are considered to be negligible in further numerical simulations.

5.4 Method of Measurement

5.4.1 Measurement sphere

A measurement sphere is defined as a specified volume of space in the PFC3D which is capable of measuring important properties of the numerical sample, e.g. porosity, coordination number, stress and strain. This specified 3D volume of space is usually a sphere, so is referred to as a “measurement sphere”. A measurement sphere with a specified radius can be installed at any point within the sample. In later simulations, two measurement spheres with the same radius have been adopted where the porosity and coordination number of the sample have been measured, as shown in Figure 5.10.

Porosity

Porosity of a numerical sample means the air void content of the specified volume of space. In theory, porosity n is defined as the ratio of total void volume within the measurement sphere to measurement sphere volume.

$$n = \frac{V_{void}}{V_{sphere}} = \frac{V_{sphere} - V_{ball}}{V_{sphere}} = 1 - \frac{V_{ball}}{V_{sphere}} \tag{5.2}$$

Where V_{sphere} is the volume of the measurement sphere, V_{void} is the volume of air voids within the measurement sphere and V_{ball} is determined by:

$$V_{ball} = \sum_{N_p} \left(V_p \right) - V_{overlap} \tag{5.3}$$

Where V_{ball} is the volume of the measurement sphere occupied by balls. N is the number of balls that intersect the measurement sphere and $V_{overlap}$ is the volume of particles overlapping contained within the measurement sphere.

Therefore, since the measurement sphere accounts for the volume of particles overlapping it is concluded that the measurement sphere is able to measure the porosity of a synthetic material in a numerical simulation with great accuracy. This measurement method has been utilised in later simulations to measure the porosity of the numerical sample.

Coordination Number

The coordination number C_n is defined as the average number of contacts per particle. It is another important parameter which can be measured from the measurement sphere. It should be noted that only the particles with their centroids contained within the measurement sphere will be used for calculation of the coordination number, using:

$$C_n = \frac{\sum_{N_b} n_c^{(b)}}{N_b} \tag{5.4}$$

Where N_b are the number of particles with centroids contained within the measurement sphere and n_c is the number of contacts between balls.

The tracking of coordination number is important in the whole process of simulation due to the minimum requirement of certain contacts per particle, as described in subsection 5.3.3. The coordination number is updated during each time step to track change of contacts.

5.4.2 Measurement of axial stress and strain

The original coordinates of the top and bottom loading platens firstly recorded in computer memory prior to testing. The platen coordinates are then updated at each time step during the simulation. The axial strain of a numerical sample is calculated based on the relative position change of the same loading platen before and after simulation. It should be noted that the overlapping magnitude (under compression) of the wall and adjacent balls is relatively small compared to the axial displacement of the sample and hence it is negligible.

The axial stress was calculated from the contact forces between the particles in contact with the loading platens divided by the platen area. It should be noted that a constant platen area has been used, the stress which is calculated during simulations are referring to nominal stress.

5.4.3 Measurement of radial strain

The measurement of radial strain in the numerical simulation is much more complicated compared to measurement of axial strain. In a typical laboratory experiment the radial strain is measured at the specimen boundary using a LVDT. Hence, this subsection describes a similar way in the numerical simulation to measure the radial strain. To measure the radial strain in a numerical sample, artificial "measuring gauges" (replicating the function of the LVDT in the laboratory) have been constructed from specified particles at the boundary of a numerical sample (Lee, 2006). The following measurement procedure has been adopted to measure the radial strain of a numerical sample:

1) Particles at the boundary are assigned as measuring gauges,
2) The original coordinates of these particles are recorded in computer memory prior to loading,
3) Updated coordinates of these particles are tracked during the simulation,

4) The radial strain for each particle is calculated based on the difference between updated and original coordinates and,
5) The radial strain for the whole sample is calculated by averaging the radial strain from all particles.

It was initially intended to use all the particles on the circumference of the sample to measure the radial strain in the numerical sample. However, it has been shown that this approach is computationally expensive due to the large number of particles to be monitored during the simulation. Consequently, the "gauge thickness" has been introduced by specifying the height of the gauges on the circumference with respect to the sample height. Two samples with gauge thickness of 0.4 and 0.8 are illustrated in Figure 5.11 and 5.12.

A number of simulations have been performed to investigate the effect of gauge thickness in measurement values. Two samples with elastic contact stiffness and contact bonds containing 6,000 and 12,000 particles were used. The radial strains were measured using different gauge thickness for the different samples. The percentage error compared to the value calculated using all particles on the circumference was calculated for different thickness and is plotted in Figure 5.13. It can be seen in Figure 5.13 that the percentage mean error reduces from 4% to 1% when the gauge thickness increases from 0.1 to 0.8. It can be concluded that a gauge thickness of at least 0.8 is required to ensure the radial strain is within the 1% of the value calculated using all the particles on the circumference.

5.5 Summary

The following conclusions can be drawn from this chapter:

1) A numerical sample procedure has been developed to generate a numerical sample that can replicate the real testing specimen in the laboratory.
2) The packing characteristics of the numerical sample generated are dense randomly packed with a porosity of approximately 0.36.

3) The numerical sample is prepared to an isotropic equilibrium state with low internal stresses.

4) The coordination number of each particle has been monitored and the particles have been adjusted to maintain the minimum contacts of other particles.

5) Normal and shear bonds have been added to each contact point to represent the bonded material characteristics.

6) The cylindrical boundary was removed before the uniaxial simulation has been performed.

7) A measurement sphere is employed to measure the porosity and coordination number of the sample.

8) Radial strain is measured by tracking the displacement of particles on the circumference of the sample while axial strain is calculated based on the relative displacement of the loading platens.

9) Nominal axial stress can be calculated from contact forces between the particles in contact with loading platen divided by the constant platen area.

According to this procedure, a range of numerical sample sizes with a different number of particles can be generated arbitrarily. Figure 5.14 shows a sample comprising 6,000 identical particles, each particle having a diameter of 1.77 mm (thus representing the average particle size of the sand used in the experimental testing). The numerical sample was densely packed with an average 5.8 contacts per particle, the particles thus occupying 63.5% of the total volume. The lock-in force between each particle was adjusted to less than 1 *KPa*. The numerical samples used in the following simulations were all generated using this procedure but various model parameters may be used for different purposes.

5.6 Figures

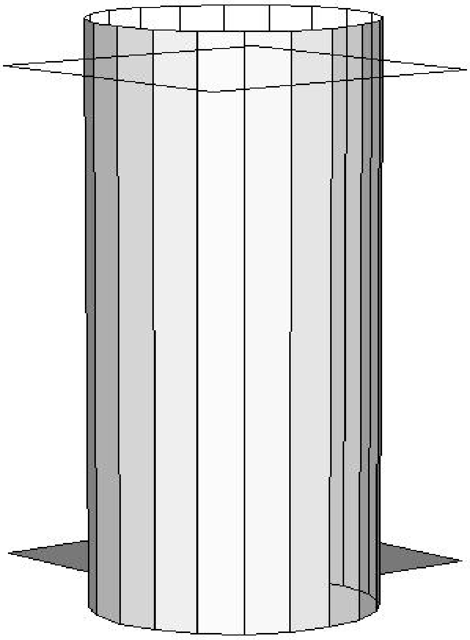

Figure 5.1: Boundaries generated in PFC3D.

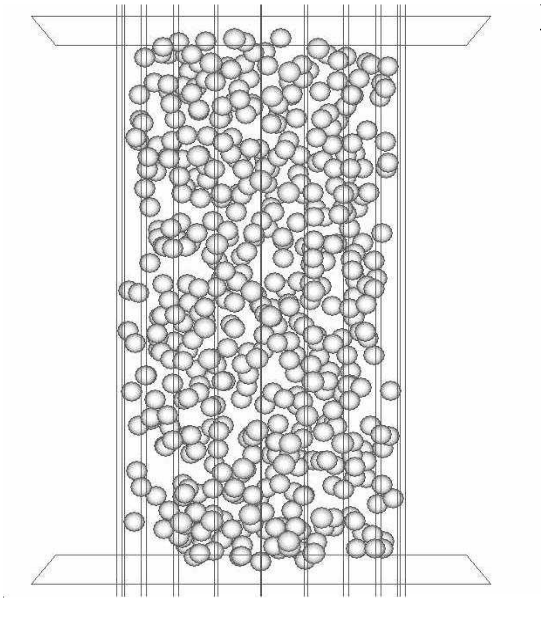

Figure 5.2: Particles generated randomly in space to half of final size.

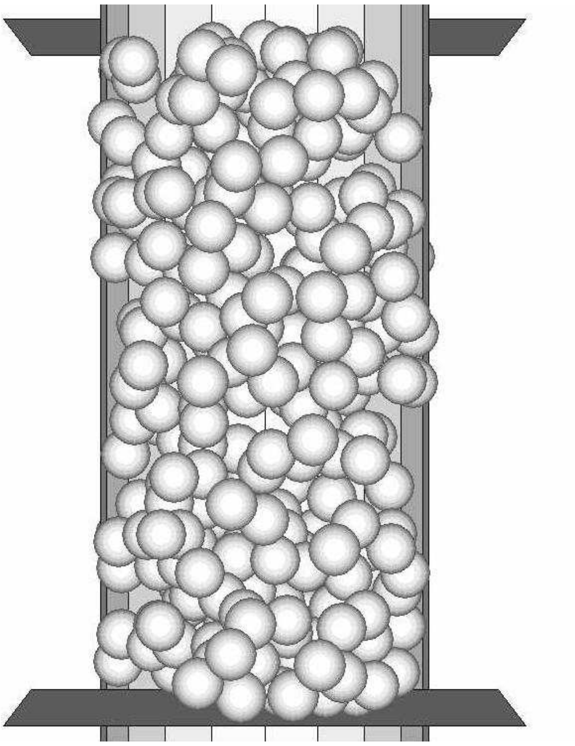

Figure 5.3: Particles expanded to final radii.

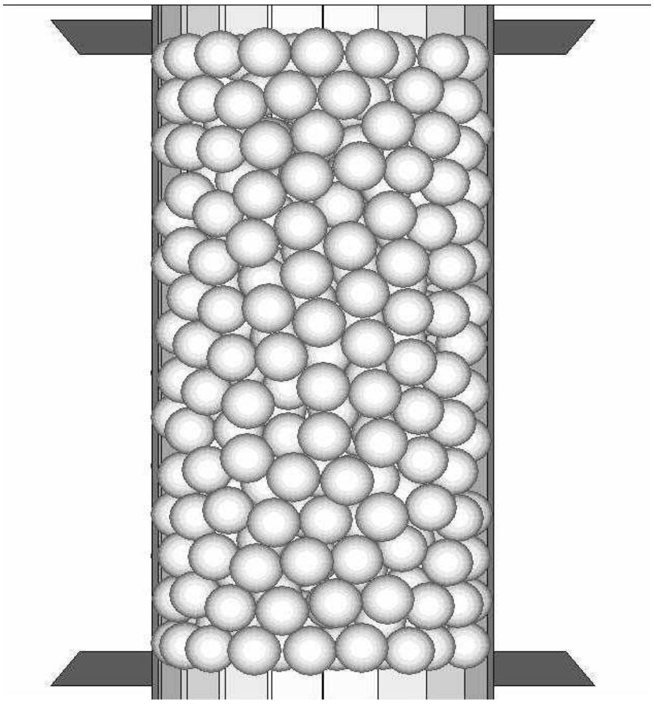

Figure 5.4: Particle re-oriented to isotropic equilibrium state.

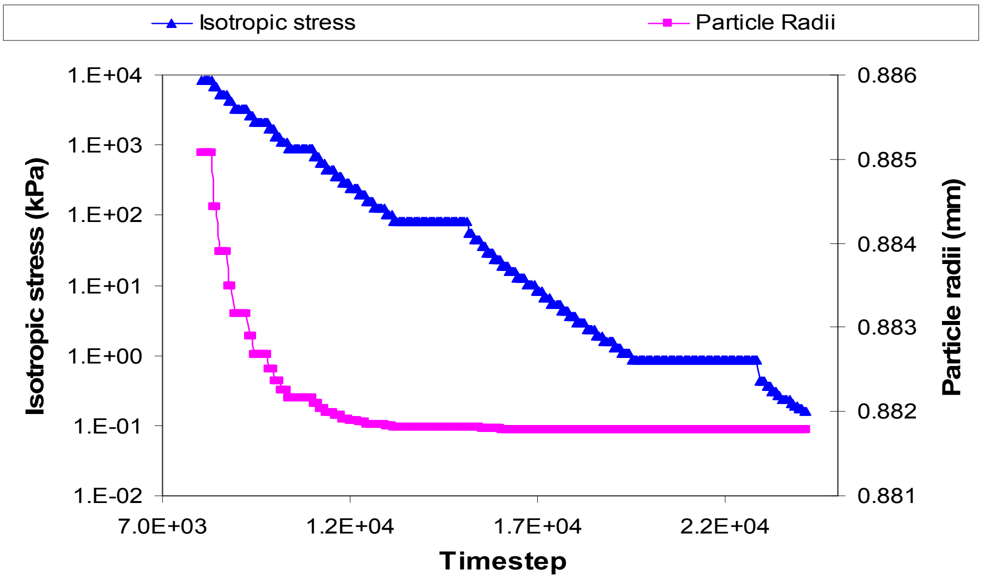

Figure 5.5: Effect of reduction of particle radii on isotropic stress.

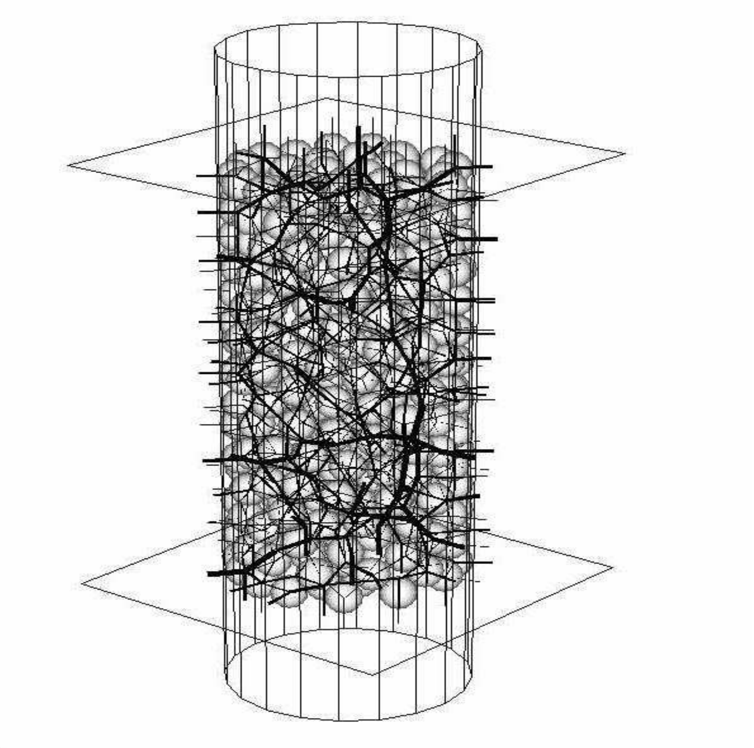

Figure 5.6: Contact force distribution under isotropic stress.

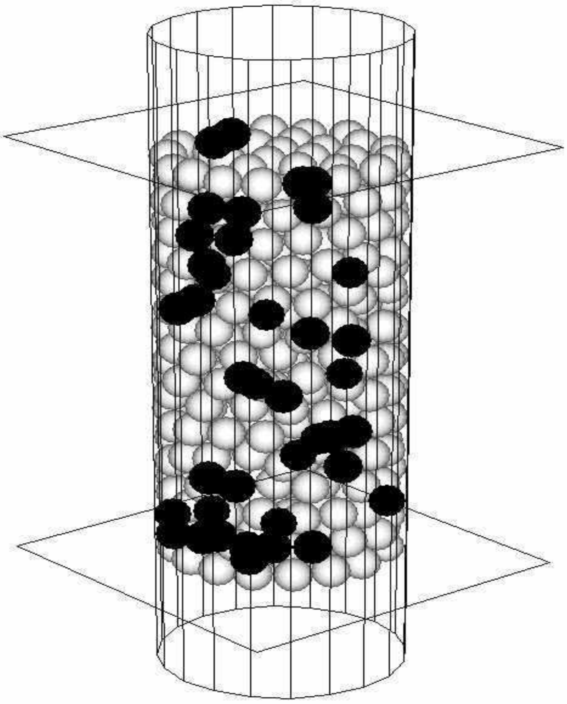

Figure 5.7: Location of particles with less than four contacts.

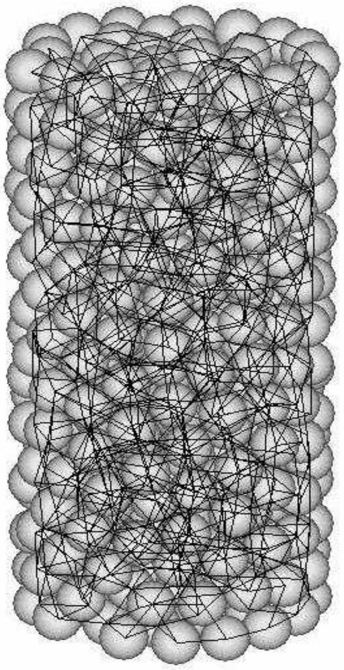

Figure 5.8: Contact bond network.

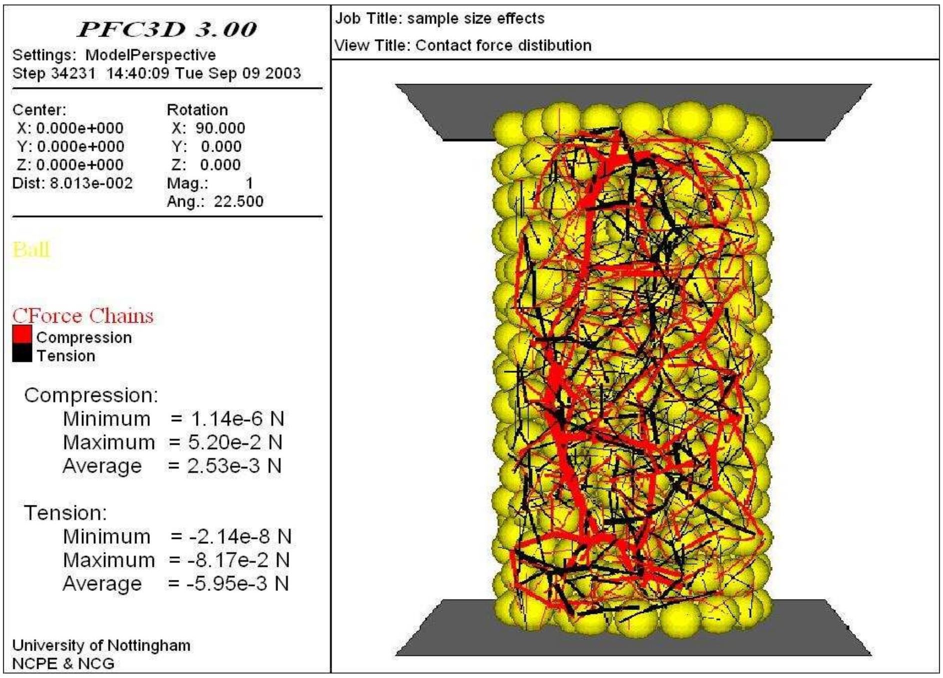

PFC3D 3.00
Settings: ModelPerspective
Step 34231 14:40:09 Tue Sep 09 2003

Center:
X: 0.000e+000
Y: 0.000e+000
Z: 0.000e+000
Dist: 8.013e-002

Rotation
X: 90.000
Y: 0.000
Z: 0.000
Mag.: 1
Ang.: 22.500

Ball

CForce Chains
🟥 Compression
■ Tension

Compression:
Minimum = 1.14e-6 N
Maximum = 5.20e-2 N
Average = 2.53e-3 N

Tension:
Minimum = -2.14e-8 N
Maximum = -8.17e-2 N
Average = -5.95e-3 N

University of Nottingham
NCPE & NCG

Job Title: sample size effects
View Title: Contact force distibution

Figure 5.9: Locked-in forces in tension and compression.

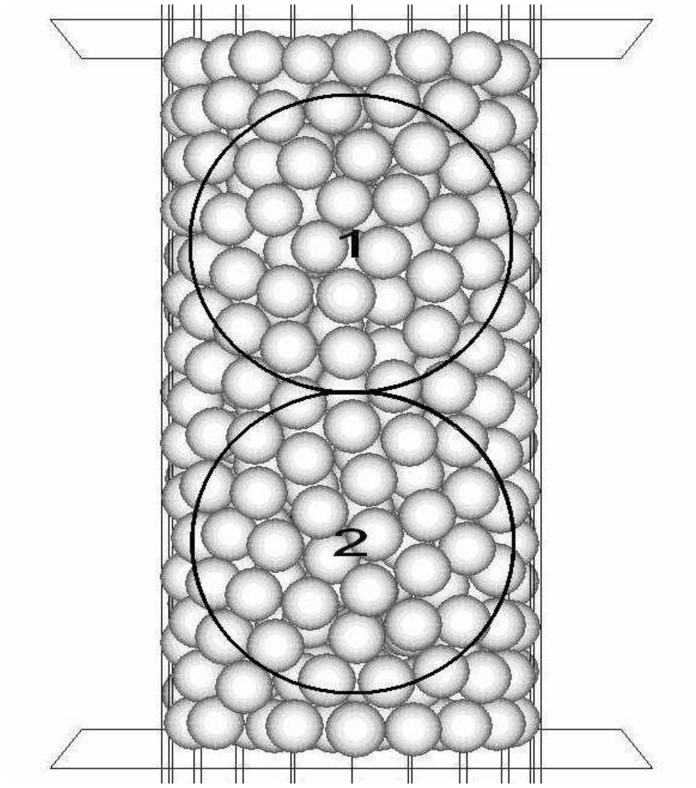

Figure 5.10: Measurement spheres in the sample.

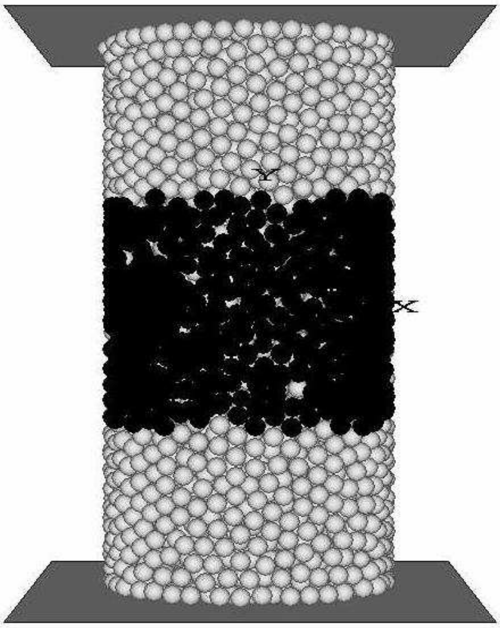

Figure 5.11: Gauge thickness of 40% to sample height.

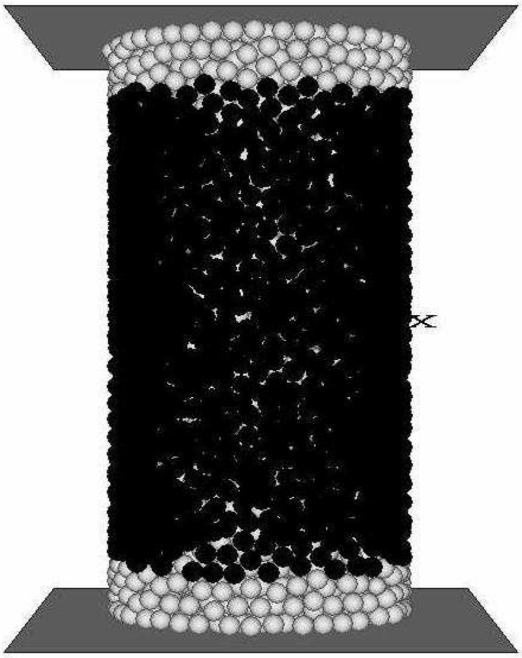

Figure 5.12: Gauge thickness of 80% to sample height.

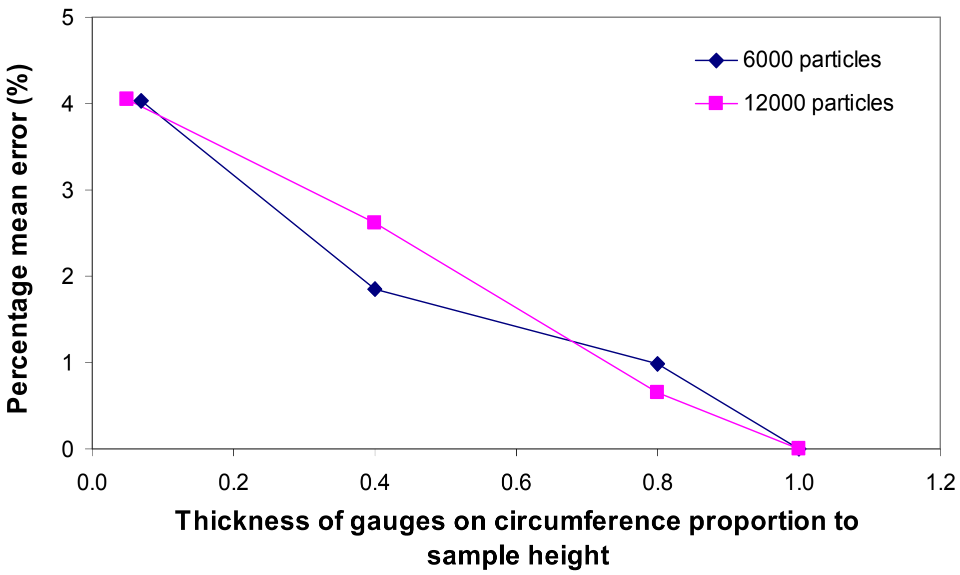

Figure 5.13: Percentage mean error of two samples at different thicknesses of gauges.

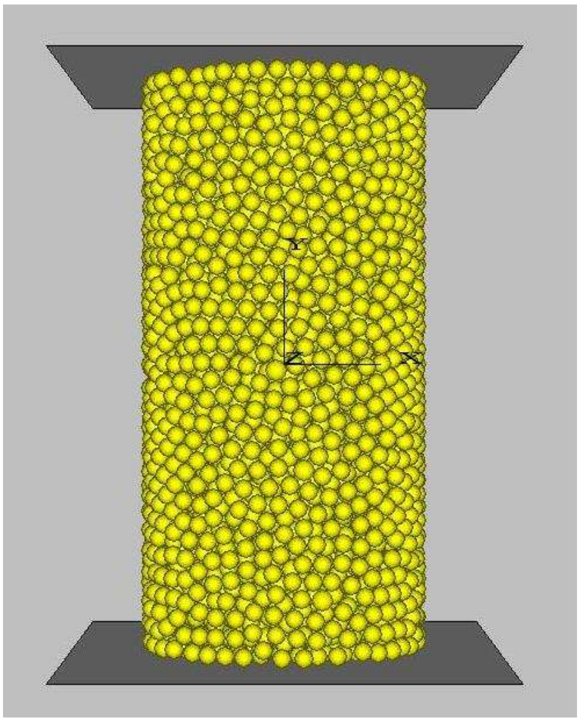

Figure 5.14: Numerical sample with 6,000 particles prepared for uniaxial simulation.

6 ELASTIC MODELLING

6.1 Model Properties and Loading Conditions

In this chapter, an elastic contact model has been utilised to simulate the monotonic compressive behaviour (pre and post-peak) of the idealised asphalt mixture in the elastic regime of behaviour (as described in subsection 4.4.1). The effect of the bitumen is represented by a linear elastic shear and normal contact stiffnesses and the sand grains are represented by spherical particles. In DEM simulations, all particles are bonded together with the elastic normal and shear contact bonds to resist the tensile and shear forces between the particles.

Equation 3.17 and 3.18, for normal and shear contact stiffnesses respectively, have been utilised in governing the force-displacement interaction among contacting particles during simulations. Previous researches (Collop *et al.,* 2004; Lee, 2006) have shown that in using the elastic contact model in DEM simulations, although the values of contact stiffnesses can be chosen arbitrarily to give sensible predictions, the factor of 10 between the normal and shear contact stiffness showed to give an appropriate value of Poisson’s ratio. Consequently, a factor of 10 between the normal and shear contact stiffness has been used in all the simulations of this chapter.

Contact bonds were used between the contacting particles. A frictional coefficient has also been used in simulations to limit shear force providing no tensile force existing at the contact when the shear contact bond breaks.

A contact bond breaks when either tensile/shear stress it is carrying exceeds the bond strength, σ_c or τ_c. The normal and shear contact bond strengths, ϕ_n and ϕ_s , are expressed in units of force. The desired strength criterion relating particle strength and contact bond strength is given in *PFC3D* manual (ITASCA, 2003) as:

$$\begin{aligned} \phi_n &= 4\sigma_c R^2 \\ \phi_s &= 4\tau_c R^2 \end{aligned} \tag{6.1}$$

All samples are prepared according to the sample preparation procedure as described in Chapter 5. The model properties that are used for the elastic simulation are summarised in Table 6.1. Single sized particles were used in the simulations. The shear stiffnesses and friction coefficient between platens and contacting balls were set to be zero to avoid sample barrelling and hence ensure a uniform deformation of the sample when subjected to loading.

The top platen (walls) was used to load the numerical sample whilst the bottom platen was fixed during simulations. The loading was achieved in two stages, namely the compaction stage and the loading stage. In the compaction stage, all three walls were controlled by a simulated numerical "servo-control" mechanism; whereby the velocity of these was updated within teach calculation cycle to maintain a target confining stress level of 0.1 *MPa*. The details of compaction stage have been described in subsection 5.3.2 and will not be detailed here for brevity. This stage is necessary to ensure an initial isotropic stress-state and isotropic distribution of particles. In the loading stage, the upper and bottom walls were freed from the servo-control mechanism whilst the cylindrical wall has been removed for uniaxial simulations. The velocity of the upper wall was increased at a constant rate until reaching a predefined final velocity whilst the bottom wall has been fixed. The simulation in the loading stage is advanced in PFC3D using an explicit time-stepping technique that is conditionally stable. In order to maintain the simulation to be stable, the time step should not exceeds the critical timestep, which is continuously changing during simulations (see more details of critical timestep in subsection 3.3.3). During the loading stage, the axial stress and strain has been recorded in each time step according to the method as described in subsection 5.4.2.

6.2 Internal Damage Simulations

It was noted by previous researchers that the growth of internal damage in an asphalt mixture can be simulated in DEM by allowing bonds breaking between adjacent particles (Kim *et al.,* 2007; Mahmoud 2008). In this section, post-peak (softening) behaviour has been simulated by allowing bond breakage when either normal or shear stress between contacting particles exceeds the normal or shear bond strength. Bond breakage is calculated during each time step of the simulation. A typical simulation result is shown in Figure 6.1 where axial stress and percentage bonds broken are plotted against axial strain.

In this simulation, the shear and normal contact stiffnesses were taken to be 1.2*MPa* and 12*MPa* respectively, the normal and shear bond strengths were taken to be 10*MN* and the friction coefficient between contacting particles where the bond has broken was taken to be 0.5. Please note that the values were chosen arbitrarily so that a general response from simulations of internal damage can be obtained. The axial strain was calculated from the displacement of the top loading platen (the bottom platen was fixed) and the axial stress was calculated from the contact forces between the particles in contact with the loading platens. It can be seen from this figure that the general shape of the predicted stress-strain curve (triangle symbols) is qualitatively similar to the experimental results (Figure 4.4) both in the pre-peak and post-peak regions of behaviour. It can be seen from Figure 6.1 that bond breakage (diamond symbols) increases progressively from about 0.5% axial strain with the greatest rate of bond breakage coinciding with the peak stress (compressive strength).

6.3 Effect of Number and Position of Particles

Since the numerical sample was generated by bonding individual particles together to form a pre-defined shape, it was necessary to determine the minimum number of particles (sample size) so that any bulk properties determined from the simulation (e.g. compressive strength) do not depend on the sample size. In this section, elastic simulations were performed on samples with different numbers of particles to investigate the sample size effect.

To simulate a uniaxial compression test it is necessary to apply a constant velocity (strain rate) to the sample and measure the axial displacement (strain) and axial force (stress) during the test. The same values of parameters were used as section 6.2 and a loading rate of 0.01m/s was chosen to avoid dynamic (wave propagation) effects in the numerical simulations (see more details in section 6.4). Note that since the numerical simulations are elastic in nature, the results do not depend on loading rate provided that dynamic effects are avoided. The coefficient of friction between the loading platens and the sample was set to be zero. The samples were loaded numerically and the simulations were terminated at an axial strain of 3.0%.

Figure 6.2 shows the effect of the number of particles on the predicted compressive stress-strain behaviour. It can be seen from this figure that the curves for 6,000 and 12,000 particles are reasonably close together indicating that at least 6,000 particles are required in the simulations to obtain reasonable estimates of bulk properties such as compressive strength.

In Figure 6.3 the compressive strength (peak stress) is plotted as a function of number of particles (square symbols). Since the placement of particles in the numerical specimen is essentially random, for each number of particles, three separate simulations have been performed with the particles in different random positions. It can be seen from Figure 6.3 that the general trend is for the compressive strength to increase with an increasing number of particles up to approximately 6,000 particles. It can also be seen that the variability caused by the random positions of the particles reduces as the number of particles is increased and the effect for 6,000 and 12,000 particles is small.

6.4 Effect of Loading Rate

Since the stress-strain response in numerical simulation has a dependence on loading rate, it was also necessary to determine the effect of the loading rate on the overall stress-strain responses. The general principle for selecting a loading rate is that the value should preferably be slow enough to eliminate dynamic effects while being fast enough to shorten simulation time. A series of simulations of uniaxial compression test have been performed on an identical numerical sample comprising 6000 particles over a range of loading rates. Figure 6.4 shows the loading rate effect on stress-strain response.

Figure 6.4 shows that convergence occurs beyond peak stress when the loading speed was slower than 0.01*m/s* which implies that a maximum speed of 0.01*m/s* can be chosen as optimum in simulation to eliminate the loading rate effect. Note that since the numerical simulations are elastic in nature, the results do not depend on loading rate provided that dynamic effects are avoided.

6.5 Effect of Bond Strength Variations

In the previous sections, a single value of bond strength has been assumed between contacting particles. However, in reality there is likely to be some variation in bond strength and the objective of this section is to investigate the importance of this variability. The simulations described in Section 6.3 were repeated with identical particle geometries but different Gaussian (normal) bond strength distributions with Coefficients of Variation (CoVs) of 25% and 50% respectively.

The results have been plotted in Figure 6.5 where it can be seen that the compressive strength and the strain at the compressive strength reduce as the variability in bond strength increases. This effect can be clearly seen in Figure 6.3 where the compressive strengths are also plotted versus the number of particles in the specimens. For example, it can be seen that for 6,000 particles, increasing the CoVs from 0% (single value of bond strength) to 50% reduces the compressive strength by approximately 30%.

6.6 Effect of Friction Coefficient

It is well known in soil mechanics that the deformation behaviour of a sand sample is significantly influenced by the interparticle friction. In this section, a series of simulations was performed to investigate the effect of friction coefficient on the predicted stress-strain response. Five numerical samples, each comprising 6,000 particles, were generated with the same particle geometry and bond strength distributions but different friction coefficients ranging from 0 to 0.9 invoked when the shear contact bond between adjacent particles is broken.

The resulting stress-strain curves are shown in Figure 6.6 where it can be seen that the compressive strength increases as the friction coefficient is increased up to a value of 0.5 after which it remains approximately constant.

6.7 Comparison with Experimental Results

Figure 6.7 shows a comparison between predicted results and experimental results. The simulation was performed on a sample comprising 6,000 particles. The shear and normal contact stiffnesses were taken to be 1.2*MPa* and 12*MPa*, respectively. The mean value of normal and shear bond strengths was taken to be 12*MN* with a CoVs of 25% and a friction coefficient was chosen to be 0.5 between particles where the bond is broken. Note that these properties were chosen according to a calibration scheme so that the predicted stress-strain curve matched the experimental curve. It can be seen from this Figure 6.7 that the general shape of the predicted curve (diamond symbols) is qualitatively similar to the experimental results up to a strain level of approximately 2% after which the predicted stress-strain curve flattens out significantly. It might be due to some technical problems in obtaining the accurate force response from the LVDT when the sample is exploding (post-peak region). Moreover, the damage initiation stage (up to the peak stress) concerns us most in this investigation and the true damage mechanism beyond the peak stress is still unknown.

6.8 Summary

The following conclusions can be drawn from this chapter:

1) An elastic contact model has been utilised in DEM to simulate the monotonic compressive behaviour of an idealised asphalt mixture in the elastic region of behaviour.

2) Post peak (softening) behaviour was simulated by allowing bond breakage between adjacent particles. Results showed that the maximum rate of bond breakage occurred at the peak stress (compressive strength).

3) It was found that approximately 6000 particles are required for reasonably accurate estimates of bulk material properties such as compressive strength.

4) It was found that a loading speed of 0.01*m/s* was an optimum speed below which the predicted stress-strain response is not depending on the loading speed providing the dynamic effect has been eliminated during simulations.

5) It was found that the random effect of particle position on predicted compressive strength is not significant compared to variability in bond strength and the friction coefficient. For example, a bond strength distribution with a Coefficient of Variation (CoVs) of 50% reduces the compressive strength by approximately 30% and increasing the friction coefficient from 0 to 0.5 increases the compressive strength by approximately 25% for simulations containing 6,000 particles.

6) The overall shape of the predicted stress-strain curve from the DEM approach showed a qualitatively good agreement with the experimental results up to a strain level of approximately 2%.

6.9 Figures

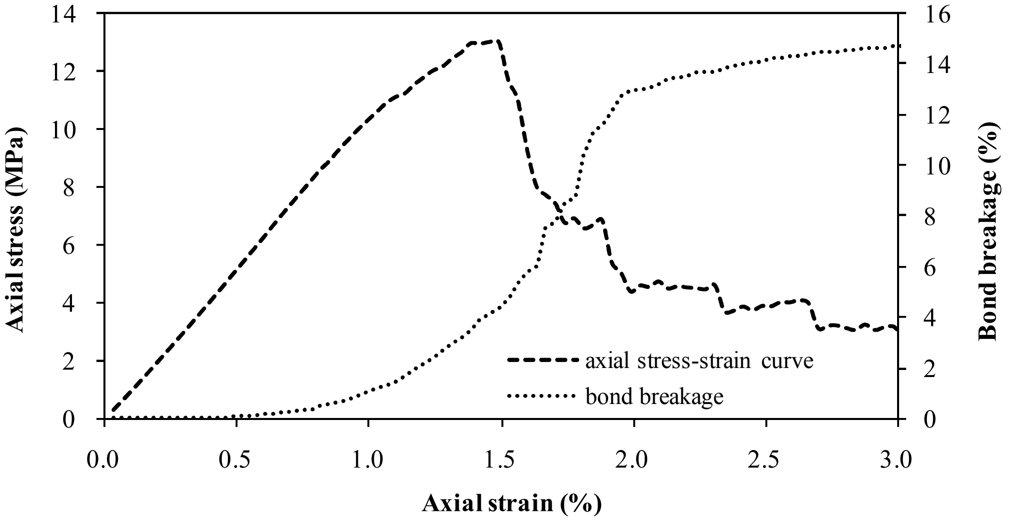

Figure 6.1: A typical simulation result of axial stress-strain response and bond breakage.

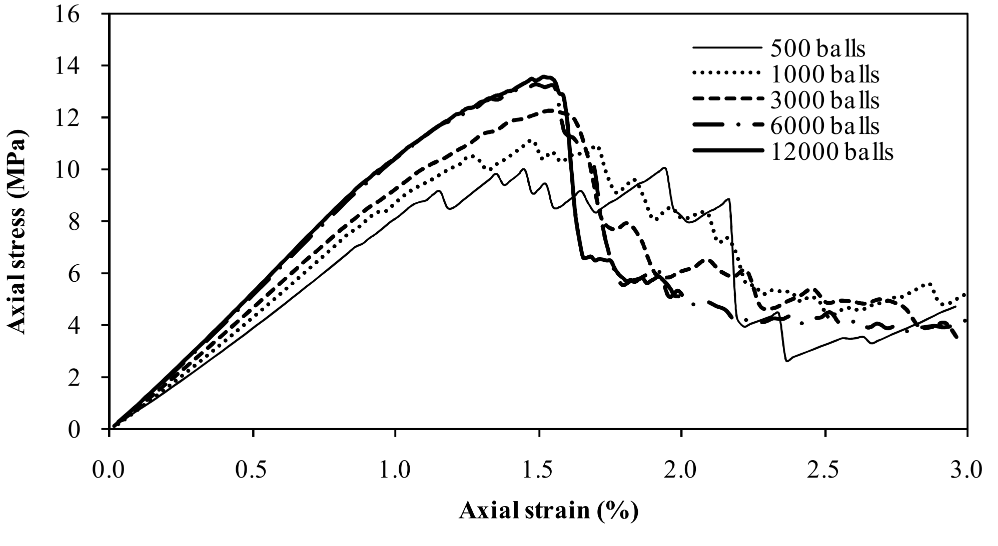

Figure 6.2: Effect of number of particles on axial stress-strain response.

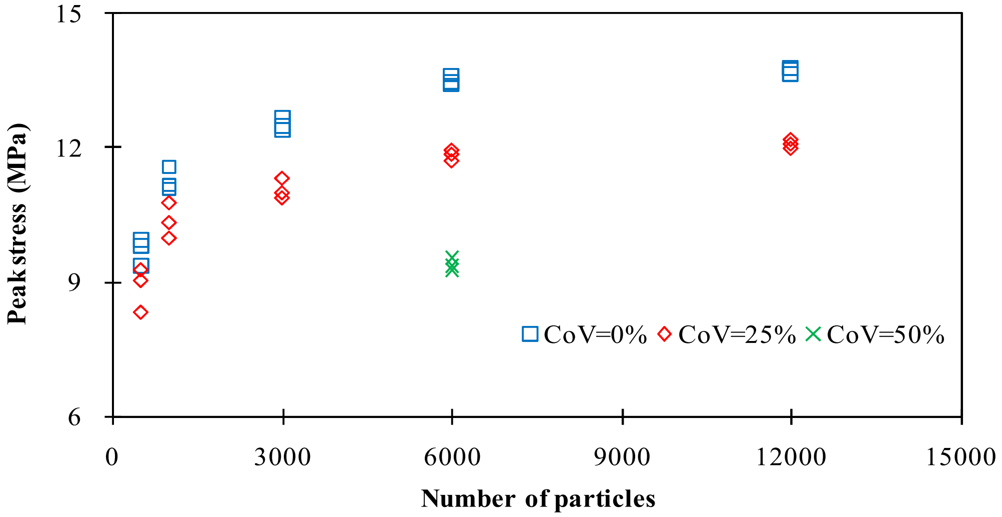

Figure 6.3: Effect of sample geometry and bond strength variations on compressive strength.

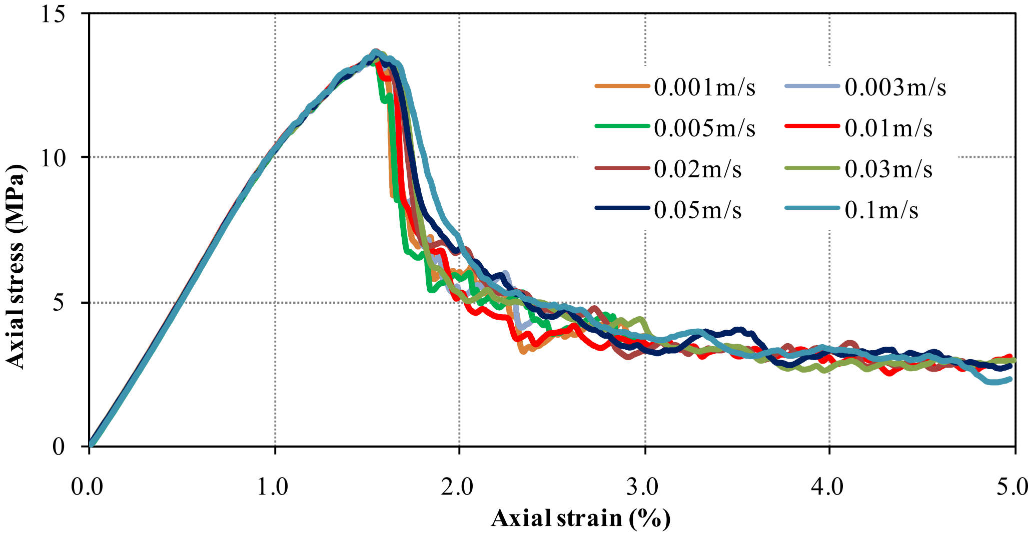

Figure 6.4: Effect of loading rate on axial stress-strain response.

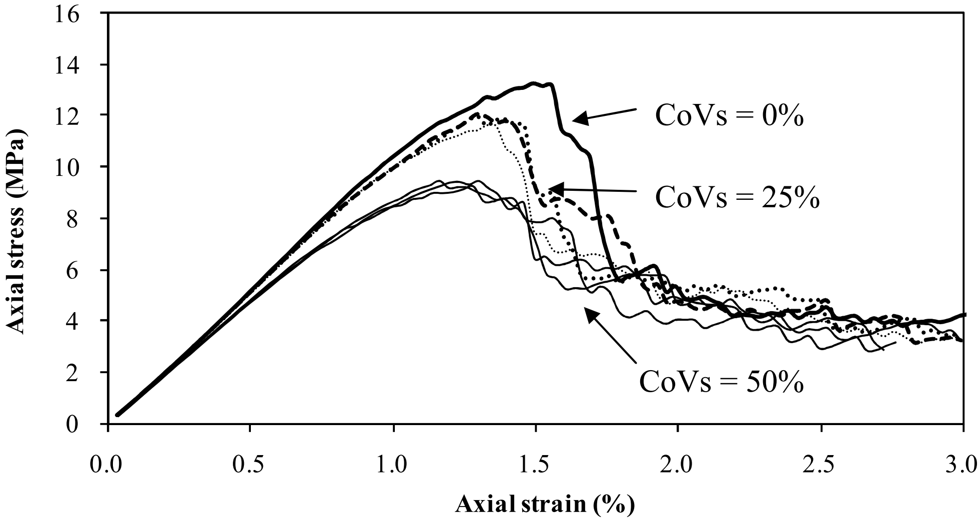

Figure 6.5: Effect of bond strength distribution (CoVs) on axial stress-strain response.

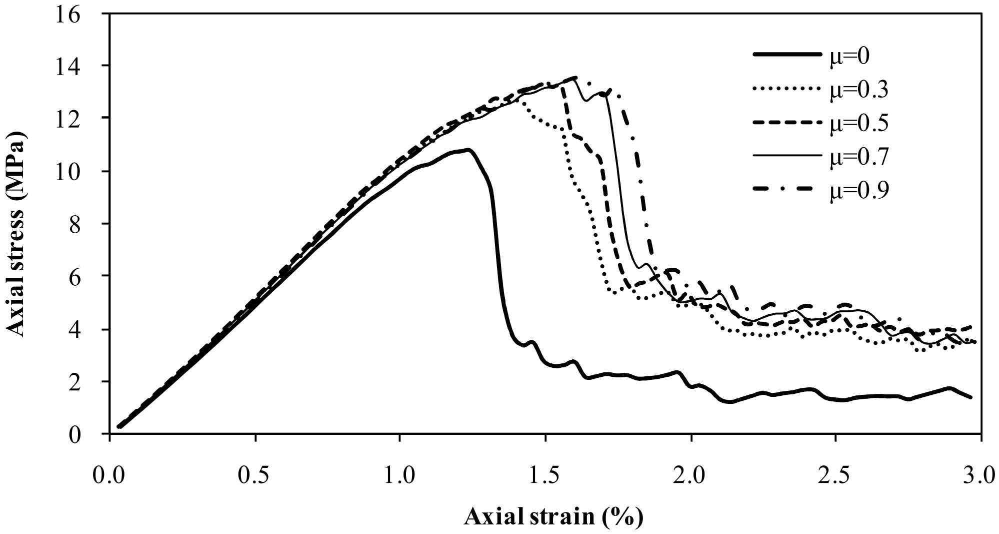

Figure 6.6: Effect of friction coefficient on axial stress-strain curve.

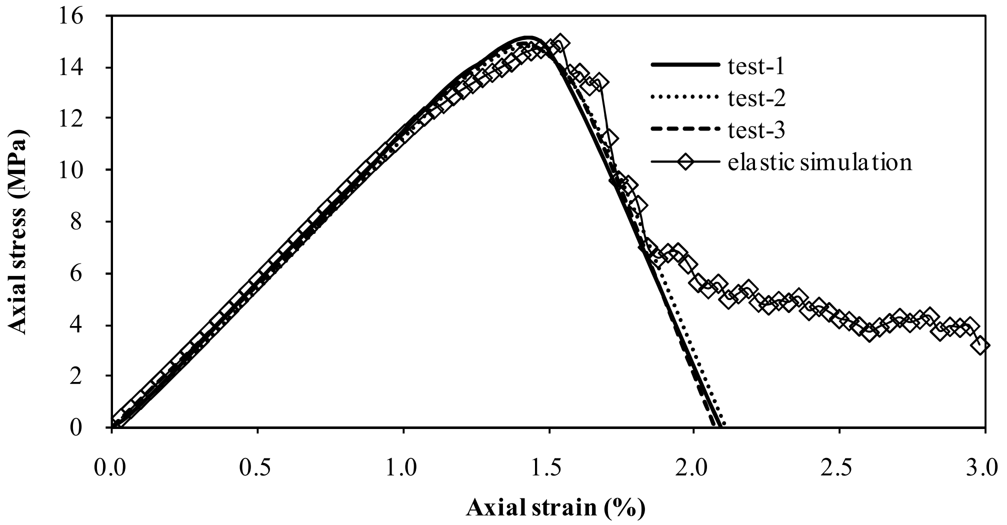

Figure 6.7: Stress-strain response comparison between elastic simulation and experiments.

7 VISCOELASTIC MODELLING

7.1 Introduction

It was noted earlier that the behaviour of the idealised asphalt mixture is dominated by the bitumen and complex aggregate interlock effects are minimised in these types of materials. It has been well documented that asphalt is a viscoelastic material, with properties that are sensitive to ambient temperature and the rate of loadings. It displays both glassy elastic behaviour and viscous behaviour, depending on the combination of temperature and strain rates (Brown and Cooper, 1980; Cheung and Cebon, 1997; Read and Whiteoak, 2003). The simplest way to capture the time dependence of bitumen at particle contacts in a reasonably realistic way in a DEM is to use the Burger's viscoelastic model to represent the contact stiffnesses (Collop *et al.*, 2006).

This chapter presents viscoelastic simulations in DEM used to model the behaviour of the idealised asphalt mixture in the ductile region. Both the strain rate and temperature dependent bond breaking criterion have been investigated. The effect of introducing frictional contacts into the simulations has also been described. The predicted stress-strain response is compared with previously obtained experimental results which have been described in subsection 4.4.2.

7.2 Burger's Contact Model

Bitumen is loading rate and temperature dependent, exhibiting elastic, delayed elastic and viscous behaviour. A simple viscoelastic model is required to capture the time dependent behaviour of bitumen. The simplest option to describe these effects in DEM simulations is to use the Burger's model to represent the normal and shear contact stiffnesses. The Burger's contact model is shown in Figure 7.1. It can be seen that this model comprises a spring with stiffness K_0 (elastic component) in series with a dashpot with viscosity C_∞ (viscous component) in series with a parallel element consisting of a spring of stiffness K_1 and a dashpot of viscosity C_1 (delayed elastic component). It can be readily shown that the time dependent contact stiffness (k) of the Burger's model under creep loading conditions is given by (Collop *et al.* (2004)):

$$k = \left[\frac{1}{K_0} + \frac{t}{C_\infty} + \frac{1}{K_1}\left(1 - e^{-t/\tau}\right) \right]^{-1} \tag{7.1}$$

where t is the loading time and $\tau = C_1 / K_1$ is the relaxation time. It can be seen from Equation 7.1 that the contact stiffness reduces as a function of loading time. This model has been successfully used in DEM by Lee (2006) to model deformation and dilation behaviour of the similar idealised asphalt mixture under creep loading conditions (see (Lee, 2006) for more details).

7.2.1 Constant strain rate analytical solution

In order to model the behaviour of the idealised asphalt mixture under constant strain rate conditions, it is necessary to determine the response of the Burger's model under an imposed velocity. The details of the governing factors in the Burger's model and the analytical solution for the constant velocity condition are described herein.

The total displacement of the Burger's model, u, is the sum of the displacement of the Kelvin section (u_k) and that of the Maxwell section ($u_{mc} + u_{mk}$) of the model, given by Equation 7.2.

$$u = u_k + u_{mk} + u_{mc} \tag{7.2}$$

The first and second derivatives of Equation 7.2 are given by equations 7.3 and 7.4:

$$\dot{u} = \dot{u}_k + \dot{u}_{mk} + \dot{u}_{mc} \tag{7.3}$$

$$\ddot{u} = \ddot{u}_k + \ddot{u}_{mk} + \ddot{u}_{mc} \tag{7.4}$$

The force, *f*, and the first derivative from Kelvin section, are given by:

$$f = K_1 u_k + C_1 \dot{u}_k \tag{7.5}$$

$$\dot{f} = K_1 \dot{u}_k + C_1 \ddot{u}_k \tag{7.6}$$

The force and its derivative from the Maxwell section:

$$f = K_0 u_{mk} \tag{7.7}$$

$$\dot{f} = K_0 \dot{u}_{mk} \tag{7.8}$$

$$\ddot{f} = K_0 \ddot{u}_{mk} \tag{7.9}$$

$$f = C_\infty \dot{u}_{mc} \tag{7.10}$$

$$\dot{f} = C_\infty \ddot{u}_{mc} \tag{7.11}$$

Using Equations 7.3 through 7.11, the following second-order differential equation for the force *f* can be obtained:

$$f + \left[\frac{C_1}{K_1} + C_\infty\left(\frac{1}{K_0} + \frac{1}{K_1}\right)\right]\dot{f} + \frac{C_\infty C_1}{K_0 K_1}\ddot{f} = C_\infty \dot{u} + \frac{C_\infty C_1}{K_1}\ddot{u} \tag{7.12}$$

For convenience, Equation 7.12 is generalised into Equation 7.13:

$$f + p_1 \dot{f} + p_2 \ddot{f} = q_1 \dot{u} + q_2 \ddot{u} \tag{7.13}$$

Where :

$$P_1 = \frac{C_1}{K_1} + C_\infty\left(\frac{1}{K_0} + \frac{1}{K_1}\right) \qquad q_1 = C_\infty$$
$$\text{and} \tag{7.14}$$
$$P_2 = \frac{C_1 C_\infty}{K_0 K_1} \qquad q_2 = \frac{C_1 C_\infty}{K_1}$$

It can be shown for a linear viscoelastic material that the hereditary integral is found by (Flugge, 1975):

$$f(t) = Y(t)u_0 + \int_0^t Y(t-t')\frac{du'}{dt'}dt' \tag{7.15}$$

For Burger's contact model, the stress relaxation modulus *Y(t)* is given by (Flugge, 1975):

$$Y(t) = \frac{1}{\sqrt{p_1^2 - 4p_2}}\left[(q_1 - \alpha q_2)e^{-\alpha t} - (q_1 - \beta q_2)e^{-\beta t}\right] \tag{7.16}$$

Where:

$$\begin{aligned}
\alpha, \beta &= \frac{1}{2p_2}\left(p_1 \pm \sqrt{p_1^2 - 4p_2}\right) \\
P_1 &= \frac{C_1}{K_1} + C_\infty\left(\frac{1}{K_0} + \frac{1}{K_1}\right) \\
P_2 &= \frac{C_1 C_\infty}{K_0 K_1} \\
q_1 &= C_\infty \\
q_2 &= \frac{C_1 C_\infty}{K_1}
\end{aligned} \tag{7.17}$$

Substituting Equation 7.16 and 7.17 into Equation 7.15 and integrating gives:

$$f = \dot{u}\left(\frac{K_0 + \lambda_2 C_\infty}{\lambda_1 - \lambda_2}e^{\lambda_1 t} + \frac{K_0 + \lambda_1 C_\infty}{\lambda_2 - \lambda_1}e^{\lambda_2 t} + C_\infty\right) \tag{7.18}$$

Where:

$$\begin{aligned}
\lambda_1 &= \frac{-P_1 + \sqrt{P_1^2 - 4P_2}}{2P_2} \\
\lambda_2 &= \frac{-P_1 - \sqrt{P_1^2 - 4P_2}}{2P_2}
\end{aligned}
\quad \text{and} \quad
\begin{aligned}
P_1 &= \frac{C_1}{K_1} + C_\infty\left(\frac{1}{K_0} + \frac{1}{K_1}\right) \\
P_2 &= \frac{C_1 C_\infty}{K_0 K_1}
\end{aligned} \tag{7.19}$$

It can be seen from Equations 7.18 and 7.19 that the contact force, *f*, is initially a function of six parameters: $\dot{u}$, K_0, K_1, C_1, C_∞ and *t* (or displacement *u*). It can also be seen from Equation 7.18 that as *t* tends to infinites, the force tends towards a constant value of $C_\infty \dot{u}$. The force calculated from Equation 7.18 is plotted as a function of displacement in Figure 7.2 using the parameters given in Table 7.1. It can be seen from this figure that under a constant velocity condition the contact stiffness (gradient) decreases as a function of loading time (or displacement *u*) due to the viscoelastic nature of the Burger's model.

7.2.2 Modified Burger's model

In DEM viscoelastic simulations, the effect of the bitumen is represented as a viscoelastic shear and normal contact stiffnesses and the sand is represented as spherical particles. All particles are bonded together with the normal and shear contact bonds to resist the tensile and shear forces between the particles. Prior to viscoelastic simulation, the numerical sample is generated according to the same procedure as that used for elastic modelling, except that a Burger's contact model has been used at each contact. It was noted earlier that for the Burger's model the contact stiffness reduces as a function of loading time. Whilst this behaviour is reasonable for the shear and normal tensile contact stiffnesses where the particles are essentially moving away from each other, the normal compressive contact stiffness should increase as particles move towards each other tending towards the contact stiffness resulting from the direct contact between two particles. Consequently, as a first approximation, elastic behaviour has been assumed for the compressive contact stiffness (i.e. no viscous behaviour) whereas viscoelastic behaviour has been assumed for the tensile normal contact stiffness and the shear contact stiffness.

7.2.3 Preliminary modelling with bond breaking criterion

In this subsection, results from a uniaxial simulation based on a modified Burger's contact model (described in subsection 7.2.2) are described. Unfortunately, the Burger's model is significantly more complex than its elastic countpart requiring much more computation time. To increase the computation speed, a sample 7.3*mm* in diameter and 29.2*mm* in height comprising 1,000 particles was used in the simulation. It should be noted that the sample was prepared using numerical sample preparation procedures as described in Chapter 5. Single sized particles were used in the simulations and the friction coefficient between loading platens and particles were set to zero to ensure a uniform stress state of the sample when subjected to loading. A contact bond has been installed at each contact point with a predefined normal and shear bond strength, as shown in Figure 7.3. The bond breakage criterion was used to predict the post-peak softening behaviour in the simulations. The contact bond with variation of 25% (CoVs) in bond strength was chosen in this investigation to give better prediction of the post-peak softening response. The values of the contact stiffnesses used in the simulations are given in Table 7.2.

A uniaxial compression test simulation was performed by applying a constant vertical strain rate of $0.005s^{-1}$ to the sample. The particle contact forces in compression, tension and shear are updated regularly during the simulations. Figure 7.4 shows an example of contact forces distributed in a numerical sample containing 1,000 particles. The red lines represent compressive forces and the black lines represent tensile forces. The thickness of the lines between contacting particles corresponds to the magnitude of contact force generated. It can be seen from this figure that the compressive forces (distributed mainly in the vertical direction) are formed due to the axial compressive loading whilst the tensile forces (distributed mainly in the horizontal direction) are generated at contacts in tension which is resisted by bond strength providing the bond is not yet breaking.

Figure 7.5 shows a plot of the predicted axial stress versus axial strain up to 10% strain level. It can be seen from this figure that, the predicted stress response is a function of strain (or time) comprising initial elastic, hardening and post-peak softening regions. The Modified Burger’s contact parameters (as shown in Table 7.2) can be readily adjusted to further fit the experimental data at a given strain rate.

The contact bond was designed to break when either normal or shear stress between contacting particles exceeds the normal or shear bond strength. The percentage of bonds broken (i.e. bond breakage) with respect to axial strain is plotted in Figure 7.6. It can be seen in this figure that the contact bond breaks progressively from about 1.5% axial strain with the maximum rate of bond breakage coinciding with the predicted peak stress. This observation is consistent with elastic modelling whereby the start of catastrophic internal damage coinciding with the peak stress (compressive strength) in the overall stress-strain response. Figure 7.7 shows the damage modes and locations of broken bonds (microcracks) in the sample at (a) 1% axial strain and at (b) 2% axial strain. The black circle represents the bond breaking in normal (tensile) direction and the red circle represents the bond breaking in shear direction. A few microcracks in the sample can be observed in Figure 7.7(a) at the axial strain of 1% which indicates internal damage starts occurring to the sample (associated with onset of the strain hardening region in Figure 7.5). However, at the axial strain of 2% as shown in Figure 7.7(b), dramatic increase of microcracks can be observed which indicates macroscopic cracks are forming in the sample (associated with onset of the post-peak softening region in Figure 7.5). It can also be seen in this figure that for each axial strain level, the microcracks in both normal and shear damage modes are uniformly distributed throughout the sample.

As a preliminary conclusion, the viscoelastic nature of asphalt can be modelled by assuming elastic contact property for compression and viscoelastic contact property for shear and tension. Moreover, the strength-based bond breaking criterion can be used in viscoelastic modelling to predict the post-peak softening region of behaviour.

7.2.4 Displacement criterion

As an alternative approach to simulate the accumulation of internal damage in the sample in the DEM, the contact bond can be assumed to break based on the relative displacement between the centres of contacting particles. A displacement bond breakage criterion was investigated, mainly because the aforementioned experimental results (as described in Chapter 4) show that the peak strain is nearly strain rate independent for asphalt tested at various strain rates in the ductile region of behaviour. However, this displacement criterion underpredicted the post-peak softening behaviour of the idealised asphalt mixture due to the possible reason that a single value of criterion was used in the simulations.

The details of preliminary investigations of using this displacement criterion in DEM have been described in Appendix A and will not be repeated herein for brevity.

7.3 Computation Time Optimisation

It has been noted earlier that DEM modelling is a powerful technique, but can be time-consuming. It has been well documented in the literature as to how various researchers have tried to reduce the computation time in DEM simulations (Hazzard *et al.*, 2000; Lee, 2006). For example, Lee (2006) suggested that by increasing the magnitude of the timestep in the DEM simulations, the computation time would be reduced. However, it is important to realise that the critical timestep in a particulate system is governed by the speed of sound waves in the material which is a function of the particle masses and the contact stiffnesses. Consequently, increasing the timestep too much is likely to lead to large unbalanced forces. Lee (2006) found that, for simulations of creep, increasing the particle density 100 times resulted in a 3 fold reduction in computation time. However, he also concluded that scaling the particle density will result in an approximately 5% difference in the axial strain response and will also result in higher unbalanced forces during the simulations. Other methods that attempt to reduce the computation time tend to either insufficiently describe the mechanical behaviour of sample (e.g. reducing number of particles in DEM simulations) or limit the modelling to two dimensions. It is important to realise, however, the kinematic constraint imposed by the 2D condition has a fundamental effect on particulate behaviour. Therefore, it is always highly desirable to develop new methods in DEM that are sufficient to describe the 3D mechanical behaviour but keep computation time to a minimum. For a given critical time-step, determined by the masses and contact stiffnesses and for a given ultimate displacement, the required number of timesteps (and hence computational time) will be inversely proportional to loading velocity. Hence, at lower loading velocities it is desirable to see if scaling appropriate parameters such as viscosity can be used instead to maintain the same acceptable computational time.

7.3.1 Scaling C_∞

It can be seen from Equation 7.18 that the contact force *f(t)* is initially a function of six parameters: $\dot{u}$, C_1, C_∞, K_0, K_1 and *t* (or displacement *u*). It can also be seen from

Equation 7.18 that as t gets large, the force tends towards a constant value of $C_\infty \dot{u}$. The aim of this section is to show that constant strain rate tests on asphalt can be simulated at a faster strain rate by scaling appropriate parameters thus reducing the computation time. Several sets of simulations have been performed. For each set of simulations, the effect on the force-displacement response of changing various parameters or the velocity $\dot{u}$ by the same amount is observed. The unscaled parameters used in the simulations are shown in Tables 7.1 and 7.2. Table 7.1 shows the unscaled values used in the analytical solution for the Burger's model and the DEM simulation using 2 contacting balls, and Table 7.2 gives the unscaled values used on a bonded aggregate, described later.

Figure 7.8 shows the results of the first set of simulations: two individual tests have been performed using the Burger’s model; in one test the velocity has been reduced by a factor of 100 and in the other the viscosity C_∞ has been reduced by the same factor. It can be seen that the two curves have the same initial stiffness and constant final force but reducing the viscosity results in overpredicting the force in the intermediate range. Clearly the parallel spring and dashpot must have an influence on the intermediate response and the relative magnitudes of various parameters must govern the behaviour. However, since Equations 7.18 and 7.19 are too complex to explain the behaviour in a simple way, it was decided that a rigorous dimensional analysis should be performed.

7.3.2 Dimensional analysis

The force F can be written as a function of the following 6 physical parameters:

$$F = f(\dot{u}, C_1, C_\infty, K_0, K_1, u) \tag{7.20}$$

It should be noted that time t could be used instead of displacement u. Dimensional analysis dictates that since the 6 parameters contain three physical dimensions: length L, mass M, and time t, the physics of the problem can be described in terms of one dependent dimensionless group and three independent dimensionless groups. One possibility is:

$$\frac{F}{C_\infty \dot{u}} = g\left(\frac{K_0 u}{C_\infty \dot{u}}, \frac{K_1 u}{C_1 \dot{u}}, \frac{C_\infty}{C_1}\right) \tag{7.21}$$

It is now evident that if C_∞ and C_1 are BOTH scaled by the same factor, F will be the same function of displacement as if only the velocity is scaled by the same factor.

Figure 7.9 shows the results from another set of two tests; in one the velocity has been reduced by 100 times and in the other BOTH viscosities C_∞ and C_1 have been reduced by the same factor of 100, and Equations 7.18 and 7.19 have been used to plot the force as a function of displacement. The two curves are identical, demonstrating that Equation 7.21 is correct.

A DEM simulation of two contacting spheres has been undertaken using the Burger's model and used for the analytical solution presented in Figure 7.10. Two sets of simulations have been performed by pulling apart two particles (with one particle fixed) under different test conditions. The first set of simulations was the same as for the analytical solution: that is by either reducing the velocity by a factor of 100 or reducing BOTH viscosities C_∞ and C_1 by a factor of 100. The results are identical, as shown in Figure 7.10(a), and the results are identical to the analytical solution in Figure 7.9. The simulation using unscaled parameters took 1*s* of physical calculation time. The simulation performed reducing the velocity by a factor of 100 took 100s. The simulation performed reducing both viscosities by a factor of 100 took 1s. This demonstrates the power of scaling the viscosities instead of the velocity, which is the main aim of this investigation. The second set of simulations again involves two tests. In one simulation, the parameters were unscaled, and in the other the velocity was increased by a factor of 100 whilst the viscosities C_1 and C_∞ were simultaneously reduced by a factor of 100. The results are shown in Figure 7.10(b), which shows that if the viscosities are reduced by the same factor as that is applied to increase the velocity, the effect is the same as using the unscaled parameters in Table 7.1.

7.3.3 Applications in modelling bonded particles

Further simulations have been performed on a numerical sample with 1,000 bonded particles to simulate the behaviour of an idealised (sand) asphalt mixture. A viscoelastic Burger's model has been assumed for the shear and tensile normal contact stiffnesses and an elastic contact has been assumed for the compressive normal contact stiffness, to represent non-viscous aggregate-aggregate contact. The unscaled parameters are shown in Table 7.2. The first investigation has been performed on simulations without bond breakage (by setting the bond strength to a very high value). Two sets of tests have been performed; one by reducing the velocity by a factor of 100 whilst the other by reducing both viscosities by a factor of 100. In Figure 7.11, the overall stress-strain response from scaling both viscosities is shown to be the same as that from scaling the velocity by the same factor.

Recent research has shown that the internal damage in an asphalt mixture under various loading conditions can be simulated in DEM by allowing bond breakage between contacting particles (Hazzard *et al.*, 2000; Kim *et al.*, 2007; Mahmoud *et al.*, 2008). Therefore, another investigation has been performed following the same procedure as above, but allowing bonds to break progressively during the simulations. The purpose of doing this is to see whether the method of scaling viscosity to velocity is applicable where internal damage occurs. The stress-strain curves have been plotted in Figure 7.12, which show close agreement between scaling velocity and both viscosities, demonstrating that the scaling method is also applicable in DEM simulations with bond breakage.

7.4 Effect of Inter-particle Friction

It is well known in soil mechanics that the deformation behaviour of a sand sample is significantly influenced by inter-particle friction (Lee and Seed, 1967; Huschek, 1985; Ni *et al.*, 1996; Lee, 2006). Huschek (1985) noted that internal friction due to aggregate contact is one of the components contributing to the deformation resistance of asphalt. In the previous viscoelastic simulations, contacting particles are bonded together and either an elastic or viscoelastic contact stiffness is used. As noted above, this approximation is simplistic and there should be some direct contact between the two aggregates prior to testing. Collop *et al.* (2007) performed viscoelastic creep simulations using PFC3D on a bonded-sample and found that the dilation gradient increases as either the frictional coefficient or the percentage of frictional contacts (due to bond absence prior to loading) increases and that approximately 20-30% frictional contacts with a friction coefficient of 0.7 shows good agreement with experimental results.

The direct contact between particles due to bond breaking during simulations is represented by the slip model featured in PFC3D, which is defined by a friction coefficient at the contact (μ) (see more details in subsection 3.4.2). In PFC3D, this model is activated when there is no contact bond specified (due to either bond absence before or during simulations). The contact is checked for slip conditions by calculating the maximum allowable shear contact force described by $F_{\max}^{s} = \mu \left| F_i^n \right|$. Simulations from previous elastic modelling in Section 6.7 showed that increasing the friction coefficient from 0 to 0.7 increased the predicted peak stress by approximately 30% before tending towards a constant value. However, another feature of inter-particle friction due to the direct contact between particles has not yet been included in the previous simulations. This section investigates the effect of inter-particle friction between contacting particles on the predicted stress-strain response in the viscoelastic simulations.

Three series of uniaxial simulations were performed on samples containing 1,000 particles generated according to the sample preparation procedure described in the Chapter 5. The contact parameters are stated in Table 7.3. A 25% CoVs of contact bond strength has been applied to give better prediction of the softening response in the stress-strain curve.

In the first series of simulations, 10% of the total contact bonds (shear and tension) were removed and the shear stiffnesses were replaced by the slip model using friction coefficients of 0.1, 0.5 and 0.9. The second and third series of simulations were the same as the first series except that 20% and 30% of the contact bonds were replaced with frictional contacts, respectively. An example of the results from the second series of simulations is shown in Figure 7.13. It can be seen in this figure that the axial stress is predicted to increase as the friction coefficient increases. For example, it can be seen that at a strain level of 1.5%, the axial stress increases from approximately 9*MPa* to approximately 15*MPa* as the friction coefficient increases from 0.1 to 0.9.

An example of results for different frictional contacts at a certain friction coefficient is shown in Figure 7.14. It can be seen in this figure that the axial stress is predicted to decrease as more contact bonds were replaced with the frictional contacts. For example, at a strain level of 1.5%, the axial stress is predicted to decrease from approximately 20*MPa* to approximately 7*MPa* as the percentage of frictional contacts increases from 0 to 30%. It can also be seen in this figure that a wider range of post-peak softening response is predicted as percentage of frictional contacts is increased.

The predicted peak stresses in the axial stress-strain response for all three series of simulations are shown in Figure 7.15. It can be seen from this figure that the general trend (for all friction coefficients) is for the peak stress to decrease as the proportion of frictional contacts is increased. This is because fewer contact bonds reduce the number of constraints, allowing more freedom for particles to roll over each other resulting in a lower stress level. It can also be seen that, at a certain percentage of frictional contacts, the peak stress increases as the friction coefficient increases.

7.5 Strain-rate Dependent Bond Breaking Criterion

7.5.1 Experimental data justification

The experimental results described in the subsection 4.4.2 have shown that the measured stress-strain response can be generally divided into three regions. In the early stages of the test, the stress increases approximately in proportion to the strain (i.e. linear behaviour). There is then a small region of hardening where the slope of the stress-strain curve decreases as the peak stress (compressive strength) is approached. Preliminary viscoelastic simulations have shown that for a certain testing condition, the post-peak softening behaviour in an axial stress-strain response can be reasonably well predicted using a strength-based bond breaking criterion.

It was noted earlier by previous researchers that the time-dependent characteristic for bitumen becomes more significant when its behaviour is dominated in the ductile region whilst less obviously when its behaviour is in the elastic region. Previous experimental results of sand asphalt mixture (as shown in Figure 4.9) have also shown that the peak stress in the overall stress-strain response is a power-law function of the strain rate in the ductile region of behaviour over a range of temperatures. Similar findings of various bituminous mixtures have also been reported by previous researchers (Cheung and Cebon, 1997; Harvey, 2000; Deshpande and Cebon, 2000; Taherkhani, 2006; Grenfell, *et al.*, 2008). Figure 7.16 shows a plot of peak stresses (normalised by the peak stress at the strain rate of 0.1s^{-1}) against strain rate for results from some typical bituminous materials tested at 20°C. It can be seen in this figure that for a range of types of bituminous materials linear relationships with similar gradients have been observed for measured peak stresses with respect to strain rate on double logarithmic scales. For example, Cheung and Cebon (1997) reported that for 50 pen pure bitumen under uniaxial tensile loading, power-law constitutive relationship between peak stress and strain rate is related by exponent $n = 0.42$. Harvey (2000) found that the 100 pen bitumen showed a greater exponent $n = 0.67$ under similar testing conditions. Grenfell *et al.* (2008) observed the similar constitutive relationships for HRA and DBM materials in constant strain rate tests with a power-law exponent $n = 0.35$ for HRA and 0.26 for DBM, respectively. It should be noted that in Figure 7.16, each set of peak stresses have been normalised by the stress at the strain rate of 0.1s^{-1}.

Simply put, both the experimental results observed in this project and the other researchers have shown that a power-law function can be used to describe the strain rate dependent characteristics of compressive strength in asphalt mixtures. Consequently, in order to model the compressive strength of sand asphalt mixture for different strain rates, both normal and shear bond strength was decided to be chosen as a power-law function of strain rate with the exponent $n = 0.29$.

7.5.2 Temperature variations

It was noted earlier that asphalt is a viscoelastic material whose properties depend on both loading time and temperature. The previous experimental data analysis has shown that the strain rates applied at various temperatures can be converted to the strain rate at the reference temperature by using the Arrhenius model. Consequently, for sand asphalt mixture tested over a range of temperatures, the peak stress is as a function of the temperature-compensated strain rate as follows:

$$\frac{\sigma}{\sigma_0} = \left(\frac{\dot{\varepsilon}_T}{\dot{\varepsilon}_0}\right)^n \tag{7.22}$$

Where $\dot{\varepsilon}_T = \dot{\varepsilon} \cdot \exp\left(k\left(\frac{1}{T_1} - \frac{1}{T_0}\right)\right)$ and T_0 is chosen as 283 K (10°C). The reference stress, σ_0 is 10.3 MPa and the reference strain rate, $\dot{\varepsilon}_0$ is 0.1s^{-1} for sand asphalt tested at 10°C. Therefore, by including the temperature variations into account for the compressive strength, the bond strength B_s can be readily shown as a function of the temperature-compensated strain rate as follows:

$$\frac{B_s}{B_0} = \left(\frac{\dot{\varepsilon}}{\dot{\varepsilon}_0}\right)^n \left[\exp\left(k\left(\frac{1}{T_1} - \frac{1}{T_0}\right)\right)\right]^n \tag{7.23}$$

Where $\dot{\varepsilon}_0$, T_0 and k is the same as in Equation 4.2. The temperature-independent exponent n = 0.29 is used in scaling both normal and shear bond strength in further DEM simulations.

7.5.3 Comparison with experimental data

A comparison between the predictions of the viscoelastic modelling and the uniaxial compression test results as described in the subsection 4.4.2 will be presented in this subsection.

A numerical sample containing 1000 particles was generated according to the sample preparation procedure as described previously in Chapter 5. The unscaled model parameters are detailed in Table 7.4 and were calibrated to given sensible levels of axial stress and a similar shape of stress-strain curve to previously presented experimental results. For all the numerical samples, 30% of the total contact bonds were replaced with frictional contacts (friction coefficient of 0.7).

Two series of simulations have been performed on a prepared sample containing 6000 bonded particles. The approach of computation time optimisation (as described in the Section 7.5) has been used so that stress-strain response can be predicted whilst simulations are maintained at a faster strain rate. A previously justified power-law exponent (*n*) of 0.29 has been used in scaling both the normal (tensile) and shear bond strengths in the modelling as a function of the temperature-compensated strain rates. The normal and shear contact stiffness has also been scaled by the same factor as the bond strength in the simulations.

The first series of simulations was performed with attempts to simulate the experimental data at 10°C over three strain rates. Three simulations of uniaxial compression tests were performed in this series at the same strain rate of $0.5s^{-1}$. For the first simulation, unscaled parameters have been used whilst for second and third simulations both viscosities (C_∞ and C_1) have been multiplied by a factor of 0.2 and 0.04, respectively to simulate the strain rates of $0.1s^{-1}$ and $0.02s^{-1}$. Figure 7.17 shows the simulation results together with the experimental results for sand asphalt tested at 10°C. It can be seen in this figure that the DEM simulations provide a good match with the experimental data in both the pre-peak and post-peak regions of behaviour.

The second series of simulations were performed to simulate the experimental data at 20°C over three strain rates. It should be noted that the three strain rates (0.5, 0.1 and 0,02 s^{-1}) applied at the temperature of 20°C can be converted to the temperature-compensated strain rates of approximately $0.1s^{-1}$, $0.02s^{-1}$ and $0.004s^{-1}$ at the reference temperature of 10°C, respectively. Therefore, for the first simulation, both viscosities have been multiplied by a factor of 0.2. For the second and third simulations, both viscosities have been multiplied by a factor of 0.04 and 0.008, respectively to simulate the temperature-compensated strain rates of $0.02s^{-1}$ and $0.004s^{-1}$. Figure 7.18 shows the simulation results together with the experimental results for sand asphalt tested at 20°C. A good agreement between experimental results and simulation results has been observed.

Additional simulation of tests at 0°C has been performed. The strain rate of 0.02 s^{-1} applied at 0°C can be converted to 0.1s^{-1} at 10°C. Therefore, in this simulation unscaled parameters were used except for that both viscosities have been multiplied by a factor of 0.02 to mimic the strain rate effect. The simulation results together with experimental data have been plotted in Figure 7.19 where a good agreement has also been observed.

In conclusion, strain-rate dependent bond breaking criterion has been proved to be a suitable method in DEM to simulate the uniaxial compression tests on sand asphalt mixture over a range of strain rates and temperatures.

7.6 Summary

The following conclusions can be drawn from this chapter.

1) DEM has been used to simulate the uniaxial compressive behaviour of idealised asphalt mixture in the ductile region over a range of strain rates and temperatures.

2) A viscoelastic Burger’s model was introduced to give time-dependent shear and normal tensile contact stiffness, whilst the normal compressive contact stiffness was assumed to be elastic.

3) A computation time optimisation method has been developed so that the stress-strain response at slower strain rate can be predicted at a faster strain rate in DEM simulations. This computation time optimisation method has demonstrated an acceptable applicability in modelling bonded particles with bond breaking.

4) Friction was introduced to simulate the shear contact behaviour at aggregate to aggregate contacts. The effect of inter-particle friction on the predicted compressive strength has been investigated. The compressive strength was found to increases as either the friction coefficient increases or percentage

frictional contacts decrease. Simulations performed by removing 30% of the bonds using a friction coefficient of 0.7 can predict a similar shape of post-peak softening behaviour as the experimental data.

5) The compressive strength as a power-law function of strain rate has been justified with the temperature independent exponent of 0.29. Temperature-compensated strain rate effect has been included in the DEM simulations.

6) The bond strength has been set as a power-law function of temperature-compensated strain rate in the modelling.

7) It was demonstrated that by using the strain rate dependent bond strength in the DEM simulations provides a good match with the experimental data in both the pre-peak and post-peak regions of behaviour.

7.7 Tables

Parameter	K_o *(MN/m)*	C_∞ *(MNs/m)*	K_1 *(MN/m)*	C_1 *(MNs/m)*	$\dot{u}$ *(m/s)*
Value	1.00	1.00	1.00	1.00	1.00

Table 7.1: Burger's contact parameters for viscoelastic simulations for 2-particle contact.

Shear Contact		Tension Contact		Compression contact	
Property	Value	Property	Value	Property	Value
K_o^s (MN/m)	0.5	K_o^n (MN/m)	0.5	E_o^n (MN/m)	0.5
C_∞^s (MNs/m)	0.5	C_∞^n (MNs/m)	0.5		
K_1^s (MN/m)	0.5	K_1^n (MN/m)	0.5		
C_1^s (MNs/m)	0.5	C_1^n (MNs/m)	0.5		

Table 7.2: Burger's contact parameters for viscoelastic simulations on 1000 bonded particles.

Shear Contact		Tension Contact		Compression contact	
Property	Value	Property	Value	Property	Value
K_o^s (MN/m)	5.50	K_o^n (MN/m)	5.50	E_o^n (MN/m)	5.50
C_∞^s (MNs/m)	0.06	C_∞^n (MNs/m)	0.06		
K_1^s (MN/m)	5.50	K_1^n (MN/m)	5.50		
C_1^s (MNs/m)	0.06	C_1^n (MNs/m)	0.06		

Table 7.3: Burger’s contact parameters for investigations of inter-particle friction.

Shear Contact		Tension Contact		Compression contact	
Property	Value	Property	Value	Property	Value
K_o^s (MN/m)	0.84	K_o^n (MN/m)	2.52	E_o^n (MN/m)	4.90
C_∞^s (MNs/m)	5.60	C_∞^n (MNs/m)	16.8		
K_1^s (MN/m)	0.21	K_1^n (MN/m)	0.63		
C_1^s (MNs/m)	5.60	C_1^n (MNs/m)	16.8		

Table 7.4: Burger’s contact parameters for viscoelastic simulations in experimental data validation.

7.8 Figures

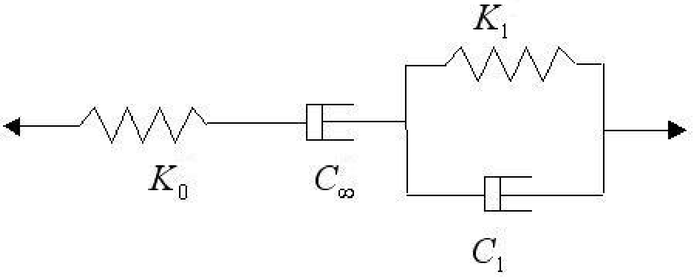

Figure 7.1: Schematic showing the Burger's viscoelastic contact model.

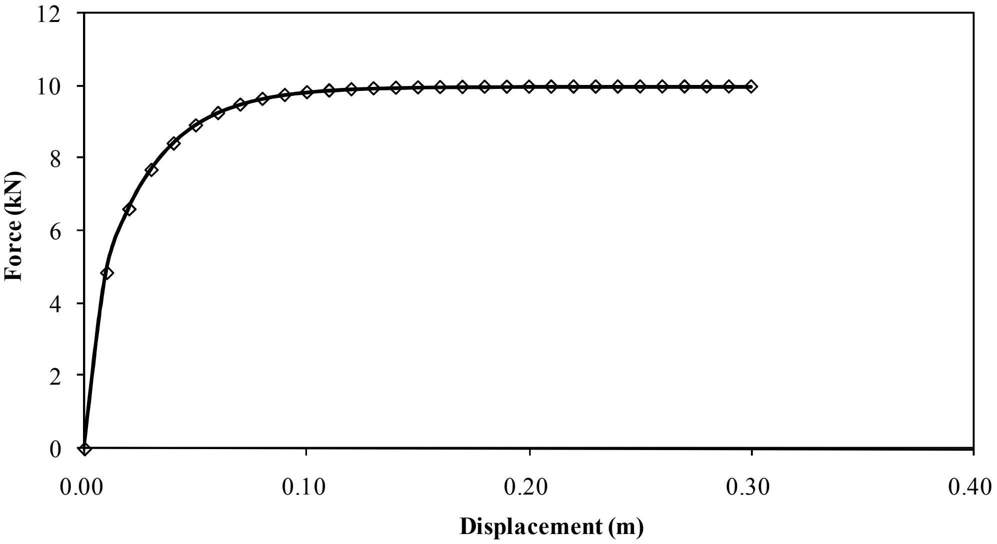

Figure 7.2: Analytical solution to the Burger's model.

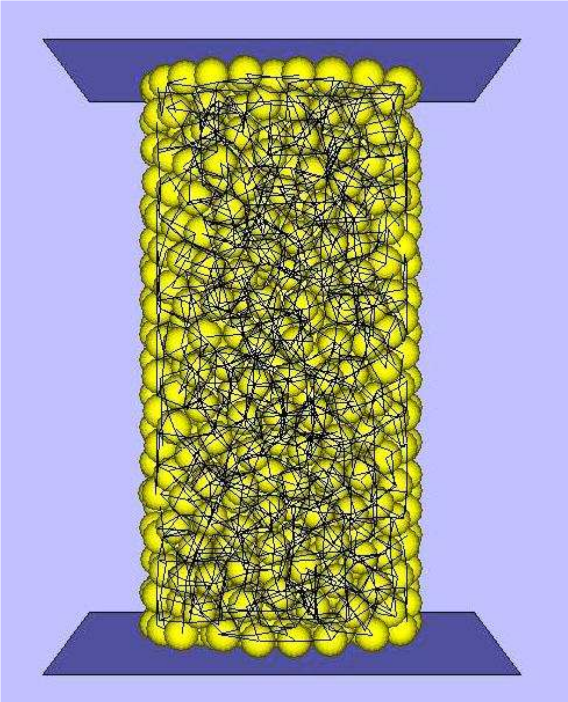

Figure 7.3: Bond network connections in 1000 particles sample.

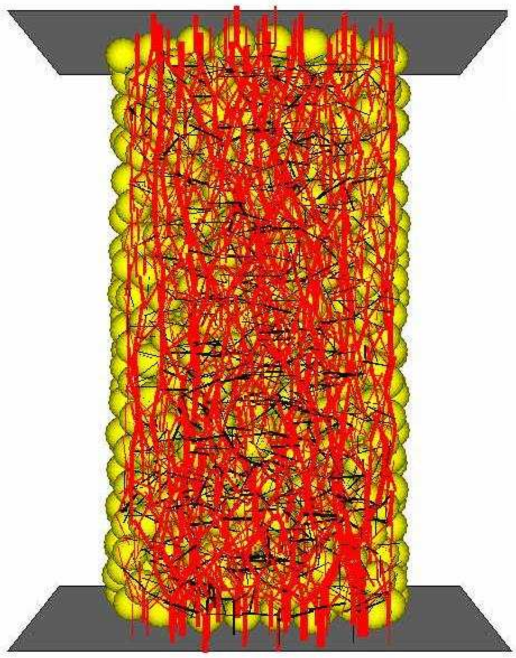

Figure 7.4: Compressive (red) and tensile (black) contact forces distributed in 1000 particles.

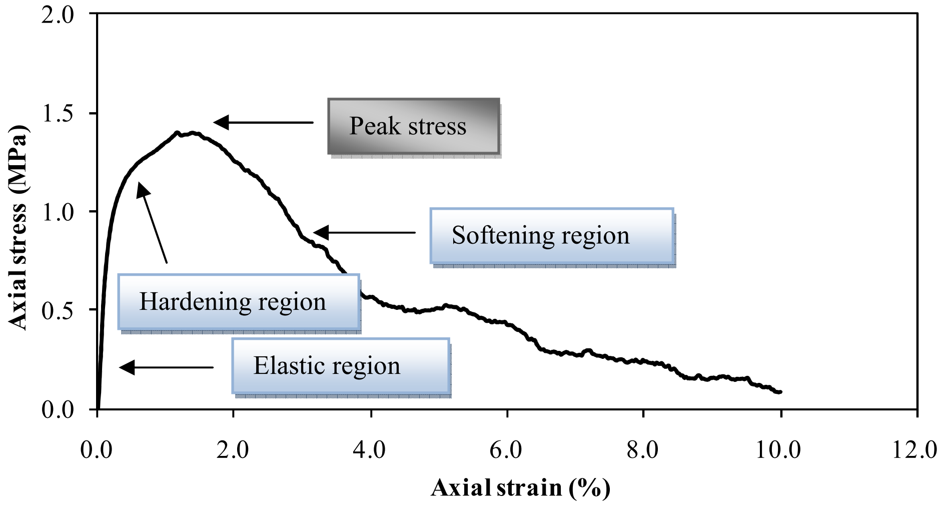

Figure 7.5: Predicted stress-strain curve in preliminary viscoelastic simulations on 1000 bonded particles.

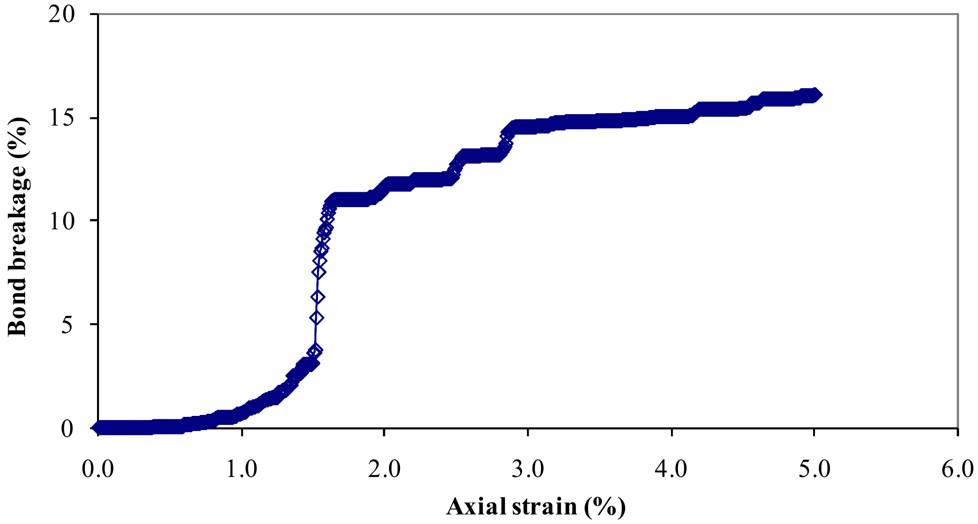

Figure 7.6: The percentage of bonds broken (i.e. bond breakage) with respect to axial strain in a viscoelastic simulation.

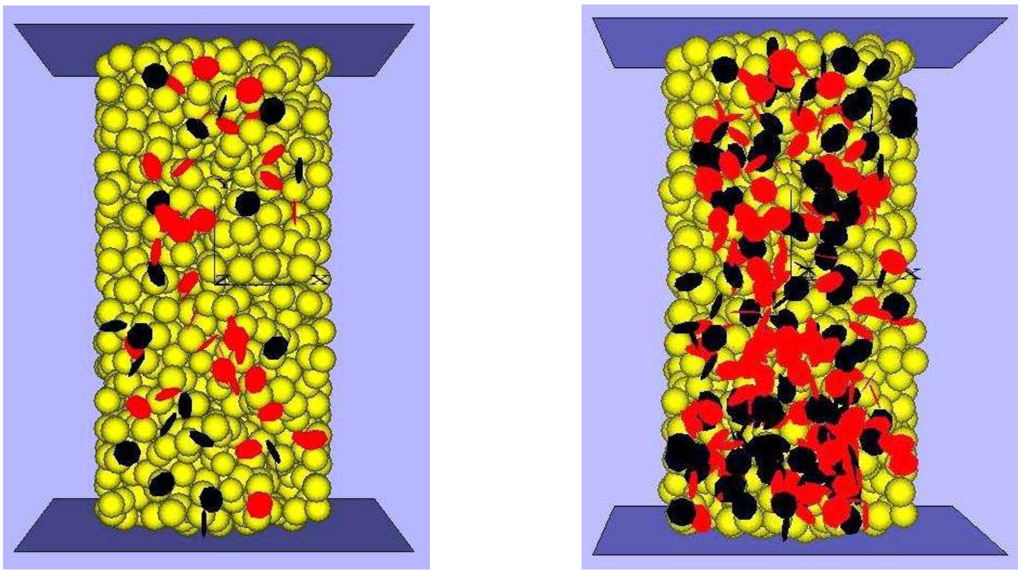

(A) (B)

Figure 7.7: Distribution of broken bonds: (A) at 1% strain level; (B) at 2% strain level.

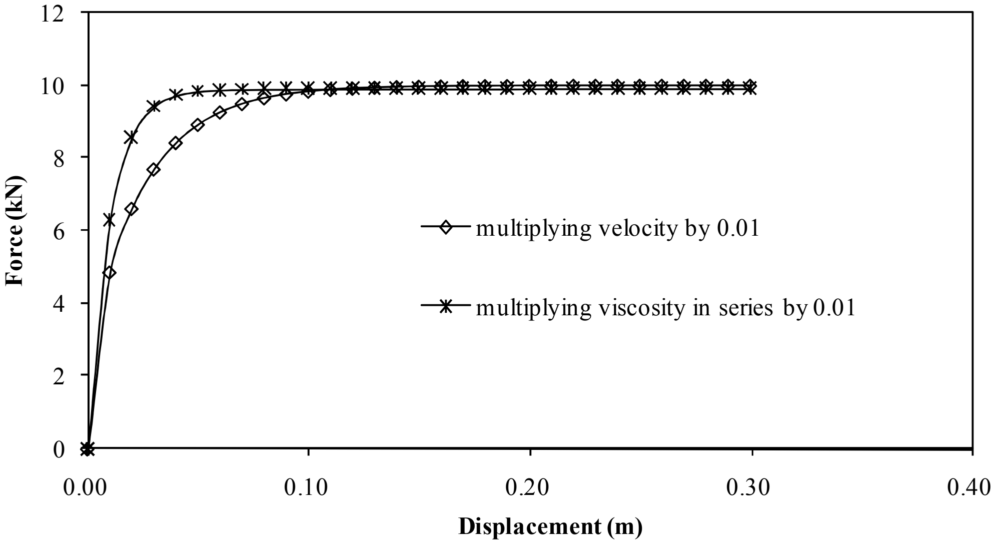

Figure 7.8: Preliminary attempt at scaling C_∞ and $\dot{u}$.

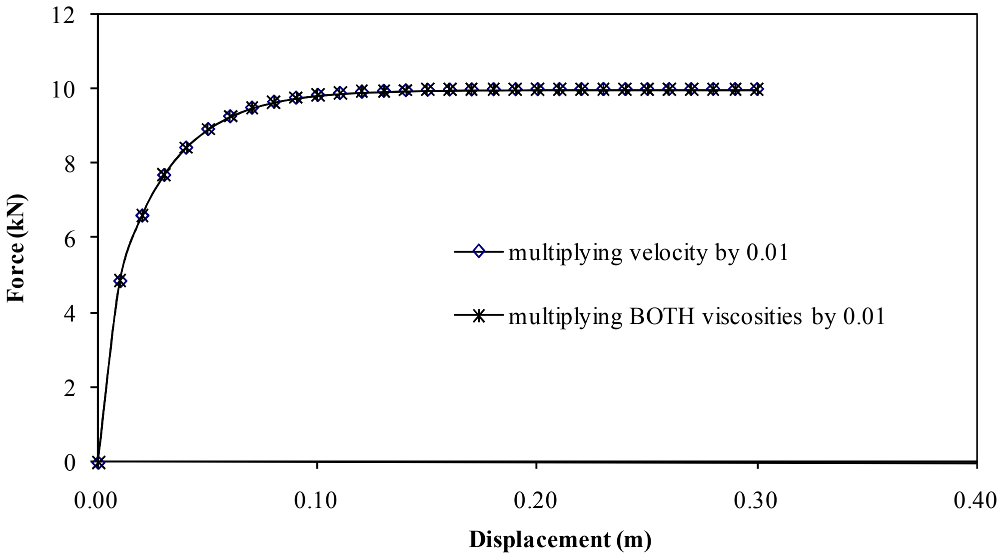

Figure 7.9: Analytical solution of scaling BOTH C_∞ and C_1 by the same factor as $\dot{u}$.

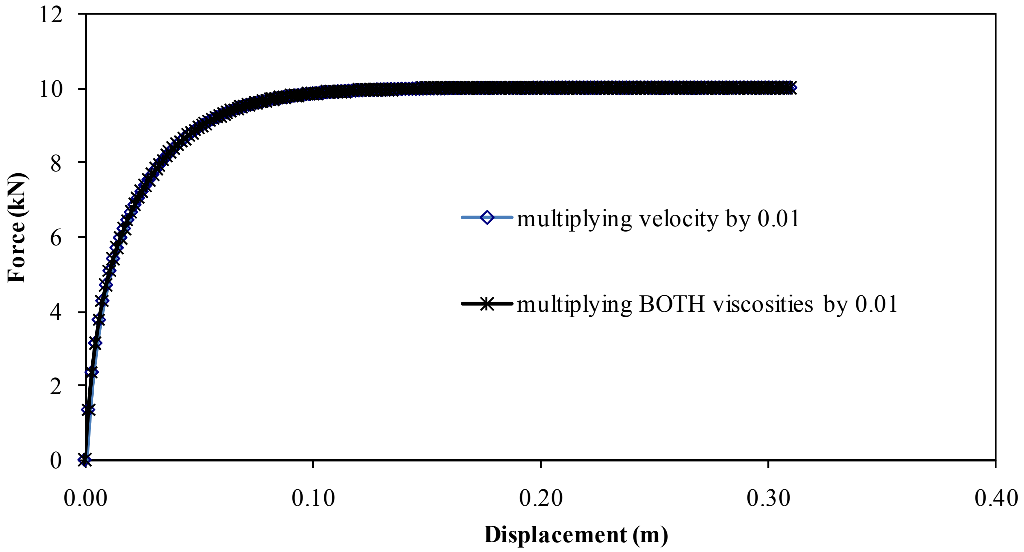

(a)

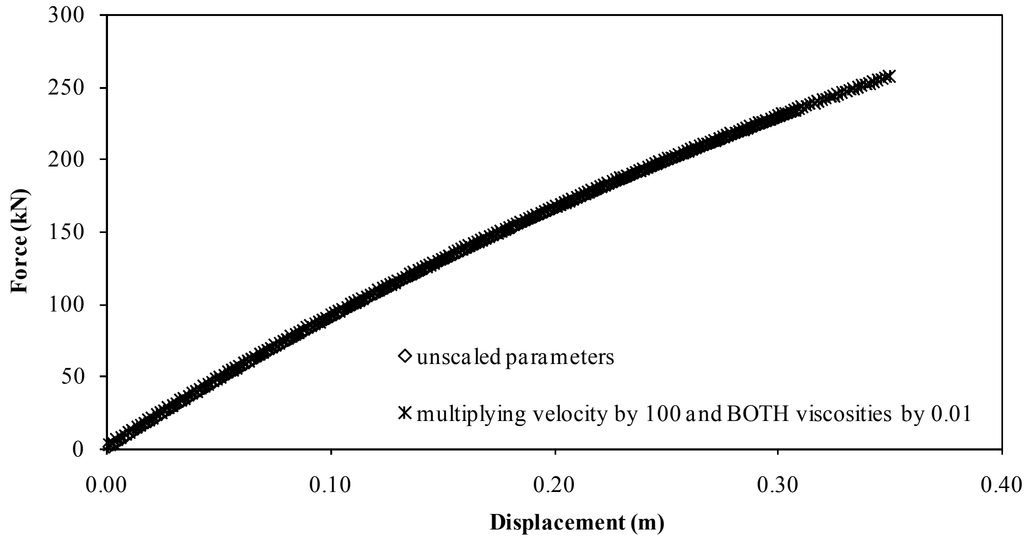

(b)

Figure 7.10: DEM simulations for a 2-particle test.

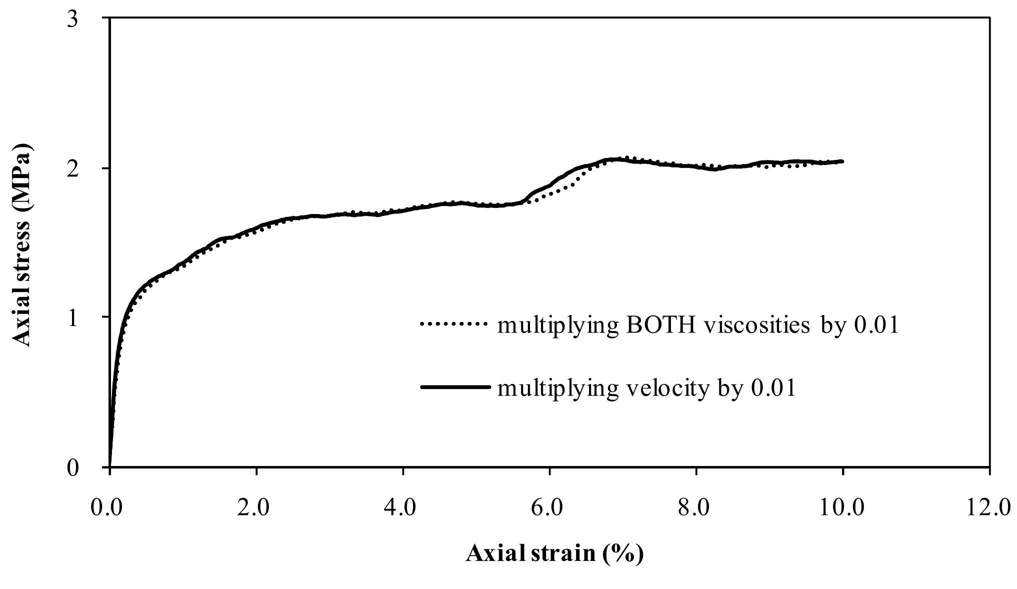

Figure 7.11: Simulations on 1000 bonded particles without bond breakage.

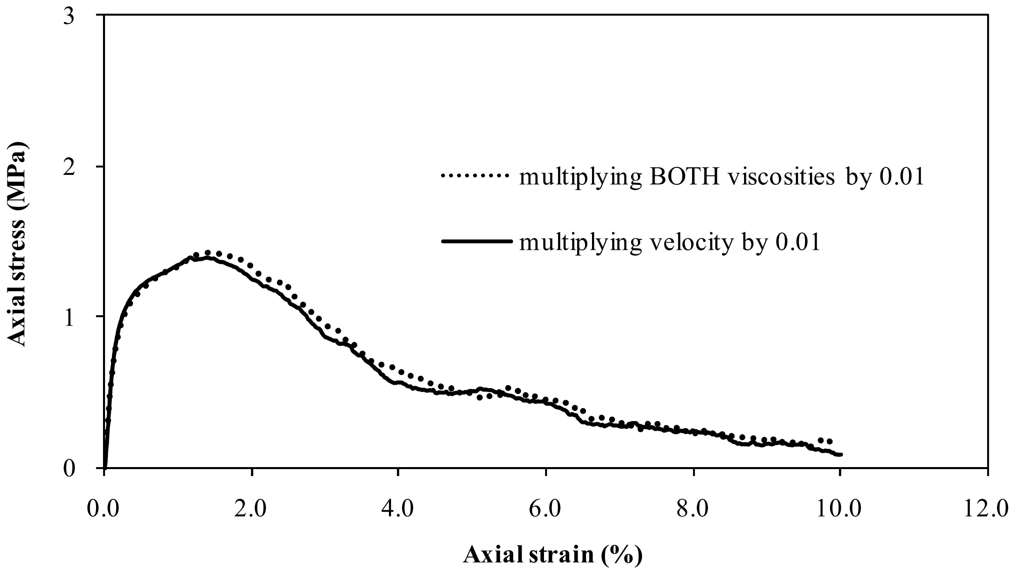

Figure 7.12: Simulations on 1000 bonded particles with bond breakage.

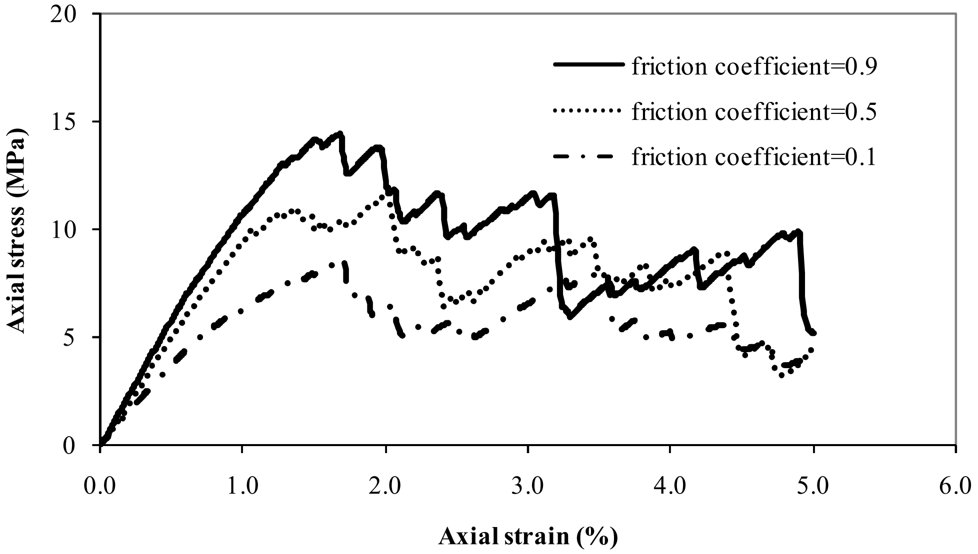

Figure 7.13: Effect of friction coefficient on predicted stress-strain response for simulations with 20% frictional contacts.

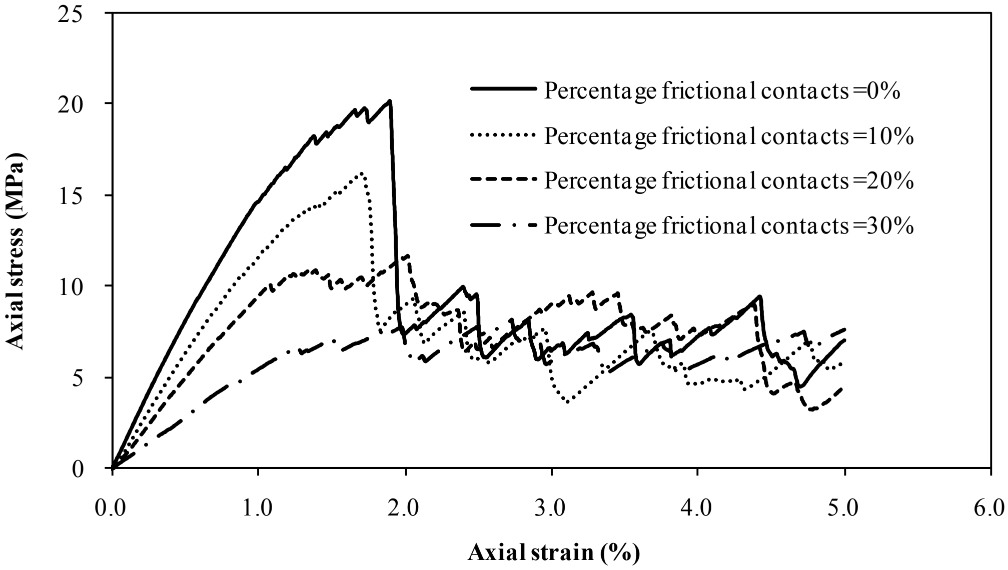

Figure 7.14: Effect of percentage of frictional contacts on predicted stress-strain response for simulations with friction coefficient of 0.5.

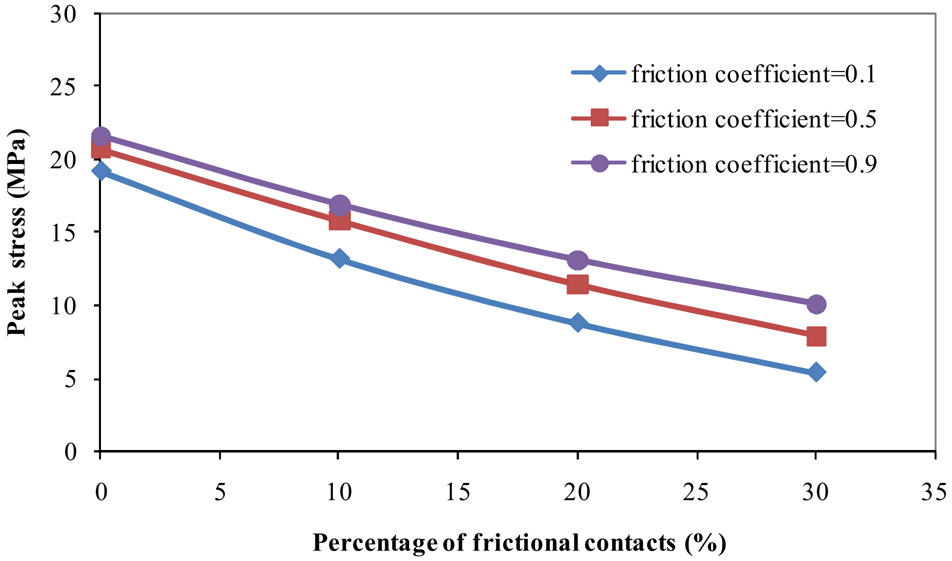

Figure 7.15: Effect of percentage of frictional contacts and friction coefficient on predicted peak stress.

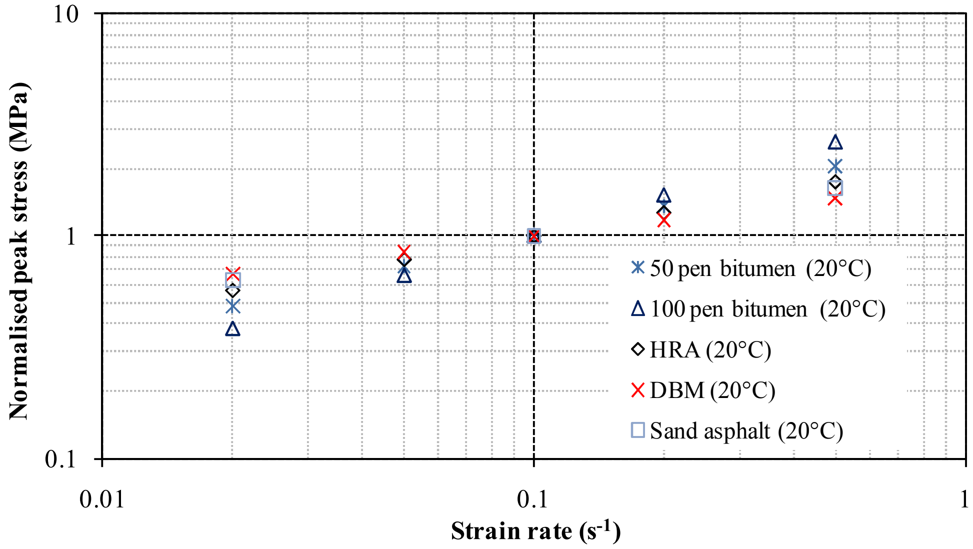

Figure 7.16: Normalised peak stress as a function of strain rate for various bituminous materials at 20°C (Cheung, 1995; Harvey, 2000; Grenfell *et al.,* 2008).

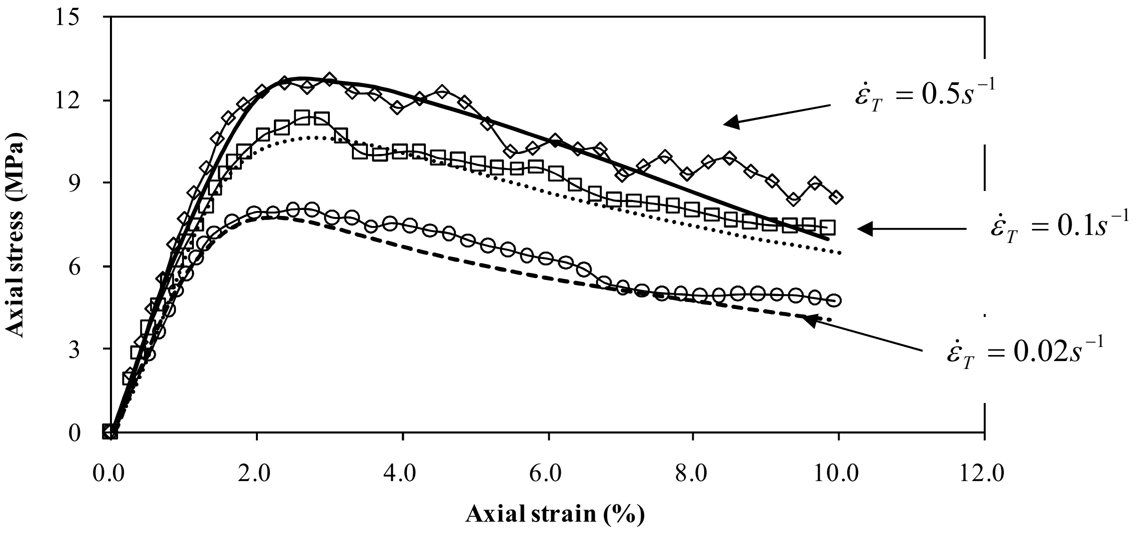

Figure 7.17: Predicted and measured axial stress-strain response for uniaxial compression tests at 10°C.

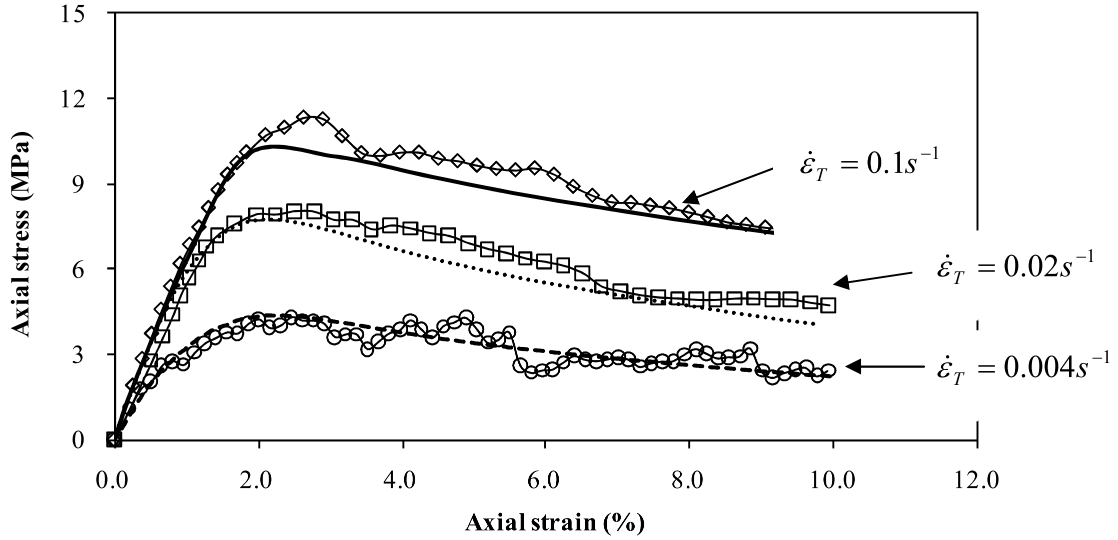

Figure 7.18: Predicted and measured axial stress-strain response for uniaxial compression tests at 20°C.

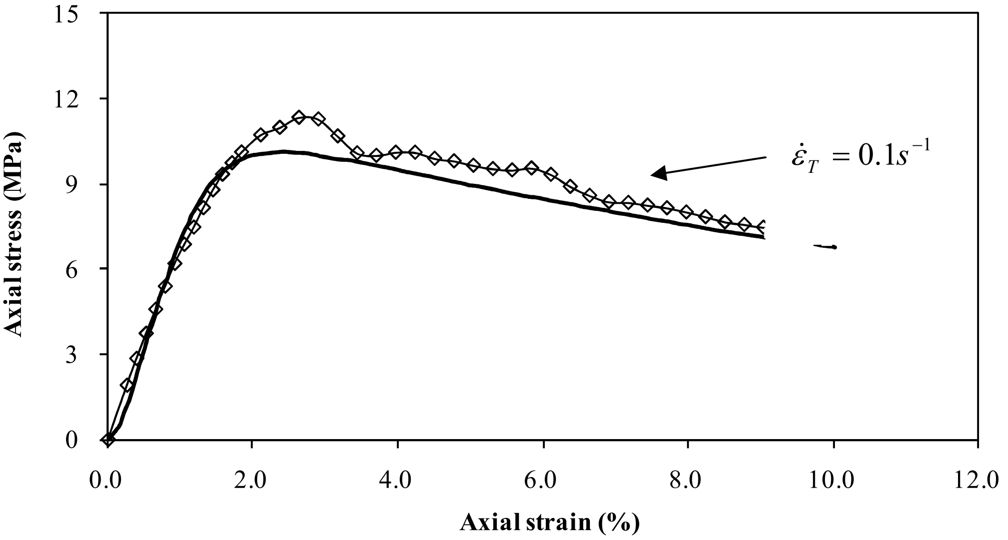

Figure 7.19: Predicted and measured axial stress-strain response for uniaxial compression tests at 0°C.

8 CONCLUSIONS AND RECOMMENDATIONS

8.1 Conclusions

A three dimensional meso-scale approach in the DEM has been developed to model the uniaxial compression tests in the idealised asphalt mixture over a range of testing conditions. The behaviour of the idealised asphalt mixture has been investigated experimentally and modelled numerically using the computer program (PFC3D). This chapter summaries the main conclusions of this thesis and also provides recommendations for future research in this area.

8.1.1 Literature review (Chapter 2)

A review of the relevant literature concerned with understanding the constitutive monotonic behaviour of bitumen and bituminous mixtures was provided in this chapter.

The literature review presented in this chapter indicated that the constitutive behaviour of asphalt mixtures at the macro-scale is reasonably well understood. It is a time, loading rate and temperature dependent viscoelastic behaviour. Asphalt materials are usually assumed to be linear viscoelastic at small strain rates and/or low stress level. However, at large strain rates and/or high stress level the behaviour of asphalt mixtures are generally non-linear viscoelastic and cannot be directly modelled by a linear viscoelastic approximation.

A number of constitutive models based on continuum mechanics are available to describe the behaviour of asphalt mixtures. These models have been successfully applied in predicting the behaviour of asphalts, although large calibration factors are required. Nevertheless none of the aforementioned models has been shown to be adequately capable of comprehensively describing the behaviour of asphalts. It is likely that a greater insight into the performance of asphalt mixtures can be gained by a better understanding of micromechanics of asphalt at the aggregate level.

8.1.2 Discrete element modelling (Chapter 3)

The review of micromechanical models for asphaltic materials has shown that these types of models are poorly developed at present. Therefore, there is a need to perform research by using micromechanical modelling to better understand the mechanical behaviour of the asphalt.

Recent developments in computation technology have allowed the simulation of the behaviour of asphalt as a heterogeneous material using DEM. PFC3D has been shown a powerful program in wide applications of modelling soil and asphalt, therefore it was chosen as the DEM programming code for this project. Some of the features in PFC3D such as calculation procedure, mechanical timestep and servo-control mechanism were reviewed.

The constitutive contact models in PFC3D including the contact model, bonding and slip model and Burger's contact model were reviewed. The Burger's contact model was chosen to represent the time dependent contact stiffness of asphalt material in the DEM simulations.

8.1.3 Experimental work (Chapter 4)

The experimental characterisation of the constitutive behaviour of the idealised asphalt mixture was described in this chapter. The idealised asphalt mixture was chosen as testing material due to its simple internal geometry. The procedure of specimen preparation in the laboratory was described and the details of employed friction reduction system between loading platen and specimen surface were given.

A series of monotonic constant strain-rate compression tests were performed to failure on the idealised asphalt mixture over a range of strain rates and temperatures. The constitutive behaviour of the idealised asphalt mixture was investigated as a first step to develop a micromechanical model.

It was found that the compressive strength of the idealised asphalt mixture showed nonlinear relationships with strain rate and/or temperature. A power-law equation has shown well predictions of the experimental data obtained at various strain rates. The strain rates applied at various temperatures were shifted to the strain rate at a reference temperature using an Arrhenius equation. Therefore, the compressive strength of the idealised asphalt mixture was found as a power-law function of both strain rate and temperature.

8.1.4 Numerical sample preparation procedure (Chapter 5)

A procedure for preparing a numerical sample that replicates a laboratory test specimen was described in this chapter. A dense randomly packed sample was generated with a volume fraction of solids equal to 64%. A procedure of preparing the sample to an equilibrium state with a low isotropic stress was described. Normal and shear contact bond has been installed at each contacting point to simulate the asphalt as a bonded material.

Some of the features of using measurement sphere in PFC3D was reviewed and applied in calculating the porosity and coordination number of the generated numerical sample before and during the simulations. The axial stress was calculated using the contact force between loading platen and contacting particles divided by the contacting area. The axial strain was measured using the relative displacement of the loading platen during the simulations.

8.1.5 Elastic modelling (Chapter 6)

An elastic contact model has been utilised in DEM to simulate the monotonic compressive behaviour of an idealised asphalt mixture in the elastic region of behaviour. Post peak (softening) behaviour was simulated by allowing bond breakage between adjacent particles. Results showed that the maximum rate of bond breakage occurred at the peak stress (compressive strength).

It was found that approximately 6000 particles are required for reasonably accurate estimates of bulk material properties such as compressive strength. It was found that a loading speed of 0.01*m/s* was an optimum speed below which the predicted stress-strain response is not depending on the loading speed providing the dynamic effect has been eliminated during simulations. It was found that the random effect of particle position on predicted compressive strength is not significant compared to variability in bond strength and the friction coefficient. The overall shape of the predicted stress-strain curve from the simulations with elastic contact model showed a qualitatively good agreement with the experimental results up to a strain level of approximately 2%.

8.1.6 Viscoelastic modelling (Chapter 7)

The details of viscoelastic modelling of the uniaxial compression tests on the idealised asphalt mixture in the ductile region were described in this chapter. A viscoelastic Burger's model was introduced to give time-dependent shear and normal tensile contact stiffness, whilst the normal compressive contact stiffness was assumed to be elastic.

A computation time optimisation method was developed so that the stress-strain response at slower strain rate can be predicted at a faster strain rate in DEM simulations. This computation time optimisation method has demonstrated an acceptable applicability in modelling bonded particles with bond breaking.

The bond breakage was introduced to model the post-peak softening behaviour of the idealised asphalt mixture in the ductile region. The strain-rate dependent bond strength was developed and used in modelling the stress-strain response of asphalt under various strain rates and temperatures. The viscoelastic modelling in DEM showed a good agreement with the experimental results in both the pre-peak and post-peak regions of behaviour.

8.1.7 Model calibration

Although it is relatively easy to assign chosen properties to a numerical model, it is often difficult to choose such properties so that the behaviour of the resulting numerical sample resembles that of an intended physical material (i.e. the idealised sand asphalt mixture). For the codes used in this DEM, PFC3D synthesize the macro-scale behaviour of materials from the interactions of micro-scale components, the input properties of the microscopic constituents (i.e. bitumen and aggregate) are not easy to measure in the laboratory. In this project, it was decided to determine relevant behaviour (and the response that best characterise such behaviours) of the idealised asphalt mixture, and then choose the appropriate micorproperties by means of a calibration process in which the responses of the generated numerical sample were compared directly with the relevant measured response from the experimental work (as described in Chapter 4). In general, most of the modelling work in this project was based on the calibration of the model with only a small aspect dealing with possible validation of test data at different temperatures.

Since it is difficult to directly relate the model parameters in PFC3D to a set of relevant material properties because the PFC3D model is also affected by the particle size and packing arrangement, the idealised sand asphalt mixture has been chosen as testing materials due to its simplified internal geometry and well known particle packing characteristics. The axial stress-strain response of this type of mixture under a certain testing conditions have been measured and used in a calibration process in developing the DEM in this project. The fundamental properties of the sand asphalt such as axial stress and axial strain are the main physical material responses that the process of calibration is based on.

In the elastic DEM model that has been developed in this project, there are five micro parameters required to characterise the brittle stress-strain response of the sand asphalt mixture, namely normal and shear contact stiffness, normal and shear bond strength and frictional coefficient. The ratio of normal contact stiffness to shear contact stiffness has been chosen as 10 to give a better prediction of Poisson's ratio. The effect of frictional coefficient between adjacent particles when the shear bond is broken has been investigated (described in Section 6.6). The values of the rest parameters were chosen based on the calibration procedure to match the experimental response when the behaviour was kept in the elastic end of its viscoelastic spectrum of behaviour.

In developing the viscoelastic model in using PFC3D, the calibration procedure is getting complicated due to the limitation of the Burger's model that has been employed to characterise the time-dependent viscoelastic nature of bitumen. The Burger's model is in fact a linear viscoelastic contact model that can well catch up the time-dependent response of the bitumen when its behaviour is dominated in the elastic region. However, it has been found that the bitumen and bituminous mixtures exhibit non-linear viscoelastic properties when the loading stress and/or strain rate is high. In order to simulate the stress-strain response of the sand asphalt mixture at a higher strain rate, the time-dependent bond strength has been investigated and developed (Section 7.5). This also involves a routine of calibration process that, although seems somewhat like "trials and errors", there are still some physical evidence that can increase the chance of "hit-and miss" throughout the calibration procedure. The ratio of normal contact stiffness to shear contact stiffness has been adjusted to be 3 according to the previous literature review (subsection 2.3.1). The inter-particle friction effects have been investigated to give a better prediction of the post-peak softening response. A large effort has been made to justify the validity of the gradient between compressive strength and strain rates in a double logarithmic scale that has been obtained from the experimental work and applied to scale both normal and shear bond strengths to simulate the peak stress in the viscoelastic modelling. There are also some validations to the viscoelastic model that has been developed to simulate the stress-strain response at different temperatures (described in subsection 7.5.2). Recommendations for future work of further validating the model has been addressed in the subsection 8.2.2.

8.2 Recommendations for Future Work

8.2.1 Limitations of discrete element modelling

Numerical modelling highly relies on the mathematic models that are usually based on certain assumptions to simplify the problems within an acceptable approximation.

Therefore, a good understanding of the physical mechanism plays a key role in choosing and developing a numerical model to represent the behaviour of the asphaltic materials.

Discrete element modelling has proved to be a promising approach to relate the observed macroscopic behaviour of the material to the micromechanical response at the meso-scale level (i.e. aggregate-aggregate contact). However, similar to other numerical models that for mathematic simplicity, some assumptions were made in developing the DEM and those assumptions resulted in lack of precision in describing the real behaviour of the problem. For example, in the DEM simulation a particle is modelled as a non deformable sphere. This assumption is reasonable for asphalt mixtures when applied stress level is low whilst it is not true at high stress level where aggregates can deform or even abrasion may occur. Therefore, it is important to realise that discrete element model or other numerical models is only acting as a supporting role in understanding the real physics of the problems.

8.2.2 Thin film of bitumen stiffening effect

It has been reviewed in Section 2.6 that the asphalt mixture can be characterised as contacting aggregates separating by the thin film of bitumen which plays an increasingly important role in understanding the deformation behaviour of the composite asphalt mixture. It has been found that the thin film of bitumen has a significant stiffening effect to give a rise to the contact stiffness between adjacent aggregates in the asphalt mixtures. Although this effect has not been applied in developing the DEM in this project for simplicity, it is recommended that this stiffening can be included in the further modelling to give a more realistic representation of particle contacting behaviour.

8.2.3 Model validation

A detailed validation studies are recommended to be undertaken to verify the appropriateness of the modelling work that has been developed in this project. This can be achieved by applying the viscoelastic model to simulate the uniaxial compression tests on the sand asphalt mixture over a broader range of testing conditions such as lower temperatures and/or higher strain rates. The predicted stress-strain response can be compared to relevant experimental data and the range of appropriateness of the model can be also determined during the validation procedure.

8.2.4 Modelling fatigue behaviour of asphalt mixtures

As a first step to model fatigue cracking of asphalt mixture, the monotonic compressive behaviour of asphalt mixture have been modelled in the DEM. The bond breakage criterion has shown to well simulate the post-peak softening behaviour of the idealised asphalt mixture under various strain rates and temperatures.

Future research can focus on further developing the model to simulate the fatigue behaviour of asphalt mixtures under cyclic loadings. This can be achieved by firstly undertaking careful experiments on the idealised asphalt mixture to investigate the fatigue behaviour under cyclic loadings. The response of tests under each condition should be measured carefully and the results can be used as a validation to the DEM. The discrete element model can be further developed to model the fatigue behaviour under repeated loadings by incorporating loading-unloading feature into the previous monotonic simulations.

8.2.5 Particle shape

The DEM simulations performed in this study assumed that the sample consists of single sized particles. However, this approximation is only valid at an ‘idealised’ stage to reduce the complexity in the simulations and it cannot represent the in situ size distribution of the aggregates in a realistic asphalt mixture. The complexity of this problem is increased by including the particle shape and the aggregate interlock effects into the simulations.

A non-sphere particle is represented by the clump feature in PFC3D. The clump can be used to model more realistic particle shapes as in the asphalt mixtures. Future work can focus on utilising a series of clumps to model more realistic aggregate structure and inter-particle contact behaviour of asphalt.

8.2.6 X-ray computed tomography

Recent development of X-ray tomography allows scanning into the internal structure of asphalt mixtures in three dimensions. The changes of internal structure of the asphalt mixtures at different stages when subjected to loading can be observed using X-ray technique. These changes (e.g. air voids) can be related to the internal damage (e.g. microcracks) within the asphalt mixtures under different loading stage. And the accumulation of microcracks within the sample can be regarded as physical evidence and related to the bond breakage in the DEM simulations.

APPENDIX A

A.1 Displacement Criterion

A displacement bond breakage criterion was investigated as an alternative method for simulating internal damage (microcracks) of asphalt mixtures for two main reasons. Firstly and foremost, it was noted earlier in the literature review that the failure strain (failure was defined as where the load begins to decrease in this chapter) is shown to be approximately strain rate independent for a range of compression tests in both the bitumen and bituminous materials (Harvey, 2000; Dunhill, 2002). Therefore, using a constant displacement as bond breaking criterion will simplify the simulations so that the Burger's contact model can be used straightforwardly to predict the strain rate dependent compressive strength of sand asphalt mixture. Secondly, parallel vertical cracks have been reported by other researchers in various experimental investigations that as Dunhill (2002) indicated, the damage mode in uniaxial compression tests is more likely to be controlled by the maximum tensile strain rather than stress in the specimen.

A.2 Experimental Justification

Harvey (2000) conducted a comprehensive investigations into Model I fracture behaviour of 100 pen bitumen under tensile loading. It was shown that for the thin films of bitumen (i.e. aspect ratio is greater than 8) the failure strain is film thickness (or aspect ratio) and strain rate independent and is approximately 10% in the ductile region.

As a first step of using displacement as bond breaking criterion, it is necessary to include this physical evidence into the numerical modelling. It was noted earlier that this idealised asphalt mixture has simplified internal geometry and its property is dominated by the bitumen whilst the complex aggregate interlock effect can be minimised. The idealised asphalt mixture was designed to have the following volumetric proportions; 70% sand (V_s), 20% bitumen (V_b) and 10% air voids (V_v). The sand was relatively single-sized, with a particle size distribution varying between 1.18*mm* to 2.36*mm* in diameter. First of all, the average sand radius (r) can be calculated as 0.885*mm*.

In the sand asphalt mixture the sand can be idealised as spheres and the total volume of sand (Vs) is therefore equals to the sum of the volume of each sphere with the average radius r by using the following equation (assuming the total volume of the sand asphalt mixture is 1m^3):

$$\frac{4}{3}\pi r^3 \times n = 0.7 \tag{A.1}$$

Therefore, the number of particles, n can be calculated as approximately 241.2×10^6. As an approximation, the bitumen can be assumed to coat the spheres with the uniform thickness t. And the thickness can therefore be calculated from the following equation:

$$n \times \frac{4}{3}\pi (r+t)^3 + V_v = 1 \tag{A.2}$$

Hence, the film thickness for the bitumen in the sand asphalt mixture is approximately 0.077 *mm*. Consequently the aspect ratio for sand asphalt, defined as sphere radius divided by the film thickness, can be calculated as follows:

$$A = \frac{r}{t} \approx 11 \tag{A.3}$$

It was indicated earlier by Harvey that for the thin films of bitumen ($A \geq 8$) the failure strain is approximately 0.1 and substitute this value into the following equation:

$$\varepsilon = \frac{\Delta t}{2t} = 0.1 \tag{A.4}$$

Therefore, the relative displacement between contacting spheres (Δt) when failure occurs is approximately 0.015 *mm* and this will be chosen as the tensile bond breaking criterion in the following modelling.

A.3 Preliminary Modelling with Displacement Criterion

It was noted earlier that the main reason to develop this displacement criterion is because the failure strain is shown to be strain rate independent in the experimental tests and thus the strain rate dependent compressive strength is supposed to be predicted by using Burger's contact model straightforward. A series of viscoelastic simulations was performed in this subsection to investigate the applicability of this displacement criterion as an alternative method in simulating the strain rate dependent peak stress of sand asphalt mixture.

The previous subsection showed that the displacement criterion for sand asphalt mixture has been calculated based on the physical evidence observed from tensile tests on the pure bitumen. The previous contact model in *PFC3D* was modified using C++ language based on this assumption to simulate the contact bonds breaking under the displacement criterion. It was designed in the program that when the relative distance between the centres of two contacting spheres is greater than 0.015*mm* then the contact bonds are broken.

A DEM simulation of two contacting spheres has been studied using the displacement criterion of 0.015*mm*. Four sets of simulations have been performed by pulling apart two particles (with one particle fixed) under different strain rates. Burger's contact model has also been used to govern the tensile force development and the details of contact parameters are given in Table A.1. The first set of simulation was performed at a constant velocity of 0.01*m/s* whilst for the second, third and fourth simulation, a constant velocity of 0.001*m/s*, 0.0001*m/s* and 0.00001*m/s* was applied, respectively. Figure A.1 shows a plot of contact force with respect to displacement for the four different velocities. It can be seen in this figure that for all velocities, the contact force increases as the velocity increases until the relative displacement between two contacting particles has reached 0.015*mm* then all contact forces are decreasing to zero simultaneously due to the contact bond has broken. It can also be seen from this figure that the velocity dependent peak force (stress) can be predicted by using the displacement criterion to break the contact bond.

A.4 Applications in Modelling Bonded Particles

In this subsection, a viscoelastic simulation was performed on a prepared numerical sample comprising 1000 bonded particles to examine the suitability of this displacement criterion in modelling the bonded sample. A viscoelastic Burger's model has been assumed for shear and tensile normal contact stiffnesses and an elastic contact has been assumed for the compressive normal contact stiffness, to represent non-viscous aggregate-aggregate contact. The contact parameters are shown in Table A.2. As an approximation, the displacement criterion of 0.015*mm* has been used to induce tensile bond breaking during the simulations whilst the shear bonds are not allowed to break during the whole simulations.

In the viscoelastic simulation, the numerical sample was loaded under a constant strain rate of 0.5s^{-1}. The simulation result has been shown in Figure A.2 where axial stress has been plotted against axial strain. It can be seen in this figure that the axial stress-strain response predicted under the displacement criterion has a similar shape to those predicted under the strength-based criterion. The bond breakage is also plotted in this figure with respect to the axial strain. It can be seen that the maximum rate of bond breakage coincides with the peak stress.

Figure A.3 shows the damage locations of broken bonds (microcracks) in the sample at 10% axial strain. It can be seen in this figure that uniformly distributed broken bonds can be observed throughout the sample under this displacement criterion. It should be noted that only tensile bonds (black circular) are designed to break under this criterion whilst no shear bonds are allowed to break during the simulation.

As a preliminary conclusion, the displacement criterion shows a promising feature as an alternative method in modelling the post-peak softening behaviour of the sand asphalt mixture.

The problem of using this displacement criterion in modelling the bonded particles at various strain rates was that the strain rate dependence has become more significant (as shown in Figure A.4-6). This displacement criterion also underpredicted the post-peak softening behaviour of the idealised asphalt mixture tested at the strain rate of $0.5s^{-1}$ (as shown in Figure A.7). It might be due to the fact that a single value of displacement criterion was used in the simulation.

A.5 Tables

Parameter	K_o *(MN/m)*	C_∞ *(MNs/m)*	K_1 *(MN/m)*	C_1 *(MNs/m)*	$\dot{u}$ *(m/s)*
Value	1.00	1.00	1.00	1.00	1.00

Table A.1: Burger's contact parameters for viscoelastic simulations for 2-particle contact.

Shear Contact		Tension Contact		Compression contact	
Property	Value	Property	Value	Property	Value
K_o^s (MN/m)	6.00	K_o^n (MN/m)	6.00	E_o^n (MN/m)	6.00
C_∞^s (MNs/m)	0.30	C_∞^n (MNs/m)	0.30		
K_1^s (MN/m)	6.00	K_1^n (MN/m)	6.00		
C_1^s (MNs/m)	0.30	C_1^n (MNs/m)	0.30		

Table A.2: Burger's contact parameters for viscoelastic simulations on bonded particles.

A.6 Figures

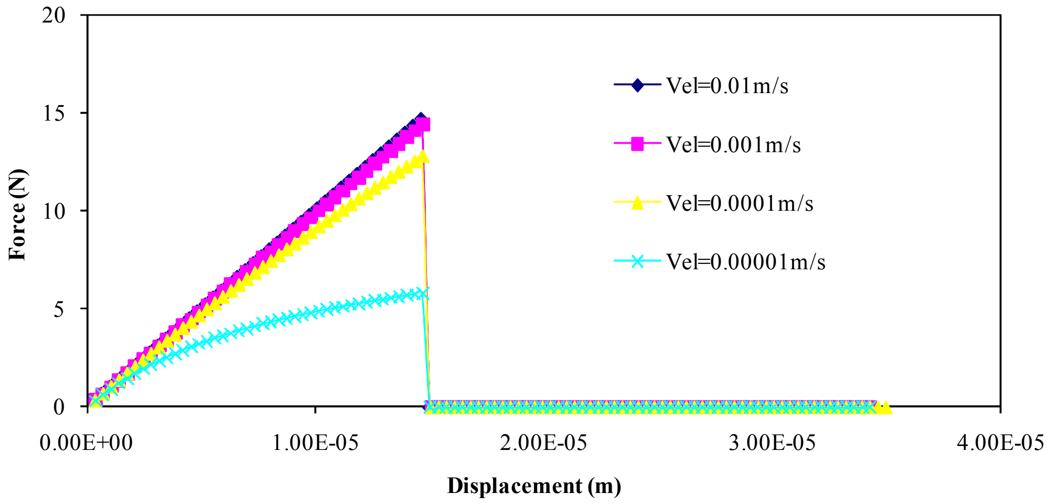

Figure A.1: Particle tests with displacement criterion.

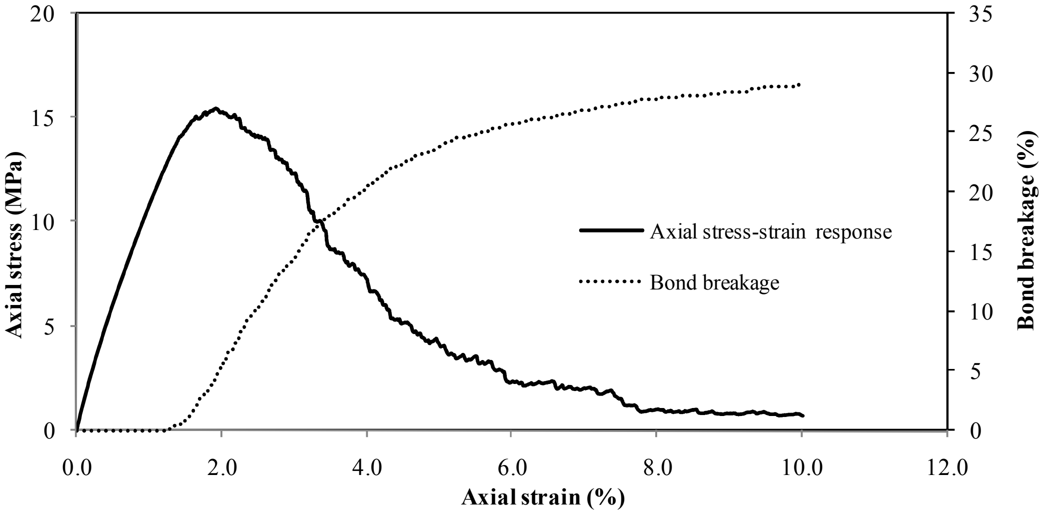

Figure A.2: A typical simulation result of stress-strain response and bond breakage using displacement bond breakage criterion.

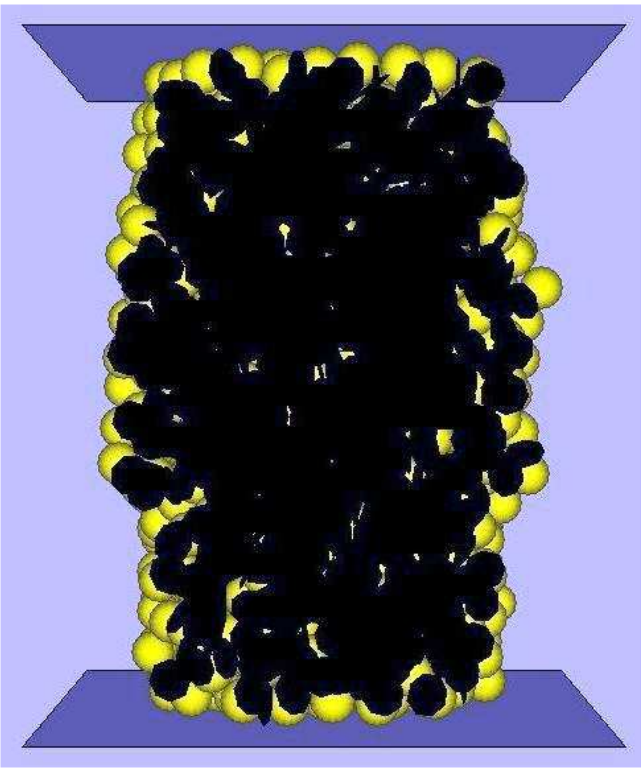

Figure A.3: An image showing tensile bond breaking locations in the sample.

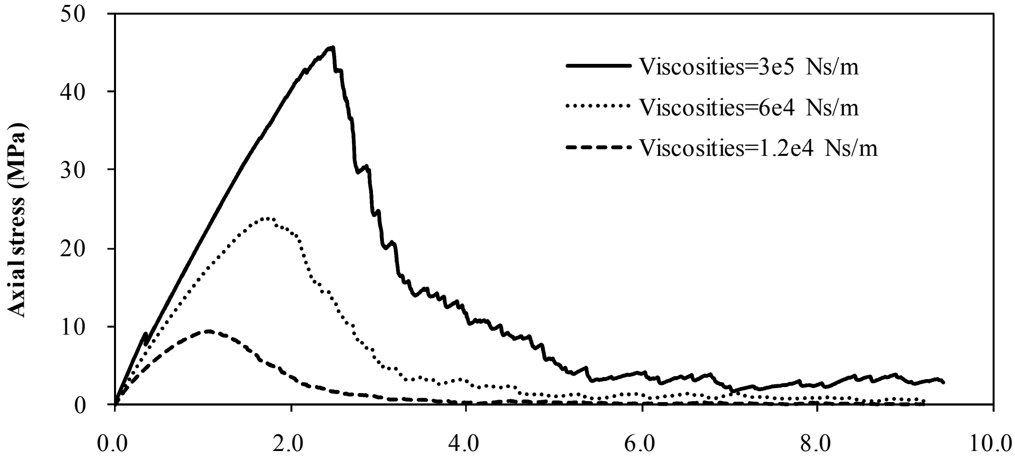

Figure A.4: Stress-strain response at different viscosities (Kc=Kt=Ks).

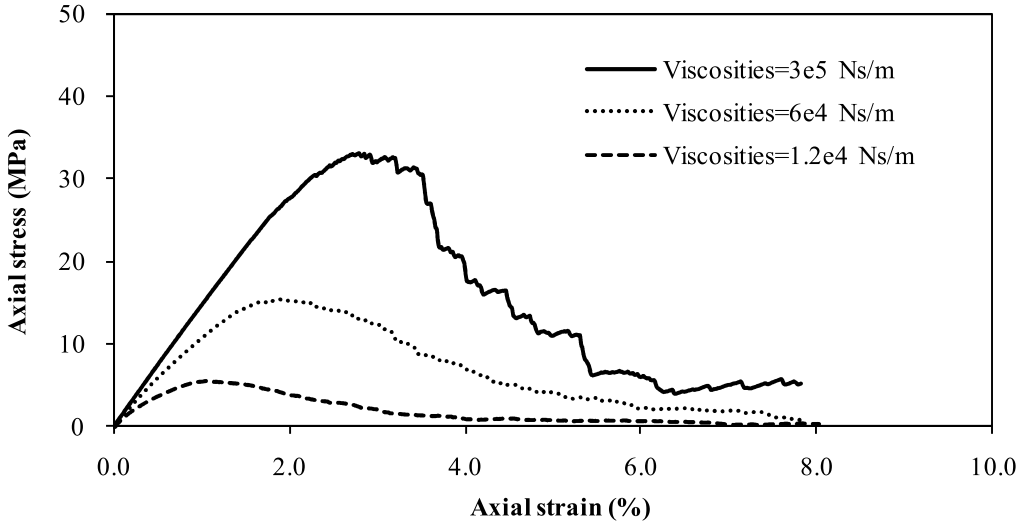

Figure A.5: Stress-strain response at different viscosities (Kc=Kt=3Ks).

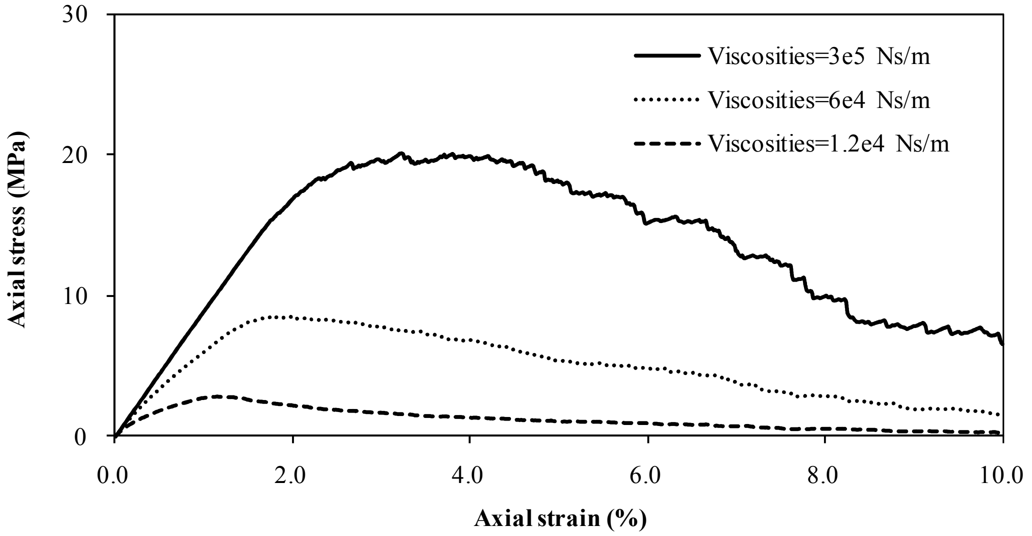

Figure A.6: Stress-strain response at different viscosities (Kc=Kt=10Ks).

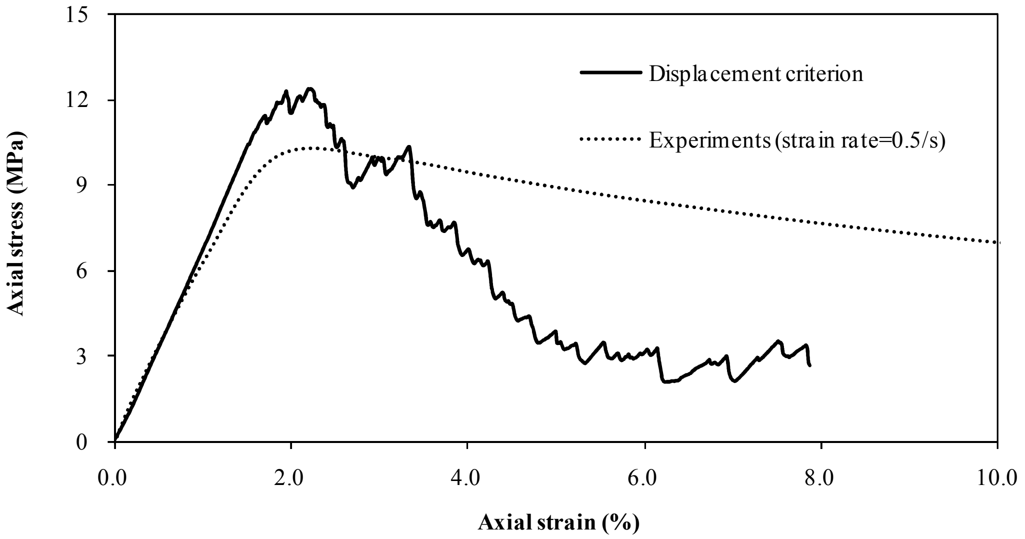

Figure A.7: Simulation result with displacement criterion compared with experimental result at strain rate of $0.5s^{-1}$.

REFERENCES

"Particle Flow Code in Three Dimensions, FISH", Minnesota, Itasca Consulting Group Inc., 2003.

"Particle Flow Code in Three Dimensions, Optional Features", Minnesota, Itasca Consulting Group Inc., 2003.

"Particle Flow Code in Three Dimensions, Theory and Background", Minnesota, Itasca Consulting Group Inc., 2003.

"Particle Flow Code in Three Dimensions, User's Guide", Minnesota, Itasca Consulting Group Inc., 2003.

Adams, R.D. and Coppendale, J., Journal of Adhesion, Vol. 10, 49, 1979.

Balci, O., *"Principles of Simulation Model Validation, Verification, and Testing",* Trans.Soc.Comput.Simul., 14(1), 3-12, 1997.

Bernal, J.D. and Mason, J., *"Co-ordination of Randomly Packed Spheres"*, Nature, Vol.188, pp.910-911, 1960.

Bezrukov, A., Stoyan, D. and Bargiel, M., *"Spatial Statistics for Simulated Packings of Spheres"*, Image Anal. Stereol., Vol.20, pp.203-206, 2001.

Blaauwendraad, J. and Scarpas, A., *"3D Finite element simulation of damage in asphalt concrete pavement"*, In: MCCI '2000 - International Symposium on Modern Concrete Composites & Infrastructures, Beijing, China, Volume I, pp. 11 – 16, 2000.

Brown, S.F., *"Stiffness and Fatigue Requirements for Structural Performance of Asphalt Mixes"*, Eurobitume Conference, London, 1978.

Brown, S.F., *"Practical Test Procedures for Mechanical Properties of Bituminous Materials",* Proc. Inst. of Civil Engineers Transport, Vol.111, pp.289-297, 1995.

Brown, S.F., *"Bituminous Pavements: Materials, Design and Evaluation"*, Residential Course Lecture Notes, School of Civil Engineering, University of Nottingham, 2002.

Buttlar, W.G. and You, Z., *"Discrete Element Modelling of Asphalt Concrete: A Microfabric Approach"*, Transportation Research Record, Vol.1757, pp.111-118, 2001.

Buttlar, W.G. and You, Z., *"Discrete Element Modelling to Predict the Modulus of Asphalt Concrete Mixtures"*, Journal of Materials in Civil Engineering, Vol.16, Issue 2, pp.140-146, 2004.

Carpenter, S.H. and Shen, S., *"Dissipated Energy Approach to Study Hot-Mix Asphalt Healing in Fatigue"*, TRR: Journal of Transportation Research Board, Vol. 1970, pp. 178-185, 2006.

Chang, G.K. and Meegoda, N.J., *"Simulation of the Behaviour of Asphalt Concrete Using Discrete Element Method"*, 2nd International Conference On Discrete Element Methods, M.I.T, 1993.

Cheung, C.Y., *"Mechanical Behaviour of Bitumen and Bituminous Mixes"*, PhD thesis, University of Cambridge, 1995.

Cheung, C.Y. and Cebon, D., *"Deformation Mechanisms of Pure Bitumen"*, Journal of Materials in Civil Engineering, Vol.9 (3), pp.117-129, 1997a.

Cheung, C.Y. and Cebon, D., *"Experiment Study of Pure Bitumen in Tension, Compression and Shear"*, Journal of Rheology, Vol.41(1), pp. 45-73, 1997b.

Cheung, C.Y. and Cebon, D., *"Thin Film Deformation Behaviour of Power-law Creeping Materials"*, ASCE Journal of Engineering Mechanics, Vol. 123(11), pp. 1138-1152, 1997c.

Cheung, C.Y., Cocks, A.C.F. and Cebon, D., *"Isolated Contact Model of an Idealised Asphalt Mix"*, International Journal of Mechanical Science, Vol. 41, pp.767-792, 1999.

Collop, A.C., Cebon, D. and Hardy, M.S., *"Viscoelastic Approach to Rutting in Flexible Pavements"*, Journal of Transportation Engineering Vol.121, pp.88-129, 1995.

Collop, A.C., McDowell, G.R. and Lee, Y., *"Modelling the Behaviour of an Idealised Asphalt Mixture Using The Distinct Element Method"*, Presented in TRB 83rd Annual Meeting, Washington D.C. 2003.

Collop, A.C., McDowell, G.R. and Lee, Y., *"Use of the Distinct Element Method to Model the Deformation Behaviour of an Idealised Asphalt Mixture"*, International Journal of Pavement Engineering, Vol.5(1), pp.1-7, 2004.

Collop, A.C., McDowell, G.R. and Lee, Y., *"Modelling Dilation in an Idealised Asphalt Mixture Using Discrete Element Modelling"*, Granular Matter, Vol.8(3-4), pp.175-184, 2006.

Collop, A.C., McDowell, G.R. and Lee, Y., *"On the Use of Discrete Element Modelling to Simulate the Viscoelastic Deformation Behaviour of an Idealised Asphalt Mixture"*, Geomechanics and Geoengineering, Vol.2(2), pp.77-86, 2007.

Cottrell, A.H., *"The Mechanical Properties of Matter"*, John Wiley, New York, 1964.

Cundall, P.A., *"A Computer Model for Simulating Progressive, Large-scale Movement in Blocky Rock System"*, Proc. Symp. Int. Soc. Rock Mech, Nancy, 1971.

Cundall, P.A., *"Computer Simulation of Dense Sphere Assemblies"*, Micromechanics of granular materials, Edited by: M. Satake and J.T. Jenkins, Amsterdam, Elsevier Science Publishers B.V., 1988a.

Cundall, P.A., *"Formulation of a Three-Dimensional Distinct Element Model - Part1. A Scheme to Detect and Represent Contacts in a System Composed of Many Polyhedral Blocks"*, Int. J. Rock Mech.,Min. Sci. & Geomech. Abstr., Vol.25(3), pp. 107-116, 1988b.

Cundall, P.A., Drescher, A. and Strack, O.D.L., *"Numerical Experiment on Granular Assemblies; Measurements and Observations"*, Deformation and Failure of Granular Materials, Edited by: P.A. Vermeer and H.J. Luger, Rotterdam, A.A. Balkema, 1982.

Cundall, P.A. and Hart, R., *"Numerical Modelling of Discontinua"*, J. Engr. Comp., Vol. 9, pp.101-113, 1992.

Cundall, P.A. and Strack, O.D.L., *"The Development of Constitutive Laws for Soil Using the Distinct Element Method"*, Third International Conference on Numerical Methods in Geomechanics, Aachen, pp.289-298, 1979a.

Cundall, P.A. and Strack, O.D.L., *"A Discrete Element Model for Granular Assemblies"*, Géotechnique, Vol.29(1), pp.47-65, 1979b.

De Josselin de Jong, G. and Verruijt, A., *"Etude photo-elastique d'un empilement de disques"*, Cahiers du Groupe Francais de Rheologie, Vol.2 (1), pp.73-86, 1969.

Deshpande, V.S., *"Steady-State Deformation Behaviour of Bituminous Mixes",* Ph.D. Thesis, Engineering Department, University of Cambridge, UK, 1997.

Deshpande, V.S. and Cebon, D., *"Steady-state Constitutive Relationships for Idealised Asphalt Mixes"*, Mechanics of Materials, Vol. 31, pp.271-287, 1999.

Deshpande, V.S. and Cebon, D., *"Uniaxial Experiments on Idealised Asphalt Mixes"*, Journal of Materials in Civil Engineering, Vol. 12, No.3, August, 2000.

Dukes, W.A. and Bryant, R.W., Journal of Adhesion, Vol. 1, 48, 1969.

Dunhill, S., *"Quasi-static Characterisation of Asphalt Mixtures"*, PhD thesis, University of Nottingham, UK, 2002.

Eisenmann, J. and Hilmer, A., *"Influence of Wheel Load and Inflation Pressure on the Rutting Effect at Theoretical Investigations"*, Proceedings of 6th International Conference on the Structural Design of Asphalt Pavements, Ann Arbor, Michigan, USA, 1987.

Eisenmann, J., Lempe, U. and Leykauf, G., *"Methods for the Structural Design of Asphalt Pavement"*, 4th Int. Conf. on the Structural Design of Asphalt Pavements, University of Michigan, 1977.

Erkens, S.M.J.G. and Poot, M.R., *"The Uniaxial Compression Test - Asphalt Concrete Response (ACRe)"*, Report 7-98-117-4, Delft University of Technology, 1998.

Gibb, J.M., *"Evaluation of Resistance to Permanent Deformation in the Design of Bituminous Paving Mixtures"*, PhD Thesis, University of Nottingham, UK, 1996.

Grenfell, J.R., Taherkhani, H., Collop, A.C., Airey, G.D. and Scarpas, A., *"Deformation Characterisation of Asphalt Concrete Behaviour"*, AAPT Vol.77, pp.479-516, 2008.

Gross, D. and Seelig, T., *"Fracture Mechanics: With an Introduction to Micromechanics"*, Germany, 2006.

Harvey, J.A.F., *"Bitumen Films In Tension"*, PhD dissertation, University of Cambridge, 2000.

Harvey, J.A.F. and Cebon, D., *"Failure Mechanism in Viscoelastic Films"*, Journal of Materials Science, Vol. 38, pp.1021-1032, 2003.

Harvey, J.A.F. and Cebon, D., *"Fracture Tests on Bitumen Films"*, Journal of Materials in Civil Engineering, Vol. 17, No.1, February, 2005.

Hazzard, J.F., Young, R.P. and Maxwell, S.C., *"Micromechanical Modelling in Cracking and Failure of Brittle Rocks"*, J. Geophysical Research, Vol 105, (B7), pp. 16683-16697, 2000.

Heukelom, W. and Klomp, A.J.G., *"Road Design and Dynamic Loading"*, Proceedings of Association of Asphalt Paving Technologists, Vol.33, pp. 92-125, 1964.

Hills, J.F., *"The Creep of Asphalt Mixes"*, J. of. Institute of Petroleum, Vol.59(570), pp. 247-262, 1973.

Hofstra, A. and Klomp, A.J.G., *"Permanent Deformation of Flexible Pavements under Simulated Road Traffic Conditions"*, Proc. 3rd Int. Conf. on the Structural Design of Asphalt Pavements, London, pp.613-621, 1972.

Huang, Y.H., *"Deformation and Volume Change Characteristics of a Sand Asphalt Mixture Under Constant Direct Triaxial Compressive Stresses"*, Highway Research Record, Vol.178, pp.60, 1967.

Ishibashi, I. and Chen, Y.C., *"Dynamic Shear Moduli and Their Relationship To Fabric of Granular Materials"*, Micromechanics of granular materials, Edited by: M. Satake and J.T. Jenkins, Amsterdam, Elsevier Science Publishers B.V., 1988.

Johnson, K.L., *"Contact Mechanics"*, Cambridge University Press, 1985.

Khanzada, S., *"Permanent Deformation in BItuminous Mixtures",* PhD Thesis, Department of Civil Engineering, University of Nottingham, UK, 2000.

Kleijnen, J.P.C., *"Verification and Validation of Simulation Models"*, Eur.J.Oper.Res., 82(1), 145-62, 1995.

Kim, H., Wagoner, M.P. and Buttlar, W.G., *"Fracture modelling considered rate-dependency of asphalt concrete using discrete element method"*, Proceedings of the International Conference on Advanced Characterisation of Pavement and Soil Engineering Materials, Athens, Greece, 20-22 June 2007.

Kim, H., Wagoner, M.P. and Buttlar, W.G., *"Simulation of fracture behaviour in asphalt concrete using a heterogeneous cohesive zone discrete element model"*, ASCE Journal of Materials in Civil Engineering, Vol. 20, Issue 8, pp.552-563, 2008.

Kinloch, A.J., Journal of Materials Science, Vol.17, 617, 1982.

Lee, Y.W., *"Discrete Element Modelling of Idealised Asphalt Mixture",* PhD Thesis, University of Nottingham, Nottingham, UK, 2006.

Lethersich, W., *"The Mechanical Behaviour of Bitumen"*, Journal of the Society of Chemical Industry Vol.61, pp. 101–108, 1942.

Lim, W.L. and McDowell, G.R., *"Discrete Element Modelling of Railway Ballast"*, Granular Matter 6(4), December, 2004.

Long, F.M., *"Permanent Deformation of Asphalt Concrete Pavements: A Non-linear Viscoelastic Approach to Mix Analyses and Design"*, PhD thesis, University of California, Berkeley, 2001.

Lu, M. and McDowell, G.R., *"Discrete element modelling of railway ballast under triaxial conditions"*, Geomechanics and Geoengineering: An International Journal, Vol.3, No.4, pp.257-270, 2008.

Lu, Yu., *"Temperature Dependent Visco-elasto-plastic Evaluation of Flexible Pavements"*, PhD Thesis, South Bank University, London, UK, 1998.

Masset, B.S., *"Mechanics of Fluids"*, 5th edition, 1983.

McDowell, G.R. and Harireche, O., *"Discrete Element Modelling of Soil Particle Fracture"*, Géotechnique, Vol.52(2), pp.131-135, 2002a.

McDowell, G.R. and Harireche, O., *"Discrete Element Modelling of Yielding and Normal Compression of Sand"*, Géotechnique, Vol.52(4), pp. 299-304, 2002b.

McDowell, G. R., Harireche, O., Konietzky, H., Brown, S. F. and Thom, N. H., *"Discrete Element Modelling of Geogrid-reinforced Aggregates",* Proceedings of the Institute of Civil Engineers, Geotechnical Engineering 159, pp.35-48, 2005.

McDowell, G.R., Collop, A.C. and Wu, J., *"A Dimensional Analysis of Scaling Viscosity and Velocity in DEM of Constant Strain Rate Tests on Asphalt"*, Submitted to Geomechanics and Geoengineering, 2008.

McLean, D.B. and Monismith, C.L., *"Estimation of Permanent Deformation in Asphalt Concrete Layers Due to Repeated Loading"*, Transportation Research Record, No 510, TRB, pp.14-30, 1997.

Monismith, C.L. and Secor, K.E., *"Viscoelastic Behaviour of Asphalt Concrete Pavements"*, Proceedings of 1st International Conference on the Structural Design of Asphalt Pavements, pp. 476-498, 1962.

Nadai, A., *"Theory of Flow and Fracture of solids"*, McGraw-Hill, 1963.

Newcomb, D.E., Struop-Gardiner, M., Olson, R. and Teig, J., *"Traffic Densification of Asphalt Concrete Pavement"*, Transportation Research Record, Nation Research Council, Washington, D.C., TRB, pp.1-9, 1997.

Oberkampf, W. L., *"Bibliography for Verification and Validation in Computational Simulations"*, Report: SAND98-2041, Sandia National Labs., Albuquerque, NM, United States, 1998.

Oberkampf, W. L., *"Feature: Computational Validation Series: Part 2. What Are Validation Experiments?"* Exp Tech, 25(3), 35-40, 2001.

Oberkampf, W. L., Trucano, T. G. and Hirsch, C., *"Verification, Validation, and Predictive Capability in Computational Engineering and Physics",* Applied Mechanics Review, 57(5), 345-84, 2004.

Oberkampf, W. L. and Barone, M. F., *"Measures of Agreement Between Computation and Experiment: Validation Metrics"*, Journal of Computational Physics, 217(1), 5-36, 2006.

Ossa, E.A., Deshpande, V.S. and Cebon, D., "*A Phenomenological Model for the Monotonic and Cyclic Behaviour of Pure Bitumen"*, ASCE Journal of Material in Civil Engineering, 2003.

Ossa, E.A., *"Deformation Behaviour of Bitumen and Bituminous Mixes"*, PhD Thesis, University of Cambridge, UK, 2004.

Ossa, E.A., Taherkhani, H. and Collop, A.C., *"Compressive Deformation Behaviour of Asphalt Mixtures"*, Journal of Association of Asphalt Paving Technologists, March, 2005.

Ossa, E.A., Deshpande, V.S. and Cebon, D., *"Phenomenological model for the monotonic and cyclic behaviour of pure bitumen"*, ASCE Journal of Materials in Civil Engineering, Vol.17, No.2, pp188-197, March/April 2005.

Pagen, C.A., *"Rheological Rsponse of Bituminous Concrete"*, Highway Research Record, No.67, 1964.

Pell, P.S. and Taylor, I.F., *"Asphaltic Road Materials in Fatigue"*, Proc. Assn. of Asphalt Paving Technologist, Vol.38, pp.371-422, 1969.

Powrie, W., Ni, Q., Harkness, R.M. and Zhang, X., *"Numerical Modelling of Plane Strain Tests on Sands Using a Particulate Approach"*, Géotechnique, Vol.55, (4), pp.297-306, 2005.

Read, J.M., *"Fatigue Cracking of Bituminous Paving Mixtures"*, PhD Thesis, University of Nottingham, Nottingham, UK, 1996.

Read, J. and Whiteoak, D., *"The Shell Bitumen Handbook"*, fifth edition, Shell UK Oil Products Limited, 2003.

Renken, P., *"Influence of Specimen Preparation onto the Mechanical Behaviour of Asphalt Aggregate Mixtures"*, Proceedings of 2nd Eurasphalt & Eurobitume Congress, pp. 729, 2000.

Robertson, D., *"Numerical Simulations of Crushable Aggregates"*, Ph.D. dissertation, University of Cambridge, 2000.

Rothenburg, L. and Bathurst, R.J., *"Micromechanical features of granular assemblies with planar elliptical particles"*, *Géotechnique*, 42(1), pp. 79-95, 1992.

Saad, M.H., Dai, Qingli., Parameswaran, Venkitanarayanan. and Shukla, Arun., "*Microstructural Simulation of Asphalt Materials: Modelling and Experimental Verification"*, 15th ASCE Engineering Mechanics Conference, New York, 2002.

Scarpas, A. and Blaauwendrad, J., *"Experimental Calibration of a Consititutive Model for Asphalt Concrete"*, Proceedings of the Euro-C Conference on the Computational Modelling of Concrete Structures, Bagastein, Ostenrijk, pp.193-202, 1998.

Scott, G.D., *"Packing of Spheres"*, Nature, Vol.188, pp. 908-909, 1960.

Starodubsky, S., Belchman, I. and Livneh, M., *"Stress-strain Relationship for Asphalt Concrete in Compression"*, RILEM, Materials and Structures, Vol.27, pp. 474-482, 1994.

Tashman, L., Masad, E., Peterson, B. and Saleh, H., *"Internal Structure Analysis of Asphalt Mixes to Improve the Simulation of Superpave Gyratory Compaction to Field Compaction"*, Asphalt Paving Technology 70, 2001.

Thom, N., *"Principles of Pavement Engineering"*, University of Nottingham, 2008.

Thrower, E.N., *"A Parametric Study of Fatigue Prediction Model for Bituminous Road Pavements"*, TRRL Laboratory Report No. 892. 1979.

Trucano, T. G., Swiler, L. P., Igusa, T., Oberkampf, W. L. and Pilch, M., *"Calibration, Validation, and Sensitivity Analysis: What's What",* Reliab.Eng.Syst.Saf., 91(10-11), 1331-57, 2006.

Ullidtz, P., *"Analytical Tools For Design of Flexible Pavements"*, Keynote Address, Proceedings of 9th International Conference on Asphalt Pavements, Vol. III, pp.22-37, Copenhagen, Denmark, 2003.

Van der Loo, P.J., *"The Creep Test: A Key Tool in Asphalt Mix Design and In The Prediction of Pavement Rutting"*, Proceedings of Association of Asphalt Paving Technologists, Vol.47, pp. 523-557, 1978.

Van der Poel, C., *"Representation of Rheological Properties of Bitumen Over a Wide Range of Temperatures and Loading Times"*, Proceedings of 2nd International Congress on Rheology, pp. 331-337, 1954.

Van der Poel, C., *"Time and Temperatures Effects on the Deformation of Asphaltic Bitumens and Bitumen-Mineral Mixtures"*, Journal of Society of Petroleum Engineers, pp. 47-53, 1955.

Vardoulakis, I., Labuz, J.F., Papamichos, E. and Tronvoll, J., *"Continuum Fracture Mechanics of Uniaxial Compression on Brittle Materials"*, International Journal of Solids and Structures, Vol.35, pp.4313-4335, 1998.

Velasco, F. R. D., *"Method For Test Data Selection",* J.Syst.Software*,* 7(2), 89-97, 1987.

Wu, J., Collop, A.C. and McDowell, G.R., *"Discrete Element Modelling of Low Temperature Monotonic Compression Tests in an Idealised Asphalt Mixture"*, the 6th

RILEM International Conference on Cracking in Pavements, Chicago, 16-18 June, 2008.

Wu, J., Collop, A.C. and McDowell, G.R., *"Discrete Element Modelling of Monotonic Compression Tests in an Idealised Asphalt Mixture"*, Submitted to the 3rd International Conference on Asphalt Materials, Shandong, China, 6-7 August, 2009.

Wu, J., Collop, A.C. and McDowell, G.R, *"Modelling Compressive Behaviour of an Idealised Asphalt Mixture using Discrete Element Modelling"*, Submitted to ASCE Journal of Materials in Civil Engineering, 2009.